IAEA TECDOC SERIES

IAEA-TECDOC-1890

IAEA-TECDOC-1890

Heavy Water Reactor Moderator Effectiveness as a Backup Heat Sink during Accidents

IAEA
International Atomic Energy Agency

HEAVY WATER REACTOR MODERATOR EFFECTIVENESS AS A BACKUP HEAT SINK DURING ACCIDENTS

The following States are Members of the International Atomic Energy Agency:

AFGHANISTAN
ALBANIA
ALGERIA
ANGOLA
ANTIGUA AND BARBUDA
ARGENTINA
ARMENIA
AUSTRALIA
AUSTRIA
AZERBAIJAN
BAHAMAS
BAHRAIN
BANGLADESH
BARBADOS
BELARUS
BELGIUM
BELIZE
BENIN
BOLIVIA, PLURINATIONAL STATE OF
BOSNIA AND HERZEGOVINA
BOTSWANA
BRAZIL
BRUNEI DARUSSALAM
BULGARIA
BURKINA FASO
BURUNDI
CAMBODIA
CAMEROON
CANADA
CENTRAL AFRICAN REPUBLIC
CHAD
CHILE
CHINA
COLOMBIA
CONGO
COSTA RICA
CÔTE D'IVOIRE
CROATIA
CUBA
CYPRUS
CZECH REPUBLIC
DEMOCRATIC REPUBLIC OF THE CONGO
DENMARK
DJIBOUTI
DOMINICA
DOMINICAN REPUBLIC
ECUADOR
EGYPT
EL SALVADOR
ERITREA
ESTONIA
ESWATINI
ETHIOPIA
FIJI
FINLAND
FRANCE
GABON
GEORGIA
GERMANY
GHANA
GREECE
GRENADA
GUATEMALA
GUYANA
HAITI
HOLY SEE
HONDURAS
HUNGARY
ICELAND
INDIA
INDONESIA
IRAN, ISLAMIC REPUBLIC OF
IRAQ
IRELAND
ISRAEL
ITALY
JAMAICA
JAPAN
JORDAN
KAZAKHSTAN
KENYA
KOREA, REPUBLIC OF
KUWAIT
KYRGYZSTAN
LAO PEOPLE'S DEMOCRATIC REPUBLIC
LATVIA
LEBANON
LESOTHO
LIBERIA
LIBYA
LIECHTENSTEIN
LITHUANIA
LUXEMBOURG
MADAGASCAR
MALAWI
MALAYSIA
MALI
MALTA
MARSHALL ISLANDS
MAURITANIA
MAURITIUS
MEXICO
MONACO
MONGOLIA
MONTENEGRO
MOROCCO
MOZAMBIQUE
MYANMAR
NAMIBIA
NEPAL
NETHERLANDS
NEW ZEALAND
NICARAGUA
NIGER
NIGERIA
NORTH MACEDONIA
NORWAY
OMAN
PAKISTAN
PALAU
PANAMA
PAPUA NEW GUINEA
PARAGUAY
PERU
PHILIPPINES
POLAND
PORTUGAL
QATAR
REPUBLIC OF MOLDOVA
ROMANIA
RUSSIAN FEDERATION
RWANDA
SAINT LUCIA
SAINT VINCENT AND THE GRENADINES
SAN MARINO
SAUDI ARABIA
SENEGAL
SERBIA
SEYCHELLES
SIERRA LEONE
SINGAPORE
SLOVAKIA
SLOVENIA
SOUTH AFRICA
SPAIN
SRI LANKA
SUDAN
SWEDEN
SWITZERLAND
SYRIAN ARAB REPUBLIC
TAJIKISTAN
THAILAND
TOGO
TRINIDAD AND TOBAGO
TUNISIA
TURKEY
TURKMENISTAN
UGANDA
UKRAINE
UNITED ARAB EMIRATES
UNITED KINGDOM OF GREAT BRITAIN AND NORTHERN IRELAND
UNITED REPUBLIC OF TANZANIA
UNITED STATES OF AMERICA
URUGUAY
UZBEKISTAN
VANUATU
VENEZUELA, BOLIVARIAN REPUBLIC OF
VIET NAM
YEMEN
ZAMBIA
ZIMBABWE

The Agency's Statute was approved on 23 October 1956 by the Conference on the Statute of the IAEA held at United Nations Headquarters, New York; it entered into force on 29 July 1957. The Headquarters of the Agency are situated in Vienna. Its principal objective is "to accelerate and enlarge the contribution of atomic energy to peace, health and prosperity throughout the world''.

IAEA-TECDOC-1890

HEAVY WATER REACTOR MODERATOR EFFECTIVENESS AS A BACKUP HEAT SINK DURING ACCIDENTS

INTERNATIONAL ATOMIC ENERGY AGENCY
VIENNA, 2019

For further information on this publication, please contact:

Nuclear Power Technology Development Section
International Atomic Energy Agency
Vienna International Centre
PO Box 100
1400 Vienna, Austria
Email: Official.Mail@iaea.org

Printed by the IAEA in Austria
December 2019

IAEA Library Cataloguing in Publication Data

Names: International Atomic Energy Agency.
Title: Heavy water reactor moderator effectiveness as a backup heat sink during accidents / International Atomic Energy Agency.
Description: Vienna : International Atomic Energy Agency, 2019. | Series: IAEA TECDOC series, ISSN 1011–4289 ; no. 1890 | Includes bibliographical references.
Identifiers: IAEAL 19-01282 | ISBN 978–92–0–162919–7 (paperback : alk. paper) | ISBN 978–92–0–163019–3 (pdf)
Subjects: LCSH: Heavy water reactors. | Reactor moderators. | Nuclear reactors — Safety measures. | Computer simulation.

FOREWORD

The IAEA organizes International Collaborative Standard Problems (ICSPs) to facilitate the development and validation of computer codes for design and safety analysis of nuclear power plants. The implementation of an ICSP usually includes an experimental investigation of interesting phenomena and simulation of the experiment using computer codes. Activities within the framework of the IAEA's Technical Working Group on Advanced Technologies for Heavy Water Reactors (TWG-HWR) are conducted within the IAEA's subprogramme on nuclear power reactor technology development. One of the activities recommended by the TWG-HWR was an ICSP exercise entitled Heavy Water Reactor Moderator Subcooling Requirements to Demonstrate Backup Heat Sink Capabilities of the Moderator during Accidents.

An important safety feature of heavy water reactors (HWRs) is the ability to use the moderator as a backup heat sink during emergencies. The purpose of this ICSP was to provide thermomechanical experimental data on the combined performance of the pressure tube (PT) and the surrounding calandria tube (CT) as the overheated PT comes into contact with the moderator cooled CT. Several experiments have shown that the post-contact behaviour of the channel, and the ability of the moderator to act as a backup heat sink during accidents that involve fuel overheating, are dependent on moderator subcooling and the internal pressure, the heat-up rate and the contact temperature of the PT. One such experiment, conducted at Canadian Nuclear Laboratories, was used as a benchmark in this ICSP, with eight participants from five countries operating HWRs contributing both blind and open calculations.

This publication summarizes the experiment, the complex interaction of transient phenomena that ultimately determine the fuel channel behaviour, the simulation methods and results, and the lessons learned from the ICSP.

The IAEA would like to express its appreciation to the Canadian Nuclear Laboratories for conducting the experiment and releasing the data to the international community, and to T. Nitheanandan (Canada) for leading the activity. The IAEA officer responsible for this publication was M. Krause of the Division of Nuclear Power.

CONTENTS

1. INTRODUCTION

The International Atomic Energy Agency (IAEA) fosters international cooperation on technology development for improved safety of water cooled reactors (WCRs) with the goals to increase fundamental understanding and improve the modelling tools. In particular, the intercomparison, benchmarking and validation of computer codes for Heavy Water Reactor (HWR) thermalhydraulics safety analyses is an ongoing activity to facilitate international cooperative research and promote information exchange on computer codes for HWR safety analyses. The objective is to enhance the safety analysis capabilities of the participants and the effective use of their resources in Member States operating or planning HWRs. Along with focused code comparison exercises using large scale experiments, these collaborations provide participants from R&D, plant operators, and regulatory bodies valuable data against which analysis methods and codes can be benchmarked in the future.

A new International Collaborative Standard Problem (ICSP) was discussed and endorsed in July 2011 by the Technical Working Group on Heavy Water Reactors (TWG-HWR) to conduct a code comparison or benchmark using a new contact boiling experiment performed at Canadian Nuclear Laboratories (CNL, at the time Atomic Energy of Canada Ltd., AECL). This report documents the results from eight participants from five Member States, all with currently operating HWRs.

1.1. BACKGROUND

This ICSP, recommended at TWG-HWR meeting held on 26–28 July 2011 and entitled *Heavy Water Reactor Moderator Subcooling Requirements to Demonstrate Backup Heat Sink Capabilities of the Moderator during Accidents* commenced with a small Consultancy Meeting on 14–17 February 2012, where the ICSP proposal was developed.

The first Technical Meeting was held in Ottawa, Canada on 19–21 November 2012 and included a visit of the CNL experimental facility where the ICSP experiment would be conducted. The Meeting was attended by 15 participants from 10 participating institutes from 5 Member States (Canada, India, Pakistan, Republic of Korea and Romania). Detailed information on the test facility and procedure, the phenomena involved, instrumentation, and relevant publications were made available by the ICSP host, CNL. Each participant presented their research experience on HWR fuel channel behaviour, and the computer codes and approach proposed for the ICSP. Common approaches, assumptions and inputs to facilitate the comparison of blind and open calculation results were discussed and all 10 participating institutes declared their intention to participate in the benchmark. The facility visit and discussion with operations staff proved very useful for the participants in resolving questions related to the facility configuration, operations, instrumentation and code requirements.

CNL performed the experiment for the ICSP in the High Temperature Fuel Channel Laboratory at Chalk River Laboratories on 17 June 2013 and issued a memo to all participants describing the data to be used as input to the blind simulations of the experiment. The data, in the form of an Excel spreadsheet, included measured initial conditions and boundary conditions as well as measured apparatus dimensions.

The second meeting was held in Vienna, Austria, 9–11 July 2014. The objectives of this meeting were to (1) fully understand the experimental data, (2) compare participants' blind calculations, using the actual test initial and boundary conditions, with the experimental measurements of pressure, temperatures, and deformation of pressure and calandria tubes and

(3) assess code capabilities and modelling issues or gaps. Eight institutes presented their blind calculation results, the host organization then presented the test results with actual experimental measurements and the synthesis of comparison between blind calculations. The presentation included several videos (proprietary and not cleared for publication) of the CT outside surface, clearly showing nucleate and film boiling regions and the development and subsequent rewetting of dry-patches. The test results were of high quality and self-consistent, achieving the objectives of displaying the important behaviours and providing good validation data. The following technical discussions and identification of modelling gaps and areas for improvement were very useful to all participants.

The third and final meeting was held in Vienna, Austria, 27–29 January 2015. The purposes of the meeting were to (1) compare participants' open calculations with the experimental measurements of pressure, temperatures, and deformation of pressure and calandria tubes, (2) assess code capabilities and sensitivities, modelling issues or gaps, (3) agree on lessons learned, and (4) plan the final steps of the ICSP, including assigning responsibilities for authoring sections of the final report (this publication). Noting the remaining differences in some assumptions in the participants' open calculations, it was agreed that a final open calculation should be done by all, using consistent input and assumptions in all simulations. For this purpose, a checklist was developed (see Appendix).

1.2. OBJECTIVE

The specific objectives of this ICSP were for the participants to:

- Improve understanding of important phenomena expected to occur in the experiment;
- Evaluate code capabilities to predict these important phenomena, their practicality and efficiency, by simulating the integrated experiment;
- Suggest necessary code or methodology improvements to reduce uncertainties.

This report provides a comparison of the results obtained from eight participating organizations from five countries, utilizing different methods and computer codes. General conclusions are reached, and recommendations made.

1.3. SCOPE

The purpose of this ICSP was to provide contact boiling experimental data to assess the subcooling requirements for a heated pressure tube, plastically deforming into contact with the calandria tube during a postulated large break loss of coolant accident condition. The data can be used to assess safety analysis computer codes simulating the following phenomena:

- Radiation heat transfer to the pressure tube;
- Pressure tube deformation or failure;
- Pressure tube to calandria tube heat transfer;
- Calandria tube to moderator heat transfer;
- Calandria tube deformation or failure.

1.4. STRUCTURE

The technical background, fuel channel behaviour during an overheating transient under pressure, and the safety significance are briefly discussed in Section 2. Section 3 provides a description of the test facility and instrumentation, as it was configured for the experiment, and a detailed description of the test subject to this exercise. Section 4 summarizes each participant's code(s), methodology, nodalization and assumptions. Section 5 presents the results of blind and open simulations, and comparison against experimental measurements for selected transient variables.

Finally, Section 6 summarizes lessons learned from the ICSP, with conclusions and recommendations given in Section 7.

2. ACCIDENT PHENOMENOLOGY AND RELEVANCE TO SAFETY

An important safety feature of HWRs is the ability to use the moderator as a passive backup heat sink during emergencies that involve overheating of the fuel. The pressure tube in a CANDU fuel channel is normally separated from the surrounding calandria tube by a CO_2 filled annulus gap, as shown in Fig. 1. This gas filled gap thermally isolates the pressure tube from the calandria tube during normal operation. The deformation and subsequent ballooning contact of an overheated pressure tube with the calandria tube rely on the combined performance of the pressure tube and calandria tube during the post-contact period to maintain channel integrity. The calandria tube, which is submerged in a subcooled pool of moderator, supports and cools the pressure tube upon contact, arresting the outward deformation. The calandria tubes are thinner than the pressure tubes but are directly cooled by the surrounding moderator.

Heat transfer between the pressure tube and the calandria tube under normal operating conditions occurs primarily by conduction through the gas and by thermal radiation. The moderator carries away the heat transferred radially out of the fuel channel in an undeformed geometry of the channel. During accident conditions, however, the pressure tubes undergo plastic deformation and radial growth. This plastic deformation is a permanent dimensional change resulting from the effects of pressure and temperature and is known as pressure tube ballooning. When a pressure tube balloons into contact with the calandria tube, the resultant contact heat transfer significantly and almost instantaneously increases the rate of heat transfer to the calandria tube, and subsequently, to the moderator. The rate of heat transfer to the calandria tube is determined by the temperature difference between the pressure tube and the calandria tube and by the contact heat transfer coefficient, which depends on the contact pressure. The temperature of the calandria tube is determined by the moderator subcooling and the heat transfer coefficient between the calandria tube and the moderator.

At the time of contact, the calandria tube experiences a large increase in heat flux at the contact locations, as stored heat is rejected from the pressure tube to the cooler calandria tube. If the heat flux on the outer surface of the calandria tube exceeds the Critical Heat Flux (CHF), film boiling (dryout) may occur on the surface of the calandria tube. If the area in dryout is sufficiently large and the dryout is prolonged, the pressure tube/calandria tube combination can continue to heat up and strain radially, ultimately leading to fuel channel rupture.

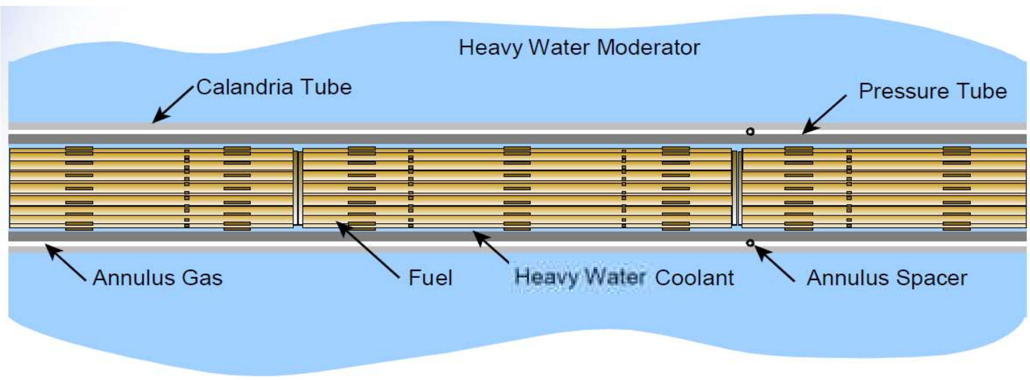

FIG. 1. HWR fuel channel details.

The moderator subcooling limits, required to avoid dryout conditions that could challenge fuel channel integrity, are defined by the contact boiling curve. The contact boiling curve generated from data collected in contact boiling experiments performed in the 1980s (Fig. 2) relates moderator subcooling and pressure tube contact temperature to the occurrence of immediate quench (or rewet), patchy film boiling or extensive film boiling [1]. The boundary between immediate quench and patchy film boiling defines the moderator subcooling limits used in safety analysis of CANDU reactors that use standard calandria tubes. More recent work has shown that glass-peening the outside surface of the calandria tube can significantly reduce and/or delay the occurrence of film boiling [2].

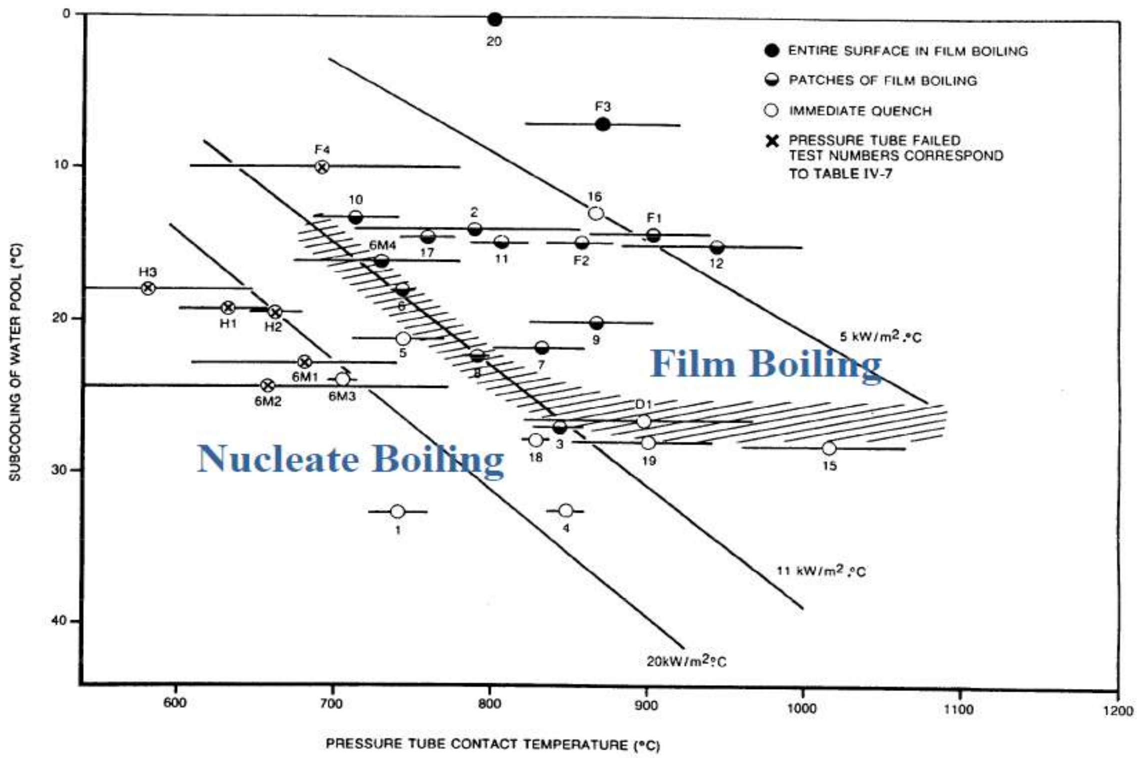

FIG. 2. Contact boiling curve [1].

In 2000, the contact boiling curve was updated with data collected from contact boiling experiments performed since the publication of the original contact boiling curve. The new experimental data showed that the occurrence of small patches of film boiling did not necessarily threaten fuel channel integrity [2]. If the area in dryout was modest (less than 15%) and the time to rewet was short (less than 20 s), fuel channel integrity was not challenged. The CANDU industry has adopted a limit of 2% CT strain to demonstrate fuel channel integrity, based on these full-scale contact boiling experiments. To confirm this limit, further test have recently been performed and have demonstrated the importance of PT-CT contact conductance immediately after contact and during the period of patchy film boiling [3].

The ICSP was performed to demonstrate the analysis capabilities of Member States to calculate the backup heat sink potential of the moderator during accidents and the test conditions were selected to fill an area of the contact boiling where more data is desirable.

Most participants from Member States used their safety analysis codes to perform a double-blind simulation, meaning the actual test conditions are unknown, using nominal pre-test initial/boundary conditions to calculate pressure tube and calandria tube temperature transients and evaluate integrity of the fuel channel. The initial/boundary conditions for double-blind calculation were the internal pressure of the pressure tube, heater power, and moderator subcooling (water temperature). Following the double-blind simulations, the contact boiling experiment was performed with target initial/boundary conditions as close as possible to the double-blind initial/boundary conditions given to the analysts. Following the double-blind simulations, the actual initial/boundary conditions obtained in the test were provided to participants for the blind simulation. The test data was distributed to participants after the blind simulation results were submitted and used for comparison with the actual test data in the open simulations.

3. FUEL CHANNEL HIGH TEMPERATURE HEAT TRANSFER TEST FACILITY

The Fuel Channel High Temperature Heat Transfer laboratory in CNL's Chalk River Laboratories has an experimental facility designed to study the behaviour of CANDU fuel channels under postulated accident scenarios involving insufficient primary and/or secondary emergency cooling [4]. The facility can conduct full scale experiments and investigate the integrated thermal–chemical–mechanical response of a CANDU fuel channel under normal and abnormal conditions. The experiments in the laboratory investigate the conditions and processes for transferring residual and decay heat from the fuel to the moderator. The laboratory provides data for validation of codes used in the safety analysis of CANDU reactors.

3.1. DESCRIPTION OF CONTACT BOILING EXPERIMENTS

The test section consists of a 1750 mm long section of Zr/2.5Nb pressure tube mounted concentrically inside a 1700 mm long section of Zircaloy-2 calandria tube, shown in Fig. 3 Before assembling the test apparatus, the pressure tube and calandria tube surfaces are cleaned with isopropyl alcohol to remove any organic contaminants. The calandria tube inside surface and the pressure tube outside surface receive special attention to ensure that the thermal contact conductance between the tubes during contact is not influenced by surface contamination. Both the pressure tube and calandria tube are free to expand at one end during heating.

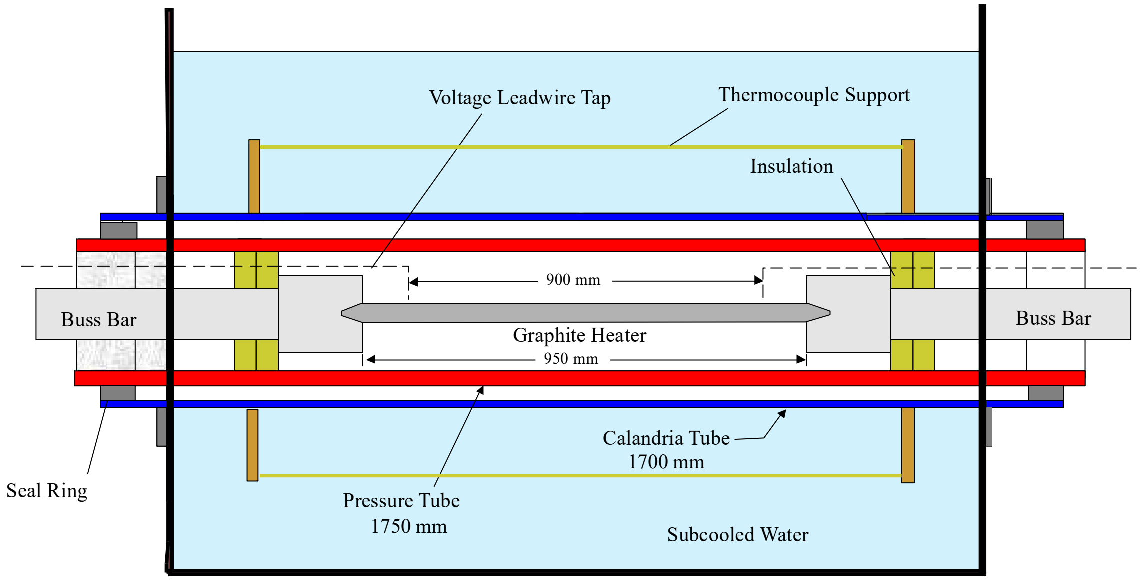

FIG. 3. Experimental apparatus for ICSP test.

The test section is surrounded by heated distilled light water in an open tank 750 mm high, 1425 mm long and 600 mm wide. The top of the calandria tube is approximately 425 mm from the bottom of the tank and 180 mm below the surface of the water at the start of the test. The walls of the tank are equipped with Lexan windows to allow observation and video recording of the boiling on the outside surface of the calandria tube during the test.

A uniform 38 mm diameter graphite rod heater, offset 9.5 mm toward the bottom of the pressure tube, is used to heat the test section. The 9.5 mm offset attempts to minimize the free convection induced circumferential temperature gradient on the pressure tube during heating. When the heater is concentric with the tube, convection in the pressurizing gas causes significantly higher temperatures at the top of the tube than at the bottom. The heater is held in place by water cooled stainless steel buss bars with Zircaloy end fittings. Compression springs are used to keep the buss bars in contact with the ends of the heater, which are tapered in a 60° cone to match the conical receptacles in the buss bars. The heater is free to expand during heating. A gas cylinder is used to equalize the pressure inside the pressure tube and the buss bars. Three 25 mm thick Zirconia disk insulators are placed at the end of each buss bar to thermally insulate the pressure tube end-fitting assembly from the heater.

Argon gas is supplied to the inside of the pressure tube via a pressure control system with a 30 l surge tank online. The gas in the surge tank is heated to 300 °C. Carbon dioxide is supplied directly from gas cylinders to the pressure tube/calandria tube annulus and maintained at a very low flowrate.

The pressure tube section was identified for traceability of materials and has adequate documentation to trace the pedigree from ingot to final product. Typically, the tubes available for testing are manufactured by Nu Tech from a quad-melted ingot supplied by Teledyne Wah Chang. The nominal wall thickness of the pressure tube is 4.40 mm.

The calandria tube section is from typical calandria tubes available in the laboratory, an as received seam welded tube manufactured by Zircatec Precision Industries. The seam weld in the test is oriented at 45° from the bottom. The nominal wall thickness of the calandria tube is 1.42 mm. Table 1 summarizes the test section dimensions.

TABLE 1. TEST SECTION DIMENSIONS

COMPONENT	INSIDE DIAMETER (mm)	OUTSIDE DIAMETER (mm)	THICKNESS (mm)
Pressure tube (PT)	103.8	112.4	4.40
Calandria tube (CT)	129.4	132.2	1.42
Graphite heater rod (GH)		38	

3.2. INSTRUMENTATION AND UNCERTAINTIES

Power is supplied by a 500-kW direct-current power supply and controlled using constant power mode with current feedback. The power supplied to the graphite heater is determined using a 10000-A shunt to measure the current, voltage taps across the buss bars to measure the total circuit voltage and voltage taps on the heater to measure the heater voltage. The voltage taps on the heater are typically 900 mm apart.

Rosemount pressure transducers are used to measure the test section pressure and the LabVIEW data acquisition system records the pressure as gauge pressure in MPa(g). The pressure is controlled by an automatic pressure control system with the ability to feed and bleed gas as required to maintain set point pressure. The annulus pressure is not measured but is assumed to be near atmospheric since the annulus is not a closed system but vented to the lab room.

The pressure tube and calandria tube are instrumented with thermocouples at five axial rings spaced 150 mm apart along the test section heated length (Fig. 4). Fifty-four thermocouples are used to monitor the test section temperature: fourteen embedded halfway into the pressure tube wall (Fig. 5) and forty on the outside surface of the calandria tube. The fourteen pressure tube thermocouples (numbered 0 to 13 in Fig. 4 and labelled TC0 to TC13 in Fig. 10 and beyond) are made from special grade, special limits of error, 1 mm diameter, Inconel-clad Type K thermocouples. These thermocouples are swaged to 0.5 mm diameter and inserted into blind holes drilled halfway through the pressure tube wall (Fig. 5). The calandria tube thermocouples (numbered 14 to 53 in Fig. 4 and labelled TC14 to TC53 in Fig. 10 and beyond) are also special grade, special limits of error, Teflon insulated Type K thermocouples with sensing elements of 0.13 mm diameter. The tips of these thermocouple wires are spot welded directly onto the outer surface of the calandria tube at five axial rings corresponding to the instrumented locations on the pressure tube.

Four platinum Resistance Temperature Detectors (RTDs) placed inside the water tank are used to measure the water temperature surrounding the calandria tube. Two RTDs are located at the test section axial centreline: one 50 mm above the top surface and the other 50 mm below the bottom surface of the tube. The other two RTDs measured the bulk water temperature near the ends of the test section at a depth of a horizontal plane passing through the calandria tube centre.

Two video cameras are used to record the entire test through windows on either side of the water tank (north and south views). This allows the observation of the boiling behaviour on the outside of the calandria tube during the test. Another camera provides an overhead view of the test enclosure during the experiment.

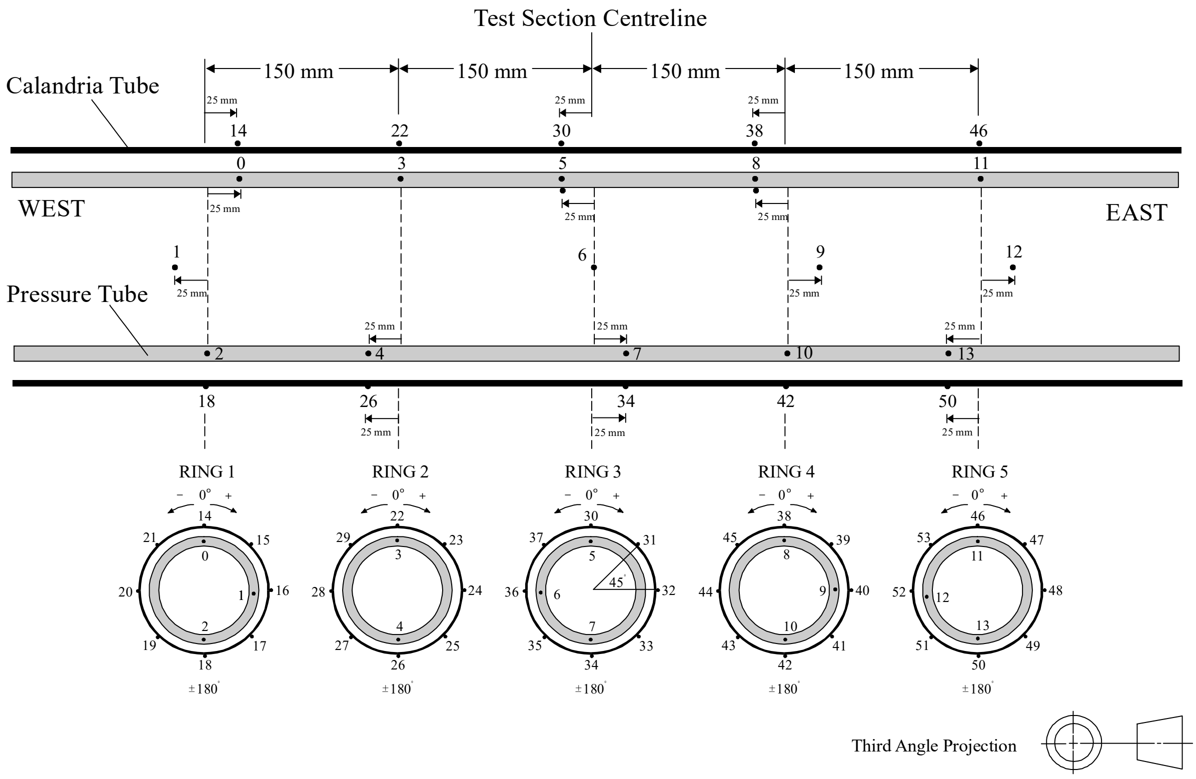

FIG. 4. Locations of pressure tube and calandria tube thermocouples.

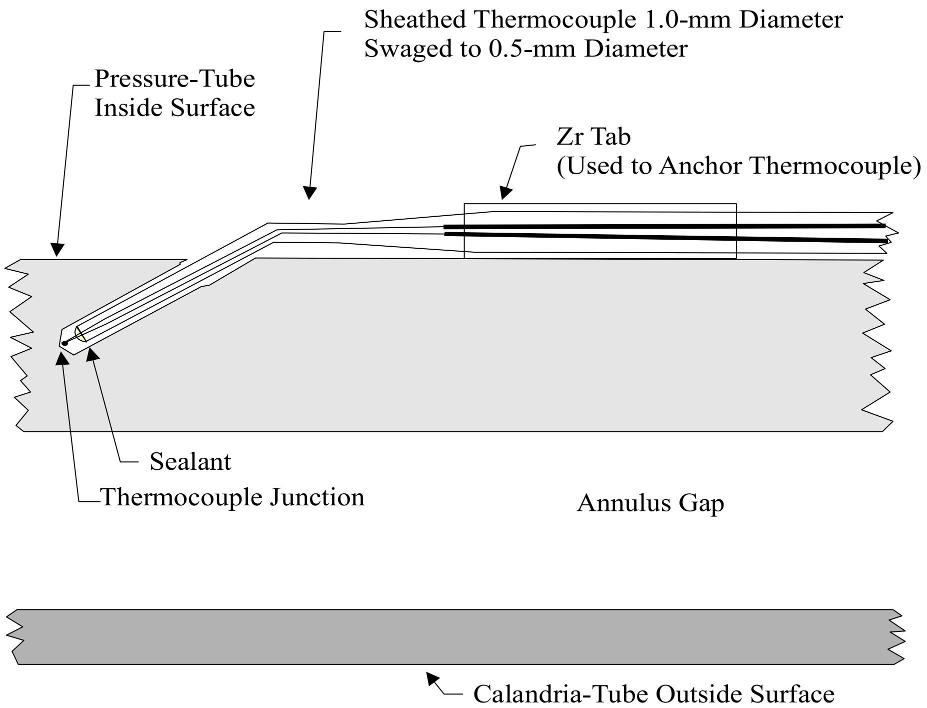

Note: Not drawn to scale.

FIG. 5. Sketch of an embedded pressure tube thermocouple (AECL Patented).

3.3. MATERIAL PROPERTIES

All participants used the below material properties, unless stated otherwise in the respective sections on assumptions in Section 4.

Pressure tube and calandria tube, using Zircaloy properties:

For both PT and CT the Zircaloy properties given by AECL [5] and in MATPRO [6] are used. Zircaloy density is 6440 kg/m^3. For ballooning or transverse creep calculations, the strain rate correlations developed by Shewfelt et al., 1984 are used [7]. The mechanism of transverse creep from 450ºC to 1200ºC is reported to be due to power law creep and grain boundary sliding. The correlation for transverse deformation rate for temperature range 450ºC to 850ºC is given by:

$$\dot{\varepsilon} = 1.3 \times 10^{-5} \sigma^{9} \exp\left(\frac{-36600}{T}\right) + \frac{5.7 \times 10^{7} \sigma^{1.8} \exp\left(\frac{-29200}{T}\right)}{\left[1 + 2 \times 10^{10} \int_{t_1}^{t} \exp\left(\frac{-29200}{T}\right) dt\right]^{0.42}} \quad (1)$$

For the temperature range 850ºC to 1200ºC the transverse deformation rate is given by:

$$\dot{\varepsilon} = 10.4 \sigma^{3.4} \exp\left(\frac{-19600}{T}\right) + \frac{3.5 \times 10^{4} \sigma^{1.4} \exp\left(\frac{-19600}{T}\right)}{\left[1 + 274 \int_{t_2}^{t} \exp\left(\frac{-1960}{T}\right) (T - 1105)^{3.72} dt\right]} \quad (2)$$

where $\dot{\varepsilon}$ is the transverse deformation rate in s^{-1}, σ is the transverse stress in MPa, t is the time in s, T is the temperature in K, t_1 is the time when T = 973 K (699.85ºC), and t_2 is the time when T = 1123 K (849.85ºC).

Zircaloy thermal conductivity (Fig. 6) for temperatures less than 2098 K (1825°C) is described by:

$$k_{\mathrm{Zr}} = 7.5 + 2.09 \times 10^{-2}T - 1.45 \times T^2 + 7.67 \times 10^{-9}T^3 \tag{3}$$

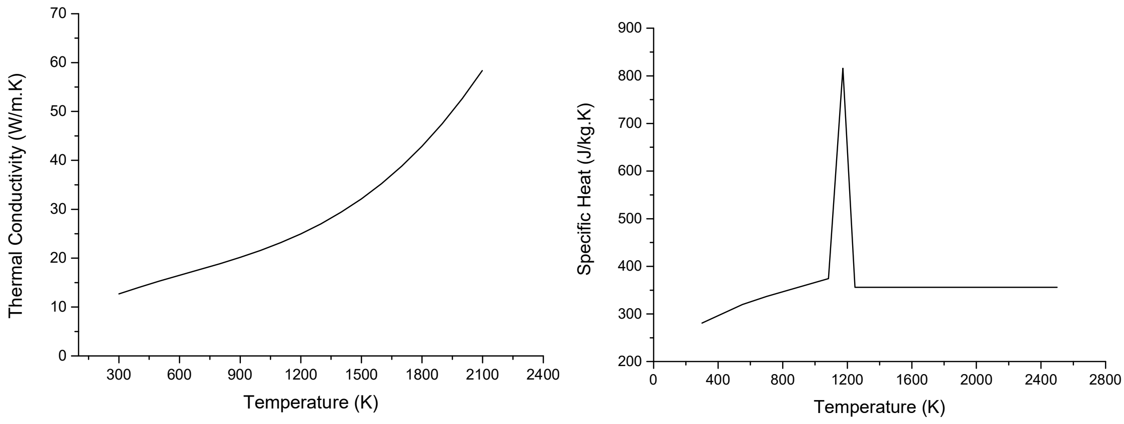

(a) *(b)*

FIG. 6. Zircaloy (a) thermal conductivity and (b) specific heat.

The behaviour of Zircaloy specific heat is shown in Fig. 6 (b). Graphite density was taken as 1780 kg/m^3 and Fig. 7 below shows the variation of thermal conductivity and specific heat capacity of graphite, respectively.

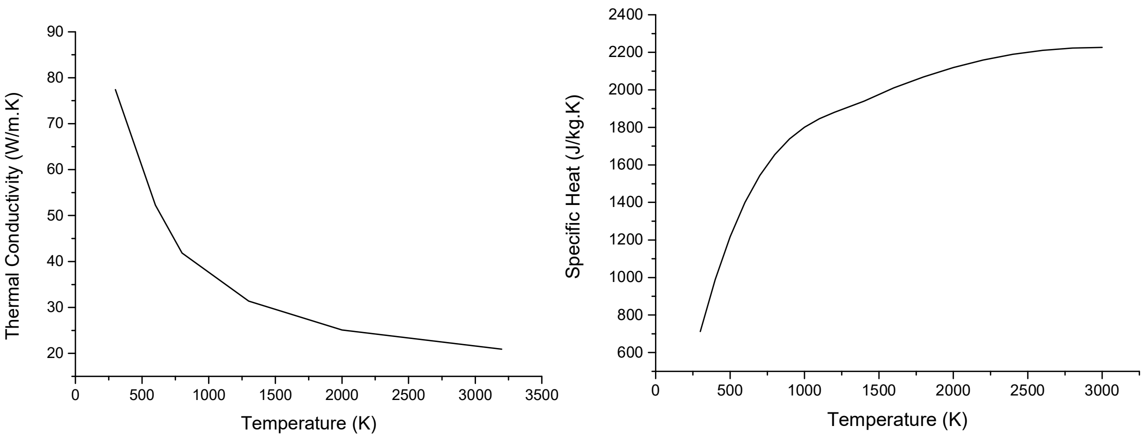

(a) *(b)*

FIG. 7. Graphite (a) thermal conductivity and (b) specific heat [5].

3.4. TEST INITIAL CONDITIONS AND PROCEDURE

Safety analysis codes are validated against full scale contact boiling experiments conducted using specific initial conditions relevant to CANDU operation, such as channel power, pressure, and moderator subcooling. The transient pressure tube and calandria tube temperatures, the extent of dryout on the outside of the calandria tube, and failures of the pressure tube and/or the calandria tube (if any) are the outcomes of these experiments. The particular test of the ICSP was performed to demonstrate the analysis capabilities of Member

States to calculate the backup heat sink potential of the moderator during accident conditions. Furthermore, the initial test conditions and the heat-up rate are selected with an objective that the test conditions fill an area of the contact boiling (Fig. 2) where more data is desirable. The nominal test conditions are summarized in Table 2.

TABLE 2. TARGET TEST CONDITIONS

TEST PRESSURE	HEATER POWER (V-tap)	PRESSURE TUBE HEAT-UP RATE	SUBCOOLING
3.5 MPa(g)	140 kW	20 °C/s	30 °C

3.5. MEASUREMENTS AND RESULTS

The experiment investigated radiation and convection heat transfer from the heater to the pressure tube, pressure tube deformation, pressure tube to calandria tube contact and the resulting heat transfer, calandria tube deformation and heat transfer to the moderator water. Test conditions comprised a transient heat up where the pressure tube experienced an average heat-up rate of 21ºC/s. The internal pressure was 3.5 MPa and the moderator was at 70ºC, corresponding to 30°C subcooling. Important measurements include transient temperature on both pressure and calandria tubes, shown in Fig. 8, post-test tube thicknesses, and dry-patch areas on the calandria tube outside surface (Fig. 9 shows two post-test views). Fig. 8 shows pressure tube and calandria tube temperatures measured at the axial centre of the test section (Ring 3). Video footage clearly showed nucleate, intermittent, and film boiling regions following contact, and the development and rewetting of dry-patches. The test results were of high quality and self-consistent, achieving the objectives of displaying in a qualitative and quantitative way the important behaviours and providing good validation data.

A heat balance was performed by using the transient measured temperatures of the main components: the heater, pressure tube, calandria tube, and water pool. It revealed that during the first 40 s more than 95% of the electrical energy input (~147 kW) is stored in the heater itself, after that, until contact at 72 s; about 50% heats the pressure tube providing a nearly constant heat-up rate of 21ºC/s. Upon contact, about ¼ of the pressure tube stored heat is transferred to the calandria tube and surrounding water in the first second, after which, until the end of the test, the pressure and calandria tubes maintain nearly constant temperatures, and heat transfer is effective and nearly constant from the heater to the surrounding water pool. This condition is referred to as the ‘moderator providing an effective heat sink’.

Ignoring thermocouple TC0 inside the pressure tube, which most likely partially detached early in the test, Fig. 10 shows a relatively uniform heat up of the top of the pressure tube to 850–920°C before contacting the calandria tube and cooling down as a result of the contact heat transfer. Contact occurred at 71 to 74 s depending on location, first along the bottom, and then spreading towards the top. Slightly higher contact temperatures were reached at the bottom, but larger and more prolonged dryout occurred near the top. Fig. 9 compares the dryout patches on the top and bottom halves of the calandria tube, as indicated by the clearly visible post-test oxide patches.

A peak calandria tube temperature of 650°C was measured and complete rewet occurred after 21 s, although many smaller dry-patches rewet after only a few seconds. During this time up to 22% of its surface was in dryout. This resulted in a local maximum CT strain of 3% inside the largest dryout patch (see Fig. 9(a)). Post-test measurements of the pressure tube thickness revealed that, with an average strain of 15% (corresponding to full ballooning) the local strains varied from 9% to 29%, with the largest strains near the bottom. This is because of the higher heating rate and ultimate contact temperatures near the bottom, as compared to the sides and top of the pressure tube.

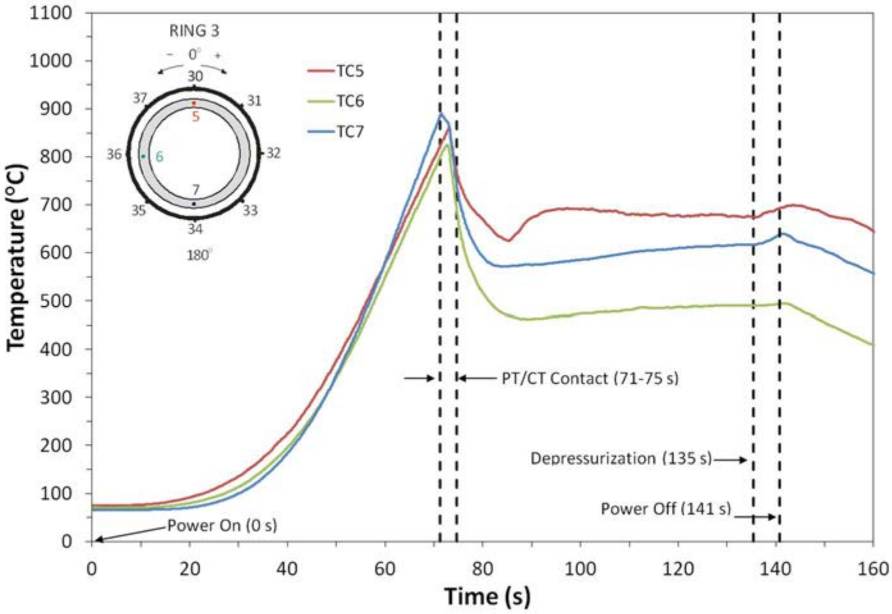

(a)

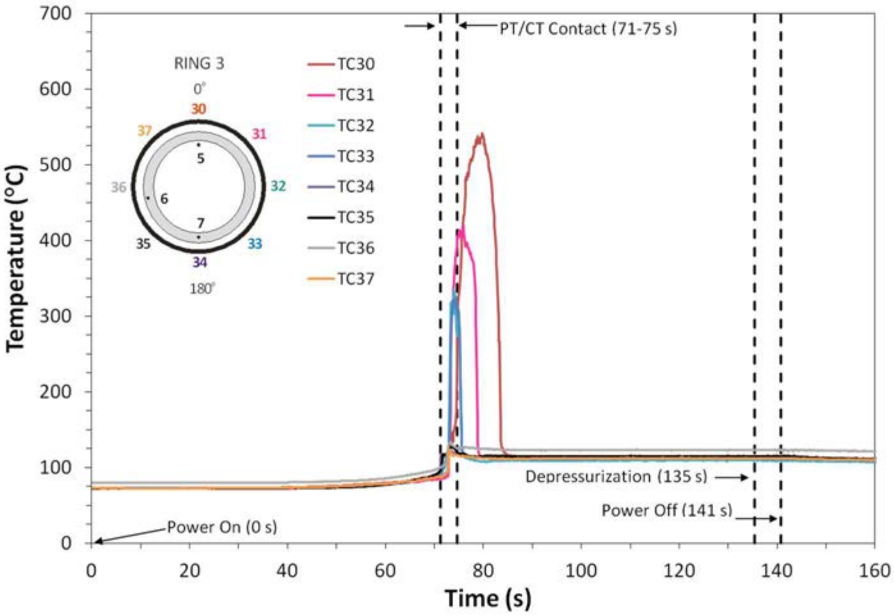

(b)

FIG. 8. (a) Pressure tube and (b) calandria tube temperatures at Ring 3, axial centreline.

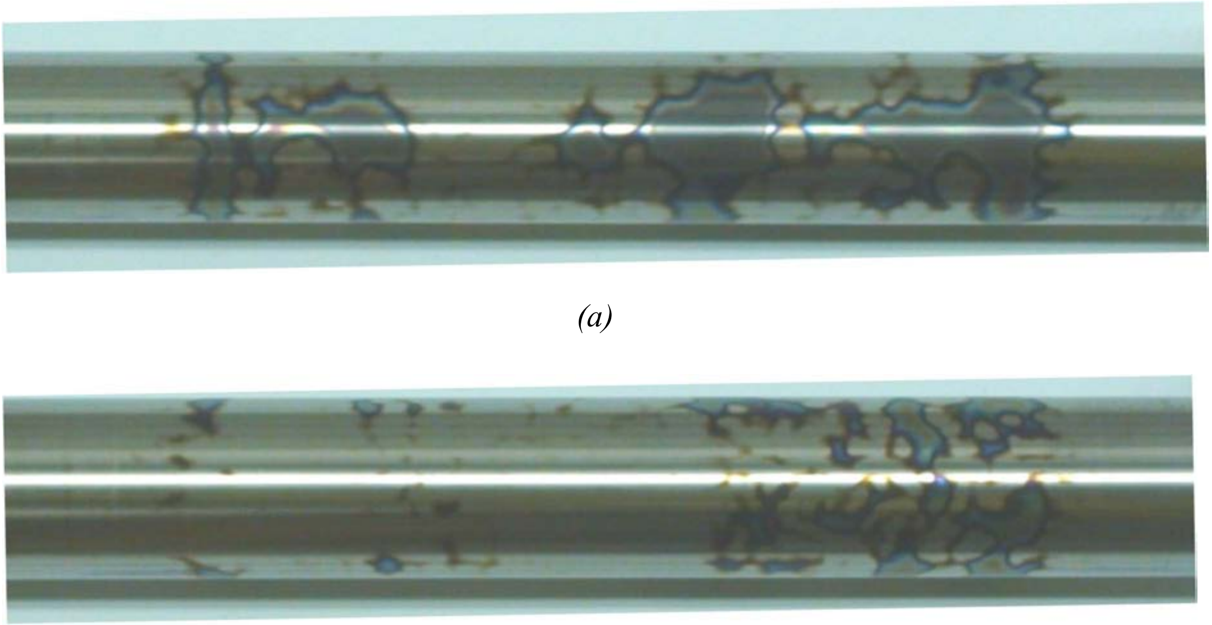

(a)

(b)

FIG. 9. Photos of (a) top and (b) bottom of calandria tube outside surface after the experiment.

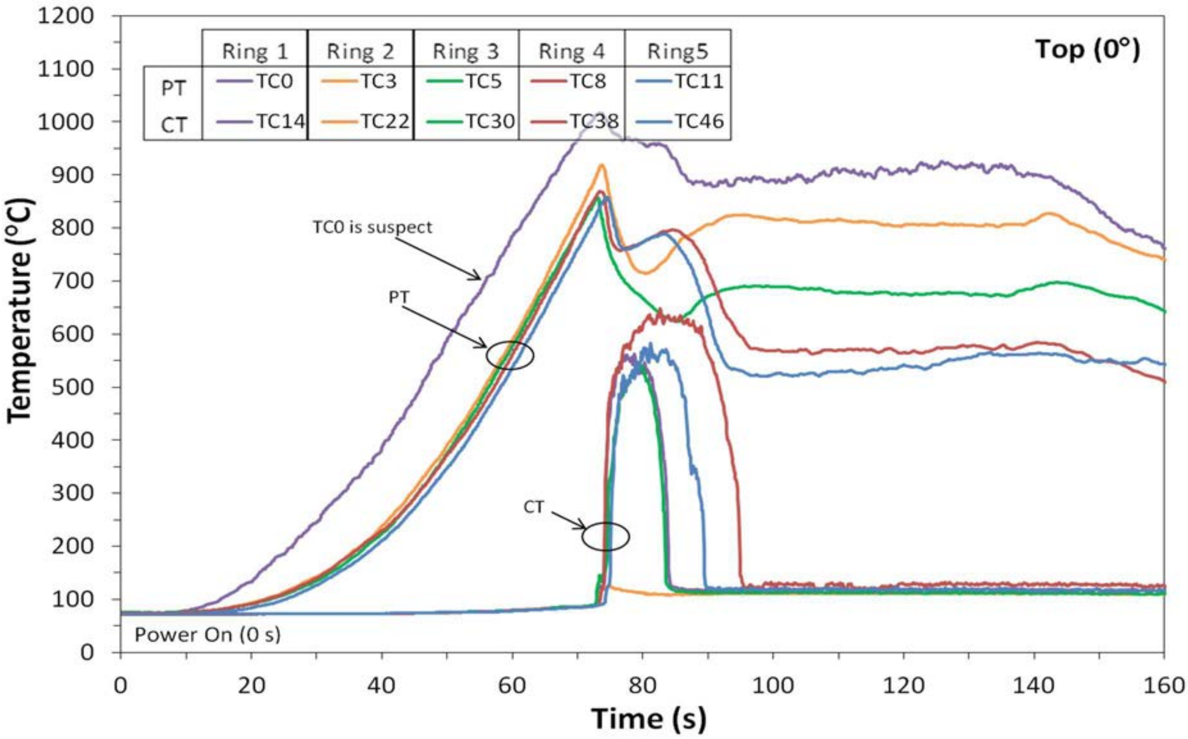

FIG. 10. Measured temperatures at the top of pressure tube and on calandria tube.

4. PARTICIPANTS, CODES AND MODELS

4.1. GROUND RULES FOR BLIND AND OPEN CALCULATIONS

The participants from Member States were expected to use safety analysis codes to perform a double-blind simulation using pre-test initial/boundary conditions and to report both on the pressure tube and calandria tube temperature transients and assess the integrity of the fuel channel. The initial/boundary conditions for the double-blind calculation were the internal pressure of the pressure tube, heater power, and moderator subcooling (water temperature). Following the double-blind simulations, the contact boiling experiment was performed with target initial/boundary conditions as close as possible to the double-blind initial/boundary conditions given to the analysts. The test was completed following the double-blind simulations and then the actual initial/boundary conditions obtained in the test was provided to participants for a blind simulation. The test data was distributed to participants only after the blind simulation results were submitted. The participants were then asked to compare the simulation results and the actual test data. The calculated results were returned to CNL's Chalk River Laboratories in an Excel spreadsheet template provided to the participants. These calculations were expected to be completed and reported in SI units and the temperatures were expected to be at the location of the thermocouple placed in the test. The participants were requested to make a clear statement whether the fuel channel ruptured or successfully rewet during the transient based on strain calculations and failure criteria.

Following the blind calculations and considering some substantial differences in participants' assumptions, a detailed checklist was developed for the open calculations (Appendix).

4.2. GENERAL PURPOSE AND INTEGRAL COMPUTER CODES

4.2.1. ABAQUS

Coupled thermal and structural analysis is performed using ABAQUS [8]. The heat transfer analysis implements radiation heat transfer from heater to PT and from PT to CT. Physics based variable contact conductance between PT–CT is modelled. Convection from outer surface of CT to water is also considered based on flow regime. Finite-Element Model (FEM) based structural analysis included elastic creep, elasto-plastic and creep of the PT–CT assembly under thermal and mechanical loading. The description of the thermal-mechanical creep analysis is provided in Section 4.4.1.

4.2.2. CATHENA

CATHENA is a 1D thermalhydraulic code that has solid, thermalhydraulic, and heat transfer models. These models implemented in CATHENA-MOD 3.5d/Rev 2 were used in the study [9]. The graphite rod, pressure tube, and calandria tube were modelled as solid components with an axial length of 1 m. These components were modelled using the Generalized Heat Transfer Package (GENHTP) models in the code. All solid components were modelled using 18 circumferential sectors. The heater, pressure tube, and calandria tube were modelled with 10, 11 and 10 radial nodes, respectively. An odd number of radial nodes are used on the pressure tube to ensure that a computational node is located at the mid-radius of the pressure tube. The calandria tube is modelled using the default material properties for Zircaloy in CATHENA. The pressure tube is also modelled the default material properties for Zircaloy.

The heater rod/pressure tube annulus, pressure tube/calandria tube annulus, and the open tank are modelled as horizontal pipe components, respectively, containing stagnant argon at 4 MPa, stagnant CO_2 at atmospheric pressure, and water at atmospheric pressure. All components have an axial length of 1 m. The calandria tube is initialized at a temperature value of 76°C, which is the water bath's temperature at the start of the experiment. The pressure tube and heater rod are initialized with slightly lower temperature values of 64°C and 60°C, respectively.

All pipe and solid components are modelled with one axial node, thus yielding a two-dimensional model of the ICSP experiment. Heat generation within the heater rod is realized by applying a spatially uniform heat generation value corresponding to the time dependent thermal power data.

The power is sustained at a value of 118 kW/m for 190 s, thus allowing sufficient time for the prediction of the rewet or failure of the calandria tube. To account for free convection, the eccentricity in the heater is not modelled. Heat transfer between the GENHTP solid components and thermalhydraulic pipe components are calculated by the default heat transfer correlations in CATHENA. However, the critical heat flux value is systematically increased from the top sector to the bottom sector by a value of 4% so that dryout does not instantaneously occur on the entire calandria tube surface, if the conditions are favourable for the film boiling regime. Hence, should dryout occur, it will first happen on the top two sectors (5.6% of the surface) before spreading to the other surfaces of the calandria tube, and vice-versa for the rewetting phenomenon.

Radiation heat transfer between the solid components that define each annulus was calculated using view factors obtained using the GEOFAC utility. Temperature-independent emissivity values of 0.8, 0.7, and 0.325 were assumed for the heater rod, pressure tube, and calandria tube, respectively.

The non-uniform deformation of the pressure tube and calandria tube were calculated in CATHENA. Additional information not output by CATHENA by default, such as calandria tube strain values, are calculated using system control models provided in CATHENA. Contact resistance values are specified to mimic an assumed temporal distribution of contact resistance.

4.2.3. COMSOL

For the blind calculation of the ICSP experiment on heavy water reactor moderator subcooling requirements, the COMSOL Multiphysics code [10] is used to simulate plastic deformation of a pressure tube as a result of the interaction of stress and temperature. It is shown that the thermal stress model of COMSOL is compatible to simulate the multiple heat transfers (including the radiation heat transfer and heat conduction) and stress strain in the simplified two-dimensional problem. The benchmark test result for radiation heat transfer is in good agreement with the analytical solution for the concentric configuration of pressure tube and calandria tube. Since the original strain model of COMSOL only considers an elastic deformation with thermal expansion coefficient, the pressure tube/calandria tube contact cannot be predicted in the ICSP problem. Therefore, the plastic deformation model by the Shewfelt and Godin [7], widely used in the CANDU fuel channel analysis, is implemented to the strain equation of COMSOL. The heat up of pressure tube, the strain rate, and the contact time of the pressure tube/calandria tube are calculated with the boundary conditions given for blind calculation of the ICSP experiment.

4.2.4. RELAP5/SCDAP

RELAP5/Mod3.4 was used to model the test section upper and lower halves. The principal feature of the RELAP5 system code is the use of a two-fluid, non-equilibrium, non-homogeneous, hydrodynamic model for transient simulation of the two-phase system behaviour. RELAP5 has a reflood model with changes made to interfacial heat transfer, interfacial drag, and wall heat transfer. This model is selected by user option for the heat transfer at the PT–CT heat structures to estimate the dryout and rewet phenomena observed in the experiments.

4.2.5. TUF

The model results are predicted using the TUF (Two Unequal Fluids) code, version 1.2.6 (henceforth referred to as TUF) [11]. TUF is a one-dimensional code used to simulate fuel channel thermalhydraulics under steady state and transient conditions. The new moderator subcooling methodology was used in the TUF simulations for this analysis. This model was developed and implemented in TUF based on Reference [12].

The model consists of two TUF runs, one steady state run followed by a transient run. The steady state run was developed to create the restart file necessary for the transient. The steady state run describes the analysed geometry, material properties, and other TUF options. During the transient run the heater power and the inner pressure of the pressure tube were varied according to experimental measurements.

4.3. SPECIAL PURPOSE CODES, METHODS AND MODELS

4.3.1. BARC

Two explicitly coupled computational modules namely (a) HEATCATS [13] and (b) PTCREEP [14] were used in simulating the simultaneous creep deformation and the heat transfer in the channel. 'HEATCATS' predicts 2D temperatures in 'r-θ' across the channel cross-section which includes the components such as graphite pin heater, PT and CT. This module also simulates the boiling around CT and calculates the average temperature rise of the surrounding water. PTCREEP predicts average radial creep dilation of the PT based on predicted temperatures and internal pressure. The change in PT geometry due to creep deformation is communicated to the 'HEATCATS' at each time interval. On PT/CT contact, the conductance is calculated based on the semi-empirical model developed by Yovanovich [15] with the contact pressure being evaluated through a simplistic contact zone model described in Section 4.4.4.

4.3.2. CNSC Model

The mathematical models given in Section 4.4.5 below were implemented in MATLAB R2013a scripts. Three modules were developed:

— Main simulation module; it contains all geometrical values, material properties, correlations, physical constants and numerical solvers.
— View factors calculation module, which contains geometrical data relevant to view factors calculation for modelling radiative heat transfer between the heater and the Pressure Tube.

— Plotting and post-processing module, which contains all geometrical values relevant to nodalization, 2D and 3D plotting subroutines, and post-processing subroutines, such as calculation of Pressure Tube heat-up rates or percentage of calandria surface dryout area.

4.3.3. KANUPP Model

An indigenous code has been developed to simulate the experiment. The code solves conduction equations for Graphite Heater (GH), Pressure Tube (PT) and Calandria Tube (CT) using implicit finite difference method in one dimension. The moderator heat transfer package uses a set of correlations to describe the boiling curve involving natural convection, nucleate boiling, CHF, transition and film boiling. The dominant mode of heat transfer is radiation between the three metallic cylinders. Plastic deformation of the pressure tube due to heat up and internal argon gas pressure is modelled by Shewfelt equations [7]. Temperature-dependent thermal properties of the materials involved are used for setting up the heat balance equations. The current version is called version ‘zero’ and future improvements will be done in the upcoming versions.

4.4. PARTICIPANTS’ IDEALIZATIONS AND ASSUMPTIONS

4.4.1. AERB ABAQUS Model

The AERB model, as implemented in ABAQUS, has been described in [16] and is for completeness also briefly described here.

The PT and CT are modelled with a finite element mesh and half-symmetry along the YZ plane considering symmetry of the geometry, boundary condition and loading in YZ plane, as shown in Fig. 11 with an initial temperature of 72.5°C. The solid model has been meshed with 3D Iso-Parametric linear hexahedral elements with reduced integration and hourglass control (coupled thermal structural element). The mesh consists of 5891 elements and 12 152 nodes. The true stress and true plastic strain are used to model plasticity in cases where elastoplastic deformation is considered. The true stress vs true plastic strain curves are derived from data obtained from experimental work done by Dureja et al., 2011 [17].

The initial temperature of the heater and the water was 70°C and initial argon pressure was 3.6 MPa(a).

Contact pressure is developed due to interaction between PT–CT as the PT deforms by ballooning and contacts the CT. In ABAQUS, contact pressure due to interaction between PT–CT is estimated, and gap conductance based on this contact pressure is used in calculations. The contact conductance data provided by AECL is used in the estimation of gap conductance as given below.

$$h_{\text{contact}} = 10\,\frac{\text{kW}}{\text{m}^2\text{K}} \text{ for } 1 \text{ MPa} \leq P < 3 \text{ MPa} \tag{4}$$

$$h_{\text{contact}} = 20\,\frac{\text{kW}}{\text{m}^2\text{K}} \text{ for } 3 \text{ MPa} \leq P < 6 \text{ MPa} \tag{5}$$

Various heat transfer regimes for heat transfer from outer CT surface are modelled. Free convection correlation given by Churchill & Chu [18] is considered for heat transfer by natural convection. In pool boiling regime, Thom correlation is considered for nucleate boiling and

Zuber-Griffith correlation for CHF [19]. Transition boiling from CHF to quench, or rewet, temperature is calculated using Bjonard and Griffith correlation [20]. Minimum film boiling quench temperature is used as supplied by COG. Heat transfer corresponding to nucleate boiling is considered for quenching/rewetting.

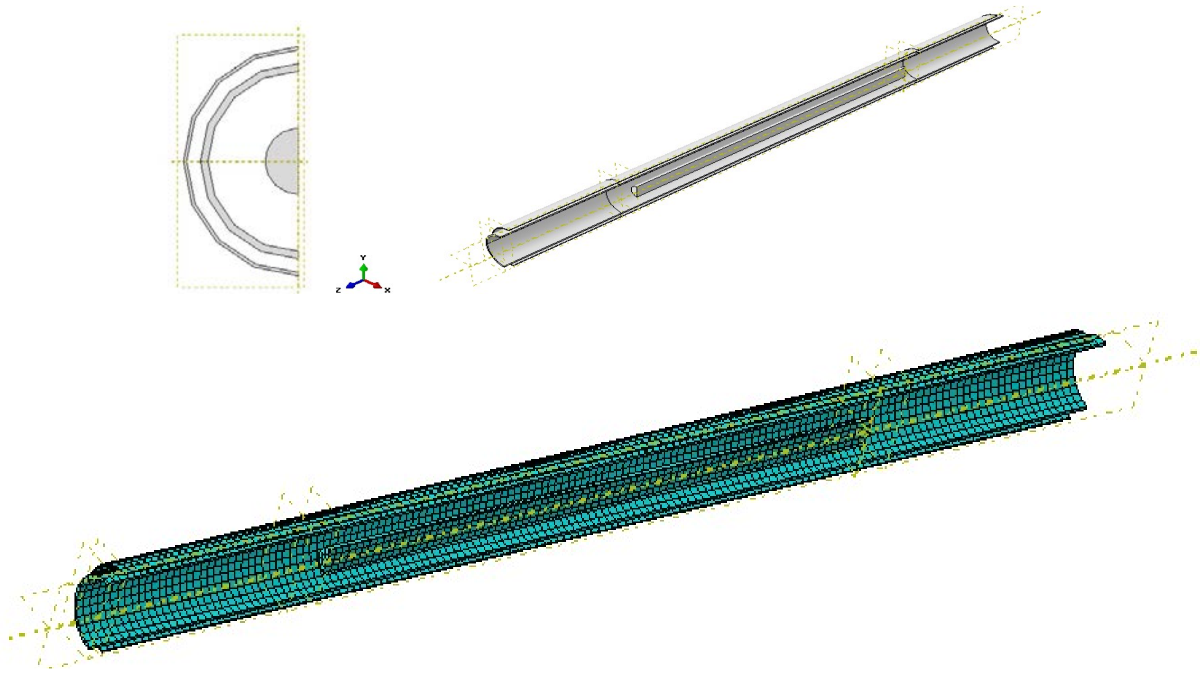

FIG. 11. Solid model and finite element discretization [16].

4.4.1.1. Changes from blind to open calculations

- — Blind calculation considered the approximate surface radiation but present study (open calculation) considers gap radiation feature.
- — Pool boiling correlation based on various regimes was used to define heat transfer outside the calandria tube in open calculation compared to limited modelling of boiling on the outer surface of CT in blind calculations.
- — Blind calculation used specific heat of PT and CT from literature whereas; in open calculation it is provided by AECL.
- — In blind calculation, contact conductance variation with gap between PT and CT was used with maximum contact conductance of 8000 W/m^2K but in open calculation, contact conductance variation with pressure is used as suggested by AECL.
- — The open calculation creep subroutine uses explicit integration scheme and coupled creep and plasticity uses implicit integration scheme, whereas in the blind calculations, only implicit integration scheme was considered.
- — Improved contact algorithm is used to prevent geometric interference between PT and CT in open calculation.
- — Nodalization to capture coupled PT–CT deformation.

4.4.2. AERB RELAP5 Model

RELAP5/Mod3.4 was used to model the test section upper and lower halves as shown in Fig. 12. The region between the heater and the pressure tube is modelled as pipe component. System pressure is maintained by connecting the pipe component to a large volume with constant pressure and temperature. The graphite heater is modelled as heat structure having 7 axial nodes and 10 radial nodes. The pressure tube and calandria tube (gap filled with CO_2) is divided into two semi cylinders and each half is modelled using 7 heat structure components with 8 radial nodes to estimate the temperature variation and contact time of the lower and upper half of PT/CT. The water tank is modelled as 33 vertical pipe components; 3 vertical pipes along the width and 11 along the length and each vertical pipe with 7 nodes are connected by multiple cross flow junctions to simulate the natural convection of fluid due to the temperature difference at different locations in the tank. The nodalization of the water tank is shown in Fig. 13. Lower and upper CT of each PT–CT heat structure is connected to the 4th node of moderator tank central row of pipes (317, 320, 323, 326, 329, 332, & 335).

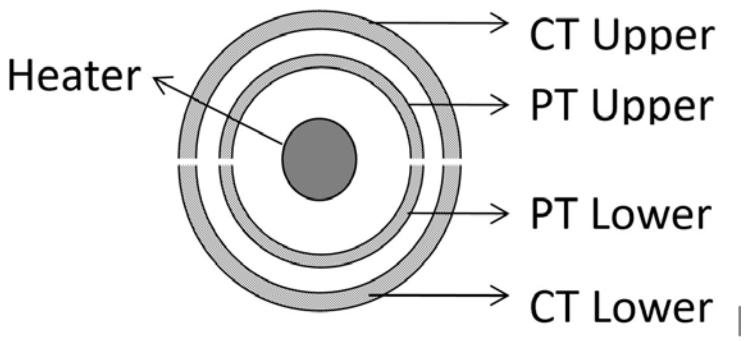

FIG. 12. PT–CT heat structure nodalization with CO_2 gap.

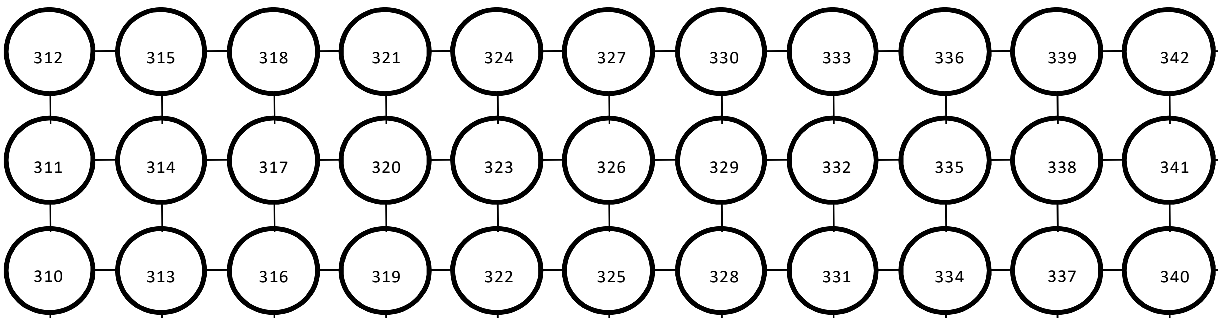

(a)

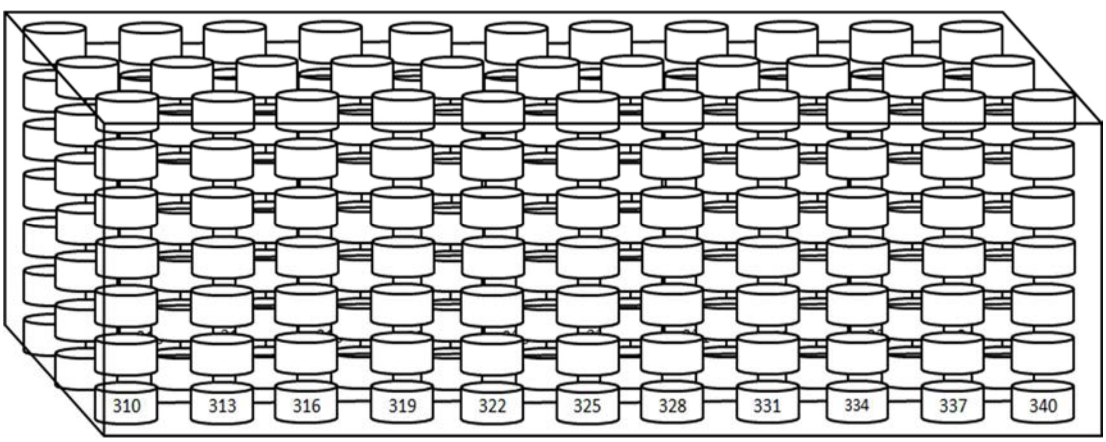

(b)

FIG. 13. (a) top view and (b) front view of moderator tank nodalization.

4.4.2.1. Changes from blind to open calculations

The nodalization of the PT–CT heat structure is modified by dividing it into lower and upper half. This enables the simulation of uniform or non-uniform heating of the bottom and top of the PT–CT, temperature variation in the top and bottom portion of PT and CT, PT–CT contact time variation. The heat transfer from the top and bottom PT–CT heat structure is modelled into different vertical tank volumes. This simulates the buoyancy driven natural circulation, variation in fluid temperature and void generation.

4.4.3. AERB COMSOL Model

After review of available contact gap models in the open literature, the Yovanovich et al. model [15], shown in Fig. 14(a) was selected, with the variation of gap conductance as a function of contact pressure between PT and CT with a CO2 filled gap from M. Shoukri and A. M. C. Chan [21], shown in Fig. 14(b). In COMSOL, the solid to solid conduction was modelled using the Yovanovich et al. equations below, and the gas conduction was given as a function of contact pressure using the values from Fig. 14 (b).

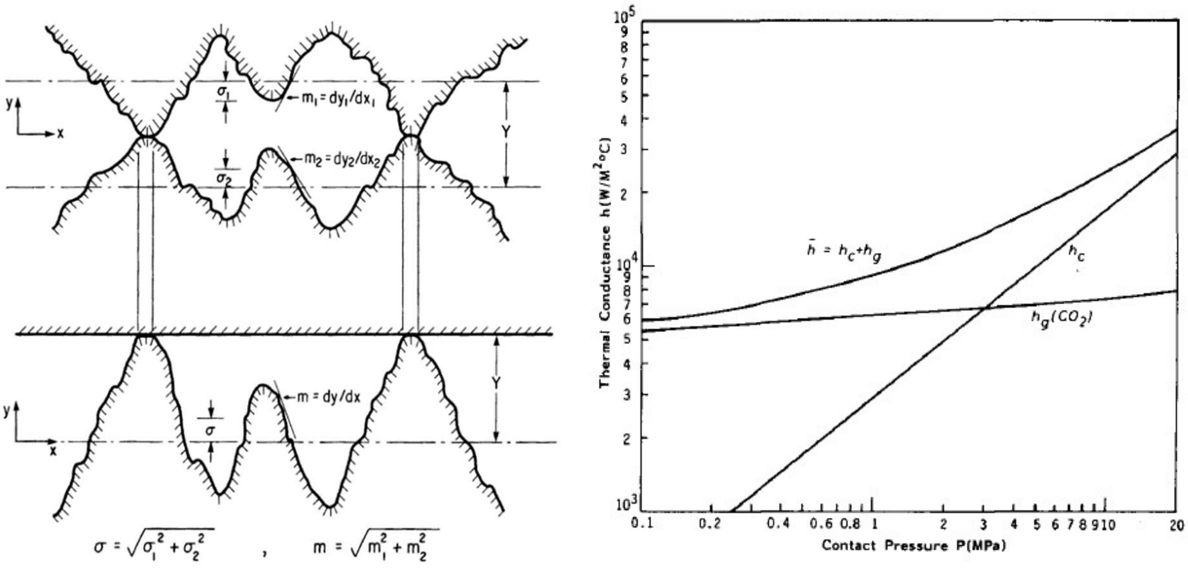

(a) (b)

FIG. 14. Models for contact conductance across CO_2 gap, (a) Schematic for Yovanovich model [15] (b) variation of gap conductance with contact pressure [21].

The solid to solid and gas conductances are thus:

$$h_c = 1.25\,\frac{k_s m}{\sigma}\left(\frac{P}{H}\right)^{0.95} \tag{6}$$

$$h_g = \frac{k_g}{(Y + \alpha_a \beta \wedge)} \tag{7}$$

$$Y = 1.184\,\sigma\left[-\ln\left(\frac{3.312P}{H}\right)\right]^{0.547} \tag{8}$$

where,

H = Material hardness of the softer material;
Y = Mean plane separation;
m = Average asperity slope;
σ = Average asperity height;
P = Contact pressure;
Λ = Mean free path;
α = Accommodation parameter;
β = Fluid parameter;
k_s, k_g = Thermal conductivity of solid material and gas.

The pool boiling heat transfer coefficient at the CT outer boundary is shown in Fig. 15.

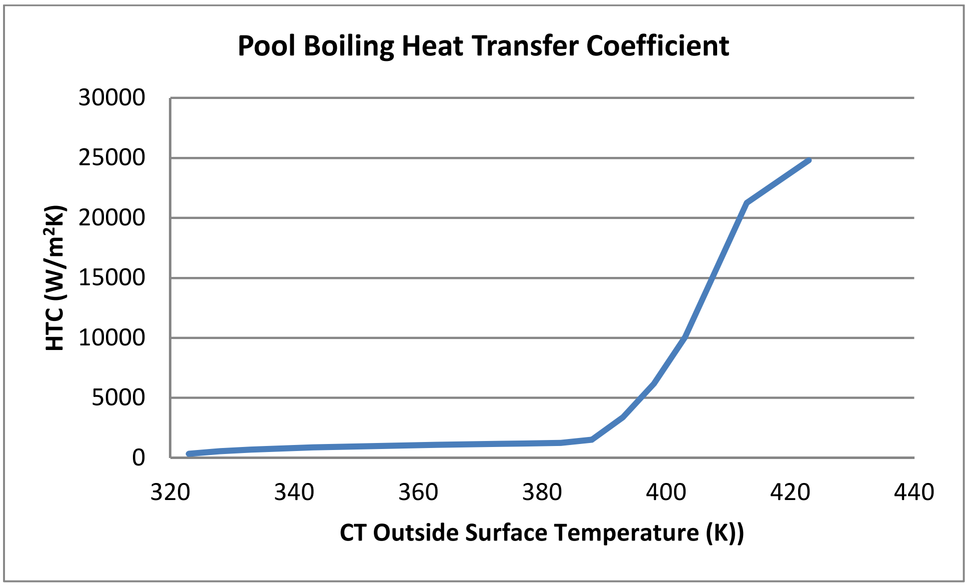

FIG. 15. Heat transfer coefficient at CT outer boundary.

4.4.4. BARC Model

The two explicitly coupled computational modules HEATCATS and PTCREEP were used to simulate the simultaneous creep deformation and the heat transfer phenomena in a 2D planar geometry at the middle of the test section (axial conduction and heat losses were ignored). Gas convection in the PT/CT gap and inside the pressure tube was also neglected. The moderator temperature was evaluated through a simple lumped parameter model

The PT deformation is assumed to be concentric and circular with the creep strain of each circumferential segment evaluated based on radially averaged PT temperature. The segments do not influence the deformation of their neighbouring segments. Creep deformation of CT was not considered; however, it is free to expand or contract due to its temperature.

Discretization of the test section is shown in Fig. 16. All the three components namely heater element, pressure tube and calandria tube are circumferentially discretized into 24 uniform meshes and radially discretized into 4, 5 and 3 nodes respectively.

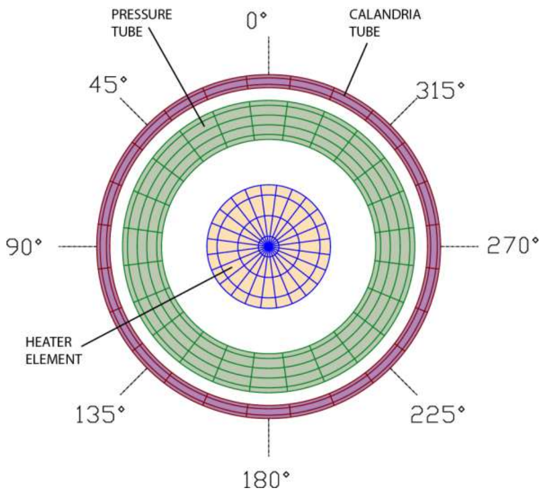

FIG. 16. Channel discretization.

HEATCATS solves the 2D energy equation through explicit finite difference formulation in cylindrical coordinates for the heater, the PT and the CT. Figure 17 indicates the mesh and nodal positions used in the formulation. In the radial direction, a component can be meshed non-uniformly whereas in the circumferential direction only uniform meshes are allowed.

Heat exchange on the internal face of the PT is calculated as:

$$q'_{\mathrm{ipt}} = q'_{\mathrm{radn}} + q'_{\mathrm{g,cond}} \tag{9}$$

where, q'_{radn} represents the radiative heat exchange between the heater element and the PT and $q'_{\mathrm{g,cond}}$ is the heat transfer through gas conduction. It is assumed that the heater is located concentrically at the centre of the PT.

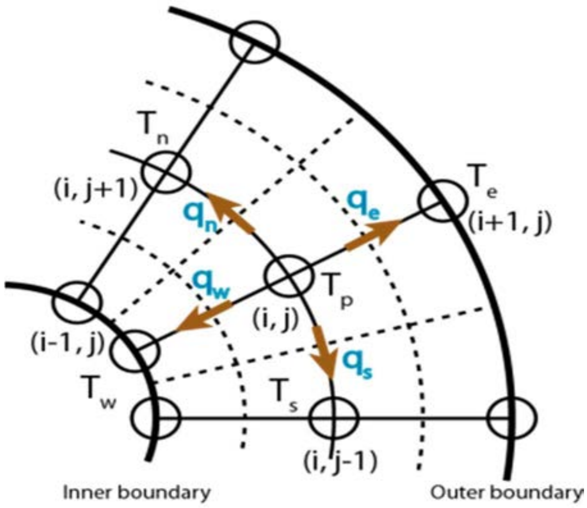

FIG. 17. Meshing of the components.

The heat transfer between PT and CT is calculated as:

$$q'_{\mathrm{ptct}} = (1 - f)q'_{\mathrm{gap}} + f q'_{\mathrm{cnt}} \tag{10}$$

where, f is the fraction of PT surface in contact with CT and:

$$q'_{\text{gap}} = q'_{\text{radn}} + q'_{\text{g,cond}} \tag{11}$$

$$q'_{\text{gap}} = \frac{\sigma A_{\text{pt}}\left(T_{\text{pt}}^4 - T_{\text{ct}}^4\right)}{\frac{1}{\varepsilon_{\text{pt}}} + \frac{A_{\text{pt}}}{A_{\text{ct}}}\left(\frac{1}{\varepsilon_{\text{ct}}} - 1\right)} + \frac{\left(T_{\text{pt}} - T_{\text{ct}}\right)}{\left(r_{\text{opt}} \ln\frac{A_{\text{ct}}}{A_{\text{pt}}}\right)} \tag{12}$$

The PT–CT contact heat transfer, q'_{cnt}, is calculated as:

$$q'_{\text{cnt}} = h_{\text{cnt}} A_{\text{cnt}}\left(T_{\text{opt}} - T_{\text{ict}}\right) \tag{13}$$

where, h_{cnt} is the contact conductance, A_{cnt} is the PT–CT contact area (equivalent to inner surface area of CT under full ballooning contact), T_{opt} and T_{ict} are the outer and inner surface temperature of PT and CT respectively. The contact conductance simulation is shown in Fig. 18.

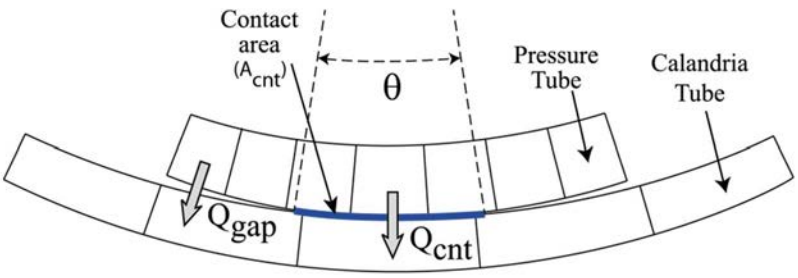

FIG. 18. PT/CT contact simulation.

The heat exchange between CT surface and the moderator is given by:

$$q'_{\text{modr}} = h_{\text{conv}} A_{\text{oct}}(T_{\text{oct}} - T_{\text{modr}}) \tag{14}$$

where, h_{conv} is the convection coefficient, T_{oct} is the outer surface temperature of calandria tube and T_{modr} is the moderator temperature. Convection coefficient is evaluated based on the pool boiling regimes dictated by calandria tube surface temperature. Boiling regimes and correlations used in the modelling are detailed in Table 3. Moderator temperature, T_{modr} is evaluated based on lumped parameter model.

The contact conductance model implemented in the code is based on the formulation proposed by Yovanovich [15] and the concept of contact zone discussed below.

Contact conductance, h_{cnt}, consists of two components, h_{c}, due to solid–solid contact and h_{gas} due to gas conduction in the gas gaps:

$$h_{\text{cnt}} = h_{\text{c}} + h_{\text{gas}} \tag{15}$$

$$h_{\text{gas}} = \left(\frac{k_{\text{g}}}{\sigma}\right) I_{\text{g}} \tag{16}$$

where, k_g is the gas thermal conductivity at mean gas temperature, σ is mean surface roughness, and the integral, I_{g} in its simplified form proposed by Yovanovich [15] as below:

$$I_{\mathrm{g}} = f_{\mathrm{g}}\left(\frac{Y}{\sigma} + \frac{M}{\sigma}\right) \tag{17}$$

where f_{g} is the correction factor:

$$f_{\mathrm{g}} = 1.063 + 0.047\left(4 - \frac{Y}{\sigma}\right)^{1.68}\left[\ln\left(\frac{\sigma}{M}\right)\right]^{0.84}$$
$$\text{for } 2 \le \frac{Y}{\sigma} \le 4 \text{ and } 0.01 \le \frac{M}{\sigma} \le 1 \tag{18}$$

$$f_{\mathrm{g}} = 1 + 0.06\left(\frac{\sigma}{M}\right)^{0.8}$$
$$\text{for } 2 \le \frac{Y}{\sigma} \le 4 \text{ and } 1 \le \frac{M}{\sigma} \le \infty \tag{19}$$

Y/σ is the relative mean plane separation between the contacting solids and is given by:

$$\frac{Y}{\sigma} = 1.184\left[-\ln\left(3.132\frac{P_{\mathrm{c}}}{H_{\mathrm{e}}}\right)\right]^{0.547} \tag{20}$$

where P_{c} is the contact pressure and H_{e} is the effective micro hardness calculated from correlation developed by Hegazy [22] for the Zr-2.5 wt% Nb surfaces. Furthermore,

$$\sigma = \sqrt{\sigma_{pt}^2 + \sigma_{ct}^2} \tag{21}$$

is the mean roughness, expressed as the root-mean-square of the PT and CT roughness, and M is the gas rarefaction parameter:

$$M = \left(\frac{2-\alpha_{\mathrm{pt}}}{\alpha_{\mathrm{pt}}} + \frac{2-\alpha_{\mathrm{ct}}}{\alpha_{\mathrm{ct}}}\right)\left(\frac{2\gamma}{1+\gamma}\right)\frac{1}{Pr}\Lambda \tag{22}$$

where α_{pt}, α_{ct}, γ, Pr, Λ are thermal accommodation coefficients corresponding to the gas–solid combination of surfaces 1 and 2, ration of specific heats, gas Prandtl number and molecular mean path [23].

The solid–solid contact conductance, h_{c}, is evaluated from below correlation:

$$h_{\mathrm{c}} = \frac{1.25 m K_{\mathrm{s}}}{\sigma}\left(\frac{P_{\mathrm{c}}}{H_{\mathrm{e}}}\right)^{0.95} \tag{23}$$

where K_{s} is the harmonic mean thermal conductivity, given by:

$$K_{\mathrm{s}} = \frac{2K_{\mathrm{pt}}K_{\mathrm{ct}}}{(K_{\mathrm{pt}}+K_{\mathrm{ct}})} \tag{24}$$

and m is the effective mean absolute surface slope, given by:

$$m = \sqrt{m_{\mathrm{pt}}^2 + m_{\mathrm{ct}}^2} \tag{25}$$

In the current formulation, the contact pressure (P_{c}) between PT/CT is not being calculated but rather obtained through a scheme of interpolation in the contact zone. Contact zone is nothing but a distance/thickness between PT and CT within which the pressure would vary from 0.1 MPa to the system pressure (e.g 3.5 MPa for the current test condition). The thickness is iteratively calculated assuming that at the contact zone the heat transfer Eq. (12) between

PT/CT is equivalent to the heat rate being calculated using Eq. (15). Within this contact zone, pressure is assumed to vary linearly with the PT radius.

The pressure tube ballooning or creep model, PTCREEP, is based on the transverse strain rate equations developed by Shewfelt et al. [7]. The PT is discretized into 1D circumferential segments equivalent to those in HEATCATS. Each circumferential segment is treated separately in calculating the strain based on radially averaged temperature. The transverse creep strain of each segment is obtained as below:

$$\varepsilon_{\mathrm{bl},i}^{k+1} = \dot{\varepsilon}_{\mathrm{bl},i}^{k+1}\Delta t \, + \, \varepsilon_{\mathrm{bl},i}^{k} \tag{26}$$

where $\varepsilon_{\mathrm{bl},i}^{k+1}$ is the creep strain at new time interval '$k+1$' and 'i' is the segment index.

The total circumferential strain of PT is calculated as:

$$\varepsilon = \sum_{i=1}^{n} \varepsilon_{\mathrm{bl},i} + \sum_{i=1}^{n} \varepsilon_{\mathrm{th},i} \tag{27}$$

where, $\varepsilon_{\mathrm{bl}}$ is the strain due to ballooning creep, $\varepsilon_{\mathrm{th}}$ is the strain due to thermal expansion and 'n' is total number of circumferential segments.

TABLE 3. CORRELATIONS USED IN BLIND AND OPEN CALCULATIONS

	PARAMETERS	BLIND	OPEN(A)	OPEN(B)
1.	Single phase	Churchill [18]		
2.	Nucleate boiling	Rohsenow [22]	Modified Chen correlation	
3.	Critical heat flux	Yagov [25]	Zuber-Griffith with modification accounting moderator subcooling (Thibault)	
4.	Transition Boiling	Interpolation between q''_{chf} and q''_{mfb} [26]		
5.	Minimum film boiling temperature	Mori [27]	$T_{mfb} = 2.38\Delta T_{sub} + 446.3 \; for \; \Delta T_{sub} < 30$ $T_{mfb} = 5.86\Delta T_{sub} + 341.9 \; for \; \Delta T_{sub} \geq 30$	
6.	Film boiling	Sakurai [28],[29]	Gillespie-Moyer correlation [26]	
7.	PT-CT contact modelling	A constant contact conductance of 11 kW/m^2 was used. PT-CT contact may loosen due to thermal contraction of PT and CT.	PT-CT heat transfer was governed by the imposed contact conductance shown in Fig. 15.	Contact conductance model detailed in this Section was used PT-CT contact may loosen due to thermal contraction of PT.
8.	Material Properties	a) For PT, Zircaloy-2 specific heat was used b) CT emissivity: 0.3	a) For PT, Zircaloy-2.5%wt Nb specific heat was used b) CT emissivity: 0.325	
9	Volumetric heat generation in graphite pin	$1.338 \times 10^8 \frac{W}{m^3}$ (max.) (heater length of 0.975 m was used)	$1.45 \times 10^8 \frac{W}{m^3}$ (max.) (voltage tapping distance of 0.9 m was used)	

4.4.5. CNSC Model

The CNSC model, as implemented in MATLAB, has been described in [30] and is for completeness also briefly described here, in addition to the novel implementation of the randomized contact conductance model, developed for this ICSP.

A typical nodalization diagram is presented in Fig. 19. A mesh and time step convergence analysis has been performed and several meshes, and time steps were tested. In the current context, 'typical nodalization' denotes an average mesh, with an optimized resolution and computation requirements. As such, the mesh presented in Fig. 19 has the following components and component structure:

— Heater (yellow): 5 radial and 30 circumferential nodes.
— Pressure tube (red): 40 axial, 3 radial and 36 circumferential nodes.
— Calandria tube (green): 40 axial, 2 radial and 36 circumferential nodes.

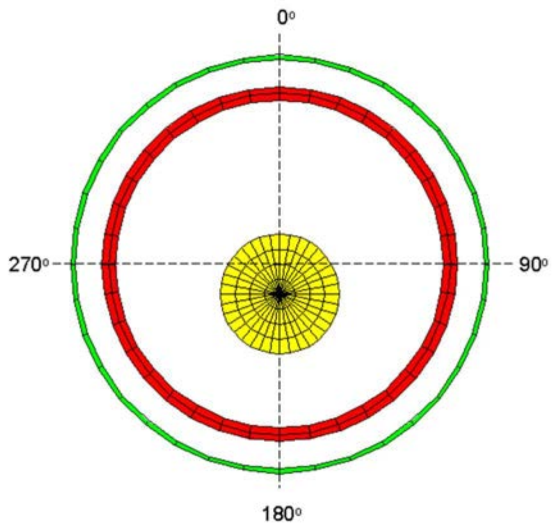

FIG. 19. Cross-sectional view of heater (yellow), pressure tube (red) and calandria tube (green) nodalization [30].

The following are the main phenomena that need to be simulated in the mathematical model of PT/CT heat transfer and deformation:

— Heat generation and conduction in the heater;
— Radiation and convection heat transfer to the pressure tube;
— Pressure tube heat up;
— Pressure tube deformation;
— Pressure tube to calandria tube heat transfer;
— Calandria tube to moderator heat transfer;
— Calandria tube heat up;
— Calandria tube deformation.

The main assumptions in the model presented herein are as follows:

— Axial symmetry: one half of test assembly length is modelled; the other half is constructed by 'mirroring' of results;
— Uniform pressure tube thickness at the beginning of the simulation;
— Uniform calandria tube thickness at the beginning of the simulation;
— Heater geometry and dimensions uniform and constant;

— Uniform Joule heat generation in heater;
— Uniform axial distribution of convective heat transfer coefficients;
— 3D unsteady temperature distribution in pressure tube and calandria tube;
— 2D (radial and circumferential) unsteady temperature distribution in heater;
— Pressure tube/calandria tube contact conductance initially variable, then uniform and constant, 2.5 $kWm^{-2}K^{-1}$;
— Heater emissivity: 0.9, uniform and constant;
— Pressure tube emissivity: 0.8, uniform and constant;
— Calandria tube emissivity: 0.3, uniform and constant;
— Creep considered only in radial direction, axial creep neglected;
— During creep deformation, pressure tube and calandria tube maintain circular geometry;
— During creep deformation, total volume of metal is constant.

4.4.5.1.Heat conduction

The general differential equation that describes the heat conduction with internal heat generation in cylindrical coordinates [5] is:

$$\frac{1}{r}\frac{\partial}{\partial r}\left(r\kappa\frac{\partial T}{\partial r}\right)+\frac{1}{r^2}\frac{\partial}{\partial \phi}\left(\kappa\frac{\partial T}{\partial \phi}\right)+\frac{\partial}{\partial z}\left(\kappa\frac{\partial T}{\partial z}\right)+q_\mathrm{v}=\rho c_\mathrm{p}\frac{\partial T}{\partial t} \tag{28}$$

Equation (28) was adapted in the heater for 2D conduction (i.e. radial and circumferential) with internal heat generation:

$$\frac{1}{r}\frac{\partial}{\partial r}\left(r\kappa\frac{\partial T}{\partial r}\right)+\frac{1}{r^2}\frac{\partial}{\partial \phi}\left(\kappa\frac{\partial T}{\partial \phi}\right)++q_\mathrm{v}=\rho c_\mathrm{p}\frac{\partial T}{\partial t} \tag{29}$$

And in the pressure tube and calandria tube for 3D conduction (i.e. radial, circumferential and axial), without internal heat generation:

$$\frac{1}{r}\frac{\partial}{\partial r}\left(r\kappa\frac{\partial T}{\partial r}\right)+\frac{1}{r^2}\frac{\partial}{\partial \phi}\left(\kappa\frac{\partial T}{\partial \phi}\right)+\frac{\partial}{\partial z}\left(\kappa\frac{\partial T}{\partial z}\right)=\rho c_\mathrm{p}\frac{\partial T}{\partial t} \tag{30}$$

In Eqs (28)–(30) T is the temperature, κ, ρ and c_p are thermal conductivity, density and heat capacity of the material. In order to obtain a numerical solution, each equation was discretized using forward difference in time and central difference in space (FTCS) method (see Fig. 20). The resulting finite difference scheme is explicit, first order in time and second order in spatial variables.

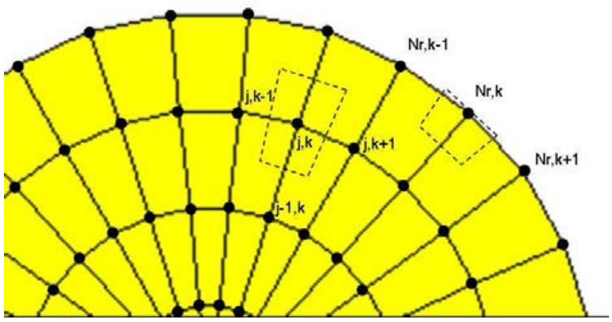

FIG. 20. Example of discretization of a cylindrical domain; boundaries of an internal node and an external node are presented [30].

The general discretized form of Eq. (28), applicable for internal nodes is:

$$\frac{T_{i,j,k}^{n+1}-T_{i,j,k}^{n}}{\Delta t}=\frac{1}{\rho c_{\mathrm{p}}}\left[\kappa_{i-\frac{1}{2},j,k}\frac{T_{i-1,j,k}^{n}-T_{i,j,k}^{n}}{(\Delta z)^2}-\kappa_{i+\frac{1}{2},j,k}\frac{T_{i,j,k}^{n}-T_{i+1,j,k}^{n}}{(\Delta z)^2}\right]+ \\ \frac{1}{\rho c_{\mathrm{p}}}\left[\kappa_{i,j-\frac{1}{2},k}\frac{T_{i,j-1,k}^{n}-T_{i,j,k}^{n}}{(\Delta r)^2}\frac{r_{j-\frac{1}{2}}}{r_j}-\kappa_{i,j+\frac{1}{2},k}\frac{T_{i,j,k}^{n}-T_{i,j+1,k}^{n}}{(\Delta r)^2}\frac{r_{j+\frac{1}{2}}}{r_j}\right]+ \\ \frac{1}{\rho c_{\mathrm{p}}}\left[\kappa_{i,j,k-\frac{1}{2}}\frac{T_{i,j,k-1}^{n}-T_{i,j,k}^{n}}{(r_j\Delta\theta)^2}-\kappa_{i,j,k+\frac{1}{2}}\frac{T_{i,j,k}^{n}-T_{i,j,k+1}^{n}}{(r_j\Delta\theta)^2}\right]+\frac{q_{\mathrm{v}}}{\rho c_{\mathrm{p}}} \tag{31}$$

where κ is the thermal conductivity, i, j and k are the node axial, radial and circumferential indices, n is the timestep index ρ and c_{p} are respectively the density and heat capacity of material. The solution of Eq (31) returns the temperature at the next timestep $(n+1)$ as function of known temperatures at the current timestep (n).

For nodes located at the boundary (e.g. at the heater surface or pressure tube surface), the discretized equation was derived based on the first principle, which balances heat transmitted by conduction from the neighbouring cells, internal heat generated (q_{v}) and heat removed by convection and radiation at the boundary (q'').

For a node located at an inside boundary that receives a net incident heat flux q'', the general discretized equation is:

$$\frac{T_{i,j,k}^{n+1}-T_{i,j,k}^{n}}{\Delta t}=\frac{1}{\rho c_{\mathrm{p}}}\left[\kappa_{i-\frac{1}{2},j,k}\frac{T_{i-1,j,k}^{n}-T_{i,j,k}^{n}}{(\Delta z)^2}-\kappa_{i+\frac{1}{2},j,k}\frac{T_{i,j,k}^{n}-T_{i+1,j,k}^{n}}{(\Delta z)^2}\right]+ \\ \frac{1}{\rho c_{\mathrm{p}}}\left[\frac{2q''R_{\mathrm{I}}}{\left(R_{\mathrm{I}}+\frac{\Delta r}{4}\right)\Delta r}-2\kappa_{i,j+\frac{1}{2},k}\frac{T_{i,j,k}^{n}-T_{i,j+1,k}^{n}}{(\Delta r)^2}\frac{R_{\mathrm{I}}+\frac{\Delta r}{2}}{R_{\mathrm{I}}+\frac{\Delta r}{4}}\right]+ \\ \frac{1}{\rho c_{\mathrm{p}}}\left[\kappa_{i,j,k-\frac{1}{2}}\frac{T_{i,j,k-1}^{n}-T_{i,j,k}^{n}}{R_{\mathrm{I}}\left(R_{\mathrm{I}}+\frac{\Delta r}{4}\right)(\Delta\theta)^2}-\kappa_{i,j,k+\frac{1}{2}}\frac{T_{i,j,k}^{n}-T_{i,j,k+1}^{n}}{R_{\mathrm{I}}\left(R_{\mathrm{I}}+\frac{\Delta r}{4}\right)(\Delta\theta)^2}\right]+\frac{q_{\mathrm{v}}}{\rho c_{\mathrm{p}}} \tag{32}$$

Similarly, for an outside boundary node, which emits net heat flux q'', the discretized heat conduction equation is:

$$\frac{T_{i,j,k}^{n+1}-T_{i,j,k}^{n}}{\Delta t}=\frac{1}{\rho c_{\mathrm{p}}}\left[\kappa_{i-\frac{1}{2},j,k}\frac{T_{i-1,j,k}^{n}-T_{i,j,k}^{n}}{(\Delta z)^2}-\kappa_{i+\frac{1}{2},j,k}\frac{T_{i,j,k}^{n}-T_{i+1,j,k}^{n}}{(\Delta z)^2}\right]+ \\ \frac{1}{\rho c_{\mathrm{p}}}\left[2\kappa_{i,j-\frac{1}{2},k}\frac{T_{i,j-1,k}^{n}-T_{i,j,k}^{n}}{(\Delta r)^2}\frac{R_0-\frac{\Delta r}{2}}{R_0-\frac{\Delta r}{4}}-\frac{2q''R_0}{\left(R_0+\frac{\Delta r}{4}\right)\Delta r}\right]+ \\ \frac{1}{\rho c_{\mathrm{p}}}\left[\kappa_{i,j,k-\frac{1}{2}}\frac{T_{i,j,k-1}^{n}-T_{i,j,k}^{n}}{R_0\left(R_0+\frac{\Delta r}{4}\right)(\Delta\theta)^2}-\kappa_{i,j,k+\frac{1}{2}}\frac{T_{i,j,k}^{n}-T_{i,j,k+1}^{n}}{R_0\left(R_0+\frac{\Delta r}{4}\right)(\Delta\theta)^2}\right]+\frac{q_{\mathrm{v}}}{\rho c_{\mathrm{p}}} \tag{33}$$

In Eqs (32) and (33), R_{I} and R_0 represent the inner and outer radii of the cylinder, respectively. Application of Eqs (31)–(33) to heater, pressure tube, or calandria tube is done with some simplifications, analogous to Eqs (28) and (29), namely no axial conduction for the heater and no internal heat generation for PT and CT.

It is worth noting that the application of Eq. (32) for the central node of the heater may lead to singularities, since $R_{\mathrm{I}}=0$. To address this aspect, the central node of the heater was modelled as a cylinder with uniform temperature and internal heat generation and the radius $r/2$.

4.4.5.2.Contact conductance

Contact conductance between pressure tube and calandria tube is one of the key parameters of simulation, since it directly controls post-contact heat transfer rate between the pressure tube and calandria tube, and ultimately impacts the boiling regime at the outside of calandria tube. It seems that the most reliable estimations of this parameter originate from PT/CT ballooning tests. A relevant study regarding the PT/CT contact conductance as well as associated phenomena (PT/CT deformation, heat transfer) is presented in [31]. One important observation is that PT/CT contact conductance is not constant during PT/CT contact transients. More specifically, it is maximum at the time of contact and subsequently decreases to a steady value, typically much smaller than the initial contact conductance. It was also observed that the maximum and steady values of contact conductance are function of PT internal pressure and, to lesser extent, the roughness of surfaces. The value recommended by [9] is 11 $kWm^{-2}K^{-1}$, but [31] uses a value of 7.8 $kWm^{-2}K^{-1}$at PT internal pressures of 3.5 MPa. Reference [12] recommends initial contact conductance 20 $kWm^{-2}K^{-1}$ for pressures greater than 3 MPa.

Experimental observations indicate that the higher initial contact conductance, the shorter its duration [31], [12]. The above-mentioned behaviour can be explained by the high interfacial pressure at the initial contact, whilst in the post-contact phase, the pressure tube contraction and calandria tube expansion cause the conductance to decrease. Higher initial conductance allows faster expansion/contractions, hence shorter duration of peak conductance. Another observation is that initial contact conductance seems to vary considerably from one geometrical location to another [12]; therefore, it is judged that one single value for a simulation may not be representative. The above observations are included in a conductance model, as follows:

(1) An average value of contact conductance was calculated, involving a few runs with different average values, and comparison of dryout maps with a reference experiment. For 3.5 MPa, 12.6 $kWm^{-2}K^{-1}$ was selected.
(2) A range of variation of maximum conductance was selected. For the current simulations, a range of ±50% the average value was adopted. That is, the initial contact conductivity ranges from a minimum of 6 to maximum of 19 $kWm^{-2}K^{-1}$. This range of variation is consistent with observations from previous contact boiling tests.
(3) Each finite surface pair pressure tube–calandria tube is randomly allocated a contact conductance selected from the conductivity range defined previously. An example of peak conductance map is presented in Fig. 21.
(4) Duration of maximum contact conductance was calculated from an empirically derived constant (i.e. the area defined by the contact conductance vs time in the transitory regime, 12 $kWm^{-2}K^{-1}s$) that was divided by the peak local conductance. For example, if a finite surface has a peak contact conductance of 11 $kWm^{-2}K^{-1}$, the duration of its application is 1.09 s. Transition from maximum conductance to steady state conductance (2.5 $kWm^{-2}K^{-1}$) is assumed over 0.5 s. The steady state conductance was maintained for the rest of the simulation.

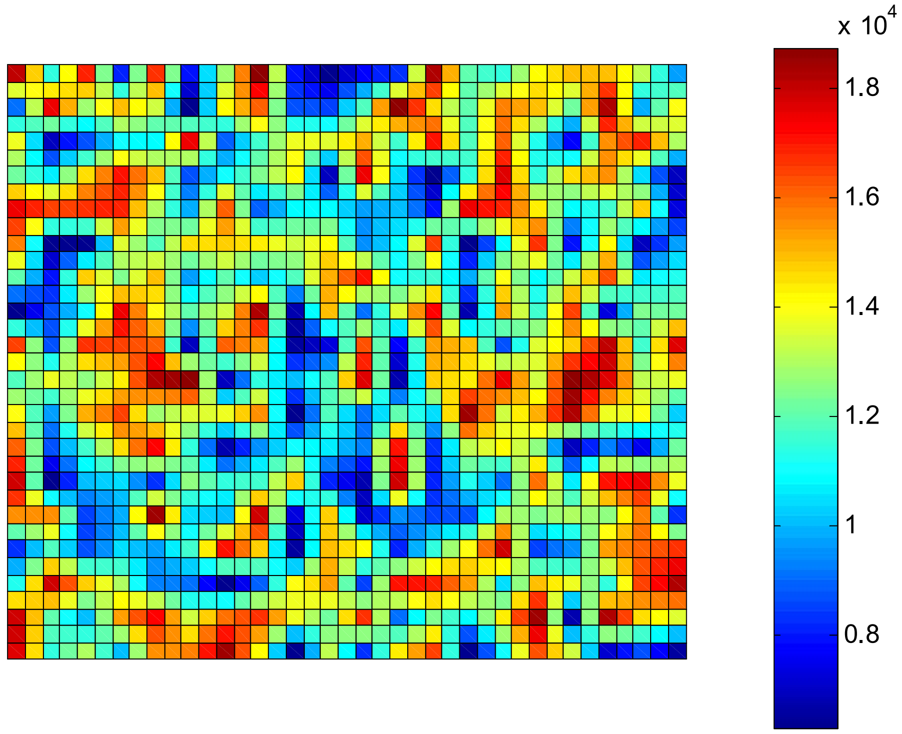

FIG. 21. Example of initial (peak) contact conductance map with average conductance of 12.6 $kWm^{-2}K^{-1}$ and range from 6 to 19 $kWm^{-2}K^{-1}$.

4.4.5.3.Free convection and radiation

Table 4 summarizes equations and correlations selected to model free convection and radiation heat transfer between heater and pressure tube, pressure tube and calandria tube and outside of calandria tube.

TABLE 4. CORRELATIONS FOR CONVECTION AND RADIATION HEAT TRANSFER [30]

LOCATION	PHENOMENON	EQUATION	OBSERVATIONS
Graphite heater–pressure tube	Free convection	Lis [32]: $\frac{k_{\text{eff}}}{k} = 0.389\left[Ra_{Di}\left(1-\frac{D_i}{D_0}\right)\right]^{0.237}$ $\frac{k_{\text{eff}}}{k} = 0.087\left[Ra_{Di}\left(1-\frac{D_i}{D_0}\right)\right]^{0.329}$	$4\cdot 10^4 < Ra_{Di}\left(1-\frac{D_i}{D_0}\right)^{6.5} < 1\cdot 10^8$ $1\cdot 10^8 < Ra_{Di}\left(1-\frac{D_i}{D_0}\right)^{6.5} < 1\cdot 10^{10}$
	Thermal radiation	$q_{\text{rad}} = \frac{\sigma(T_1^4 - T_2^4)}{\frac{1-\varepsilon_1}{A_1\varepsilon_1} + \frac{1}{A_1F_{12}} + \frac{1-\varepsilon_2}{A_2\varepsilon_2}}$	(1) Initial (un-deformed) geometry: This view factor matrix was applied from the start of the simulation until central axial ring of the pressure tube crept by 1%.
		$F_{i\to j} = \frac{1}{A_i}\int_{A_i}\int_{A_j}\frac{\cos\theta_i\cos\theta_j}{\pi r^2}dA_i dA_j$	(2) Intermediate deformation: The pressure tube radius is calculated as the average of initial value and the value at the contact with the calandria tube. This matrix was selected when deformation of central axial ring exceeded 1% until pressure tube/calandria tube contact occurred.
		$F_{i\to j} = \frac{1}{A_i}\sum_i\sum_j\frac{\cos\theta_i\cos\theta_j}{\pi r_{i\to j}^2}\Delta A_i\,\Delta A_j$	(3) Post deformation: Final view factor matrix assumed the pressure tube radius at the contact with calandria tube, and which was maintained until the end of the simulation. It should be noted that if after the contact pressure tube/calandria tube undergoes significant deformation (which was not the case for the current simulation) the view factor matrix requires subsequent updates.
Outer surface pressure tube–inner surface calandria tube (annulus)	Free convection	$q = \frac{2\pi L_{\text{h}} k_{\text{eff}}(T_i - T_0)}{\ln\left(\frac{r_0}{r_i}\right)}$	k_{eff} was assumed equal to molecular thermal conductivity of annulus gas, CO_2
	Thermal radiation	$q_{\text{rad}} = \frac{\sigma(T_1^4 - T_2^4)}{\frac{1-\varepsilon_1}{A_1\varepsilon_1} + \frac{1}{A_1F_{12}} + \frac{1-\varepsilon_2}{A_2\varepsilon_2}}$	The analysis assumes that F_{12} is unity, that is, all thermal radiation that leaves an elementary surface of PT is intercepted by the homologous surface of the CT

TABLE 4. CORRELATIONS FOR CONVECTION AND RADIATION HEAT TRANSFER (cont.) [30]

LOCATION	PHENOMENON	EQUATION	OBSERVATIONS
Outer surface calandria tube	Single phase free convection	Churchill and Chu [18] $$Nu_{\mathrm{D}} = \left\{ 0.6 + \frac{0.387 Ra_{\mathrm{D}}^{\frac{1}{6}}}{\left[1 + \left(\frac{0.559}{Pr}\right)^{\frac{9}{16}}\right]^{\frac{8}{27}}} \right\}^2$$	
	Nucleate boiling	Forster and Zuber [33]: $$q'' = 0.00122 \left(\frac{k_{\mathrm{f}}^{0.79} c_{\mathrm{pf}}^{0.45} \rho_f^{0.49}}{\sigma^{0.5} \mu_{\mathrm{f}}^{0.29} h_{\mathrm{fg}}^{0.24} \rho_{\mathrm{g}}^{0.24}} \right) [T_{\mathrm{w}} - T_{\mathrm{sat}}(P_{\mathrm{f}})]^{1.24} \Delta P_{\mathrm{sat}}^{0.75}$$	
	Critical heat flux	Zuber correlation of Lienhard [34]: $$q_{\mathrm{CHFsat}} = 0.118 h_{\mathrm{fg}} \left[\sigma g \rho_{\mathrm{g}}^2 (\rho_{\mathrm{f}} - \rho_{\mathrm{g}})\right]^{0.25}$$ For subcooled CHF, Thibault [35]: $$q_{\mathrm{CHF}} = q_{\mathrm{CHFsat}}[1 + 0.0437(T_{\mathrm{sat}} - T_0)]$$	
	Transition boiling	Bjonard and Griffith [20]: $$q_{\mathrm{TB}} = \lambda q_{\mathrm{CHF}} + (1 - \lambda) q_{\mathrm{mfb}}$$ $$\lambda = \left[\frac{(T_{\mathrm{mfb}} - T_{\mathrm{W}})}{(T_{\mathrm{mfb}} - T_{\mathrm{CHF}})}\right]^2$$	
	Rewetting temperature	$T_{\mathrm{rew}} = 2.38 \Delta T_{\mathrm{sub}} + 446.3$ $T_{\mathrm{rew}} = 5.86 \Delta T_{\mathrm{sub}} + 341.9$	$T_{\mathrm{sub}} < 30$ K $T_{\mathrm{sub}} > 30$ K
	Film boiling	Gillespie-Moyer [26]: $$h_{\mathrm{fb}} = h_{\mathrm{fb0}}[1 + 0.031(T_{\mathrm{sat}} - T_{\mathrm{l}})]$$ $$h_{\mathrm{fb0}} = 200 \frac{\mathrm{W}}{\mathrm{m^2 K}}$$	

4.4.5.4.Pressure tube and calandria tube deformation

Pressure tube/calandria tube deformation was modelled by the methodology presented by Shewfelt [7] and given in Eqs (1) and (2).

During pre-contact the pressure tube is subject to internal argon pressure, thus only the pressure tube will deform. Hoop stress of pressure tube is:

$$\sigma_{\mathrm{PT}} = \frac{P_{\mathrm{Ar}} r_{\mathrm{PT}}}{\tau_{\mathrm{PT}}} \tag{34}$$

After full circumferential contact with calandria tube, both pressure tube and calandria tube will interact and an interfacial pressure will develop. Interfacial pressure tends to suppress further deformation of pressure tube while simultaneously increasing the hoop stress of calandria tube. Deformation of post contact PT–CT was modelled by application of methodology presented in [31]. It assumes that after initial contact, PT and CT creep strain rates are equal, that is $\dot{\varepsilon}_{\mathrm{PT}} = \dot{\varepsilon}_{\mathrm{CT}}$. Alternative conditions included equality (within a small allowance) between outside radius of the pressure tube and inside radius of calandria tube at each time step.

Post contact hoop stresses are calculated as:

$$\sigma_{\mathrm{PT}} = \frac{(P_{\mathrm{Ar}} - P) r_{\mathrm{PT}}}{\tau_{\mathrm{PT}}} \tag{35}$$

$$\sigma_{\mathrm{CT}} = \frac{P \cdot r_{\mathrm{CT}}}{\tau_{\mathrm{CT}}} \tag{36}$$

where P_{Ar} denotes internal pressure tube argon gauge pressure, P is the PT/CT interfacial pressure, r_{PT} and r_{CT} are the average radius of pressure tube and calandria tube respectively, and τ_{PT} and τ_{CT} thickness of pressure tube and calandria tube, respectively.

4.4.5.5.Changes from blind to open calculations

The following three changes have been made to produce better agreement with experiment.

(a) Changing the CHF correlation

The Thibault correlation is replaced by Lienhard correlation [34] for higher CHF to reduce duration of dryout.

Thibault Correlation (as seen in Table 4):

$$q_{\mathrm{CHF}} = q_{\mathrm{CHFsat}}[1 + 0.0437(T_{\mathrm{sat}} - T_0)] \tag{37}$$

Lienhard Correlation:

$$q_{\mathrm{CHF}} = q_{\mathrm{CHFsat}}\left[1 + 0.1 c_{\mathrm{p}} \frac{(T_{\mathrm{sat}} - T_0)}{h_{\mathrm{fg}}}\right]\left(\frac{\rho_{\mathrm{f}}}{\rho_{\mathrm{g}}}\right)^{0.75} \tag{38}$$

(b) Changing the contact conductance model

The PT/CT contact conductance model was modified in accordance with values calculated from measurements. The constant value of this model two seconds after contact has been changed from 2.5 $kWK^{-1}m^{-2}$ used in the blind calculations to 1.0 $kWK^{-1}m^{-2}$ used in the open calculations. This has resulted in a higher post-contact temperature plateau for the open calculations, as compared to the blind calculation.

(c) Modifying the circumferential distributions of CHF and heat transfer coefficient (HTC) for the heater and PT

Table 5 shows CHF distributions (relative to the average value) used for blind and open calculations.

TABLE 5. CHF DISTRIBUTIONS

ANGLE FROM TOP	0 (top)	30	60	90	120	150	180
Local CHF Blind Calc.	0.87	1.03	1.03	1.03	1.02	1.11	0.93
Local CHF Open Calc.	0.93	0.98	0.99	1.0	1.0	1.1	1.1

The open calculations adopted larger CHF values at top and bottom with smaller values at sides. Larger CHF values lead to delayed occurrence of dry and shorter dryout periods.

Table 6 shows the distributions (relative to the average value) for the heater HTC used for blind and open calculations.

TABLE 6. HEATER HTC DISTRIBUTIONS

ANGLE FROM TOP	0 (top)	20	40	60	80	100	120	160	180
Local HTC Blind Calc.	0.12	0.17	0.29	0.52	0.94	1.32	1.48	1.74	1.09
Local HTC Open Calc.	0.1	0.15	0.22	0.52	0.94	1.32	1.48	1.7	2.1

The open calculations adopted smaller HTC values at top and larger values at bottom. This would lead to smaller heat flux at the top and larger heat flux at the bottom, as compared to the blind calculation.

Table 7 shows the distributions (relative to the average value) for the pressure tube HTC used for blind and open calculations.

TABLE 7. PRESSURE TUBE HTC DISTRIBUTIONS

ANGLE FROM TOP	0 (top)	20	40	60	80	100	120	160	180
Local HTC Blind Calc.	2.45	2.06	1.7	1.48	1.09	0.85	0.53	0.02	0.01
Local HTC Open Calc.	2.3	2.0	1.7	1.48	1.09	0.85	0.56	0.04	0.02

The open calculations adopted smaller HTC values at top and larger values at bottom. This would lead to smaller heat flux at the top and higher heat flux at the bottom, as compared to the blind calculation.

4.4.6. COG Model

The experimental geometry is simulated using 6 modules:

— Inflow unheated channel;
— Unheated length;
— Heated channel;
— Unheated length2;
— Outflow unheated channel;
— Moderator.

These modules are linked together and are divided into several hydraulic nodes, as presented in Fig. 22 (node numbers are listed in parentheses).

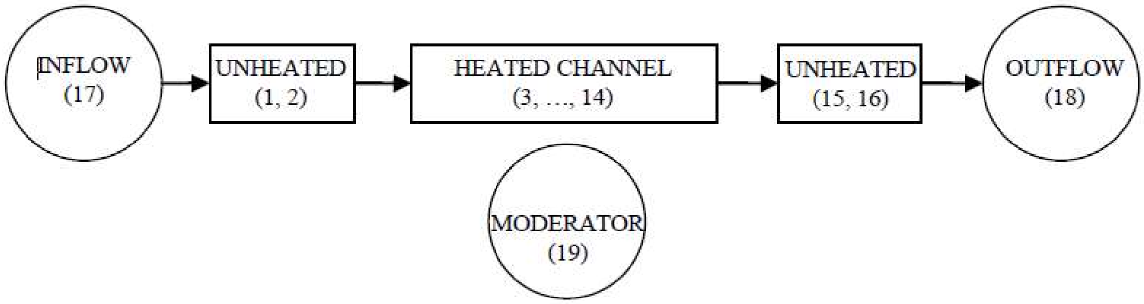

FIG. 22. Test section dimensions and TUF model nodalization

The 'INFLOW' and 'OUTFLOW' nodes in Fig. 22 are boundary condition nodes. The transient pressure measured during the test were applied as time functions for both nodes, noting that, because the measured pressure is differential, the atmospheric pressure measured at the beginning of the test was added to the transient pressure. The power measured during the test was assumed to be the heater power measured between the V-taps. For this reason, the heater power was computed by multiplying the measurements with a factor of 0.95/0.9 and all nodes in the channel (nodes 3 to 14) are assumed to have the same power fraction.

Since the time tables in TUF are limited in the number of data that can be stored, the PT pressure and heater power transients with a period of 0.1 seconds were shortened such that only the measurements that correspond to exact seconds (every 10^{th} measurement) were used in the TUF input.

The geometry parameters used as inputs to this model are:

— Heated length = 0.95 m;
— Pressure tube wall thickness = 4.4 × 10-3 m;
— Pressure tube inner wall radius = 51.900 × 10-3 m;
— Flow area = 7.3280 x 10-3 m2;
— Calandria tube inner radius = 64.700 × 10-3 m;
— Calandria tube thickness = 1.4000 × 10-3 m.

The initial heater power was set to 1 W. This low power should not affect the high temperature part of the results since the power transient is not related to the initial power. The initial temperature was set to the water temperature, 70.5 ºC, however, this parameter will be updated by the code during steady state simulation.

The transient power and pressure are represented in Fig. 23.

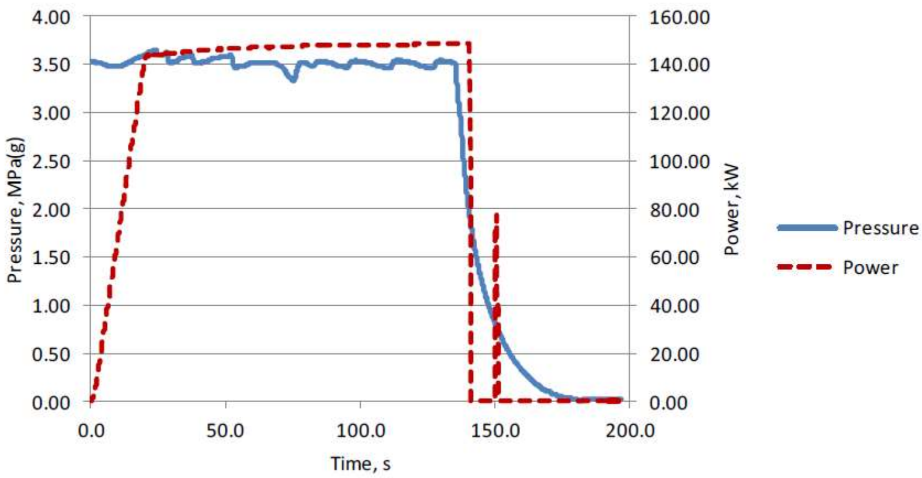

FIG. 23. Power and pressure measured during IAEA ICSP subcooling test from when the heater power is switched on (t=0) to the end of the test.

The following additional assumptions were necessary to implement the simulation in TUF:

— In TUF, the inner fluid is steam, whereas Argon is used in the test.
— The heater is simulated as a fuel element having the outer sheath diameter equal to the actual heater diameter. The material properties (conductivity, heat capacity, and density) for fuel and sheath are equal to the material properties of graphite. These properties have constant values, which are assumed to be representative for the temperatures experienced by the heater during the test.
— The maximum CT true strain at which the CT is considered failed, and at which the calculation will stop, is assumed to be 20%.

The parameters calculated in this analysis are:

— Average heater surface temperature;
— Average pressure tube mid-wall temperature;
— Average calandria tube mid-wall temperature;
— Average pressure tube circumferential strain;
— Total heat transfer from heater to PT (convective and radiative);
— Total heat transfer from PT to CT (conductive, convective, and radiative);
— Total heat transfer from CT to water;
— PT to CT contact heat transfer coefficient, axial centre;
— Heat transfer coefficient at CT outside surface, axial centre.

4.4.7. KAERI Model

The KAERI model, as implemented in COMSOL and described in [37] and [38], is for completeness also briefly described below.

The simplified schematic of the experimental setup is given in Fig. 24. Initial temperatures for all solid structures including the heater, PT, and CT walls are assumed to be 70 ˚C. The prescribed heater power conditions are given as input of the blind calculation.

In the blind calculation, initial time at 0.0 s is defined as the time when the ramp to full power started. The transient input data for heater power is simplified and plotted as a linear line. It is ramped from 0.0 kW to 150 kW of full power within 10.0 seconds. The full power is maintained until 140.0 s, and then the power is rapidly decreased to 0.0 kW.

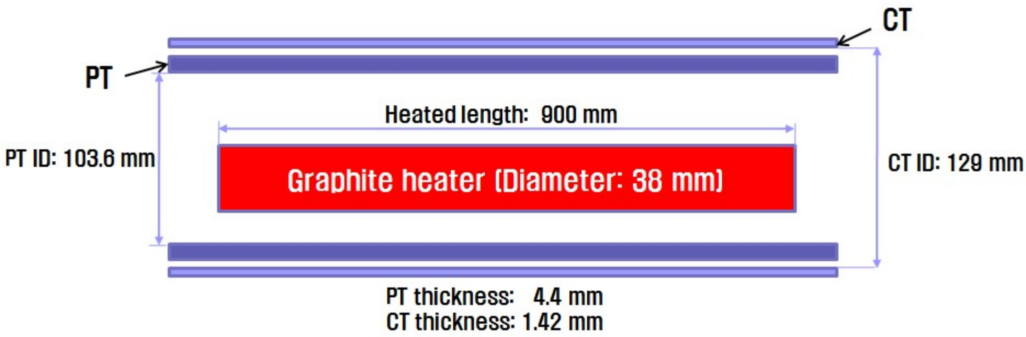

FIG. 24. Side view of the fuel channel model [37].

The multi-physical simulation is done with the thermal stress (ts) model in the structural mechanics module of a commercial code COMSOL Multyphysics™ ver. 4.3 [10]. The computational domain and boundary condition are given in Fig. 25.

The governing equations are listed as:

$$-\nabla \cdot \tilde{\sigma} = \vec{F}_{\mathrm{V}} \tag{39}$$

$$\tilde{\sigma} - \tilde{\sigma}_0 = \tilde{C} : [\tilde{\varepsilon} - \tilde{\varepsilon}_0 - \tilde{\alpha}(T - T_0)] \tag{40}$$

$$\frac{\partial \tilde{\varepsilon}}{\partial t} = \frac{1}{2}[(\nabla \vec{u})^T + \nabla \vec{u}] \tag{41}$$

$$\rho C_{\mathrm{p}} \left(\frac{\partial T}{\partial t} + \vec{u} \cdot \nabla T \right) = \nabla \cdot (k \nabla T) + Q_{\mathrm{V}} \tag{42}$$

Equation (39) is solved for components of the stress tensor, and the volumetric external force is given as boundary conditions. Note that the stress tensor, later reduced to the plane stress, should be three-dimensional though the computational domain in Fig. 25(a) is 2-D, which is due to the Poisson's ratio in the linear elastic stiffness matrix of Eq. (40). For isotropic materials, the stiffness is expressed as a symmetric square matrix with the six degrees of freedom [39]:

$$\tilde{C} = \frac{E}{(1+\nu)(1-2\nu)} \begin{bmatrix} 1-\nu & \nu & \nu & 0 & 0 & 0 \\ \nu & 1-\nu & \nu & 0 & 0 & 0 \\ \nu & \nu & 1-\nu & 0 & 0 & 0 \\ 0 & 0 & 0 & \frac{1-2\nu}{2} & 0 & 0 \\ 0 & 0 & 0 & 0 & \frac{1-2\nu}{2} & 0 \\ 0 & 0 & 0 & 0 & 0 & \frac{1-2\nu}{2} \end{bmatrix} \tag{43}$$

Structural and thermal strains are coupled in the right side of Eq. (40) where the source of temperature is fed back from Eq. (42), the energy equation. From the strain rate, the convective velocity as a function of the global inertia coordinate system is simply obtained from Eq. (41). During each time step, both Eqs (41) and (42) are integrated by time to calculate a new temperature field for the source term of Eq. (40). The volumetric heat source should be specified inside the field, and other conditions on the temperature and its gradient, or heat flux exerted at all boundaries.

If we assume a very small deformation of initial grids in the global coordinate, Eqs (39) through (42) are coupled to consist of a complete multi-physical system: structural dynamics and heat transfer.

The dominant heat transfer mechanism at the boundaries between the CO_2 gap and each tube is thermal radiation heat transfer, so the others such as convection and conduction will be neglected in this study: the gaseous gap can be deleted from the computational domain shown in Fig. 25(a). The boundary conditions are marked in Fig. 25(b) and Fig. 26 shows the computational grids for the present problem.

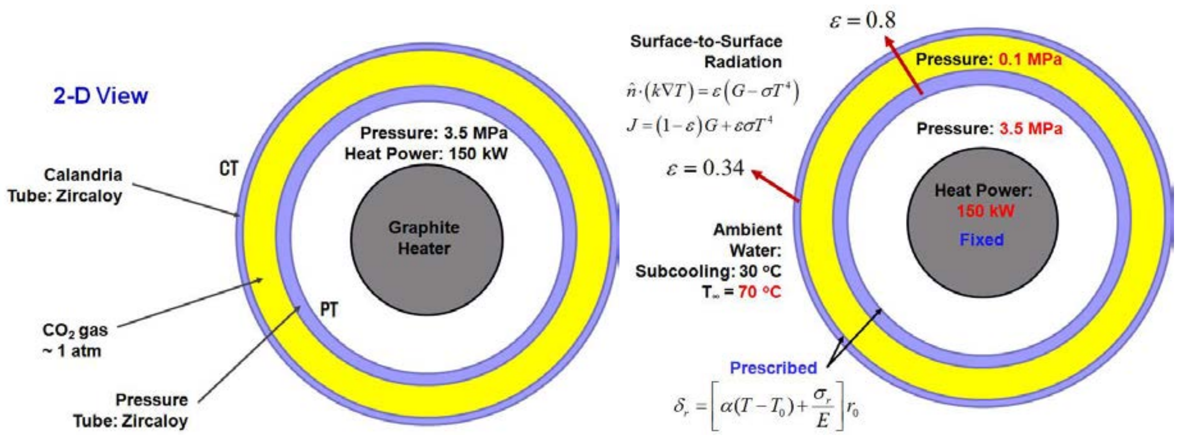

(a) *(b)*

FIG. 25. Computational model (a) computational domain (b) boundary condition [37].

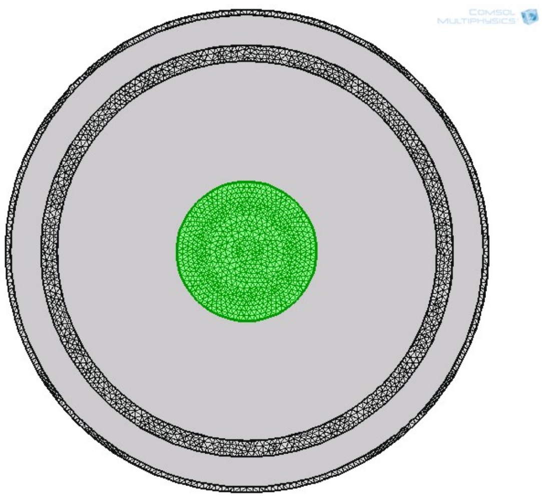

FIG. 26. Computational grids [37].

The boundary of core graphite heater is fixed while the inner boundaries of PT and CT should be prescribed as uniform in the radial direction from the thermal expansion and the structural elongation to avoid the numerical instability of asymmetric translation [40].

$$\delta_r = \left[\alpha(T - T_0) + \frac{\sigma_r}{E}\right] r_0 \tag{44}$$

where load conditions are specified with a constant pressure 3.5 MPa at the core surface and the inner PT, and 0.1 MPa at the outer PT and the inner CT. The emissivity of the core graphite heater, PT, and CT are 1, 0.8, and 0.34, respectively. At the outer boundary of CT, subcooled temperature condition is applied as a constant value of 70°C under standard atmospheric pressure.

Between the core graphite heater and PT as well as PT and CT, a radiation boundary condition is applied, which is summarized as:

$$\hat{n} \cdot (k\nabla T) = \varepsilon(G - \sigma T^4) \tag{45}$$

$$J = (1 - \varepsilon)G + \varepsilon\sigma T^4 \tag{46}$$

Equation (45) is solved for the local temperature in the boundaries to calculate J in Eq. (46), and the incident radiation G is an explicit function of the surface radiation J and the view factor F determined by the mutual geometric configuration of surface–surface radiation boundaries. Therefore, Eqs (45) and (46) are iterated for the balance of incoming and outgoing heat radiation through the boundary where the opacity is controlled with temperature distribution and emissivity ε that is a material property.

The implementation of radiation boundary condition should be validated from the comparison with an analytic solution in a classical textbook [41]. Figure 27 indicates a benchmark problem for the validation of radiation boundary condition. Between two surfaces 1 and 2, a vacuum domain exists, and $\varepsilon_1 = 0.8$, $\varepsilon_2 = 0.3$, $r_1 = 0.3$ m, $r_2 = 0.5$ m. The analytic solution for heat flux is the same as that of code prediction.

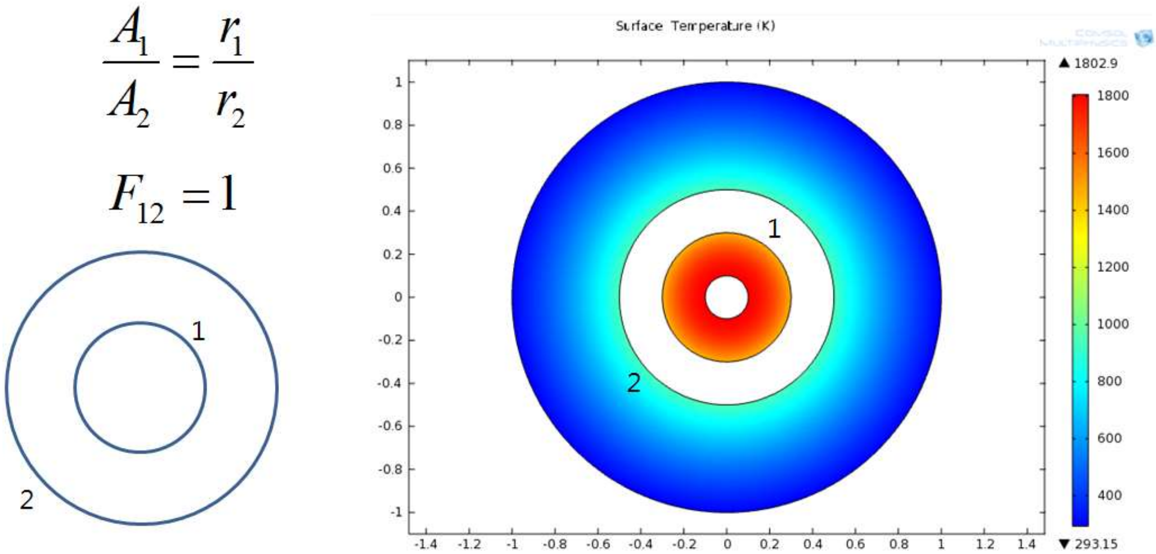

FIG. 27. Benchmark validation for the surface–surface radiation boundary condition [37].

$$Q_{12} = \frac{2\pi r_1 \beta\left(T_1^4 - T_2^4\right)}{\frac{1}{\varepsilon_1} + \frac{1-\varepsilon_2}{\varepsilon_2}\left(\frac{r_1}{r_2}\right)} \tag{47}$$

where the area ratio is $A_1/A_2 = r_1/r_2$, and view factor is $F_{12} = 1$. The numerical solution for the computational domain in Fig. 27 is $T_1 = 1456.6$ K and $T_2 = 946.5$ K, the mean temperature along each circumference for $Q_c = 150$ kW. $Q_{12} = 149.1$ kW is computed in Eq. (47). Therefore, the error is just within 0.6%.

4.4.7.1.Plastic deformation model for COMSOL code

Structural correlations are obtained from the fitting of experimental data [41] and [43]:

$$\rho\left[\frac{\mathrm{kg}}{\mathrm{m}^3}\right] = 6595 - 0.1477T\left[\frac{1}{\mathrm{K}}\right] \text{ for } T < 1083 \text{ K} \tag{48}$$

$$\rho\left[\frac{\mathrm{kg}}{\mathrm{m}^3}\right] = 1.62 \times 10^{11} - 8.79 \times 10^{7}T\left[\frac{1}{\mathrm{K}}\right] \text{ for } 1083 \text{ K} \le T \le 1800 \text{ K} \tag{49}$$

$$E[\mathrm{Pa}] = 1.24 \times 10^{11} - 6.22 \times 10^{7}T\left[\frac{1}{\mathrm{K}}\right] \text{ for } T \le 1090 \text{ K} \tag{50}$$

$$E[\mathrm{Pa}] = 1.52 \times 10^{11} - 8.79 \times 10^{7}T\left[\frac{1}{\mathrm{K}}\right] \text{ for } 1090 \text{ K} < T < 1255 \text{ K} \tag{51}$$

$$E[\mathrm{Pa}] = 9.21 \times 10^{10} - 4.05 \times 10^{7}T\left[\frac{1}{\mathrm{K}}\right] \text{ for } 1255 \le T \tag{52}$$

$$\nu = 0.4 \tag{53}$$

$$\varepsilon_{\mathrm{p}} = 4.95 \times 10^{-6}T\left[\frac{1}{\mathrm{K}}\right] - 1.49 \times 10^{-3} \text{ for } T < 1083 \text{ K} \tag{54}$$

$$\varepsilon_{\mathrm{a}} = 1.26 \times 10^{-5}T\left[\frac{1}{\mathrm{K}}\right] - 3.78 \times 10^{-3} \text{ for } T < 1083 \text{ K} \tag{55}$$

$$\varepsilon_{\mathrm{p}} = \varepsilon_{\mathrm{a}} = \left[2.77763 + 1.09802\cos\left(\frac{T\left[\frac{1}{\mathrm{K}}\right] - 1083}{161}\pi\right)\right] \times 10^{-3} \quad \text{for } 1083 \text{ K} \le T \le 1244 \text{ K} \tag{56}$$

$$\varepsilon_{\mathrm{p}} = 9.70 \times 10^{-6}T\left[\frac{1}{\mathrm{K}}\right] - 1.04 \times 10^{-2} \text{ for } 1244 \text{ K} < T \tag{57}$$

$$\varepsilon_{\mathrm{a}} = 9.76 \times 10^{-6}T\left[\frac{1}{\mathrm{K}}\right] - 4.40 \times 10^{-3} \text{ for } 1244 \text{ K} < T \tag{58}$$

where Eqs (54) through (58) are only valid for the linear elasticity model. The valid region of Eqs (54) and (55) is reduced to $T < 973$ K, and Eqs (56) through (58) are replaced to adopt the plastic deformation model described below.

The first simulation is for the linear elastic model, the result of which is shown in Fig. 28. The multi-physical system is converged to steady state in 160 s. Fig. 28(a) and (b) are von Mises stress and temperature field distribution in steady state, respectively. The temperature–time history is given in Fig. 28(c) at the surface of heater, PT, CT, and outer boundary.

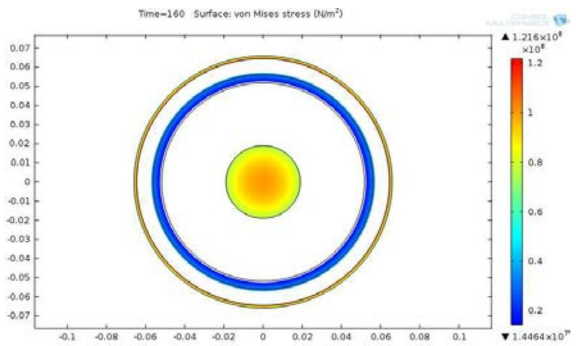

(a)

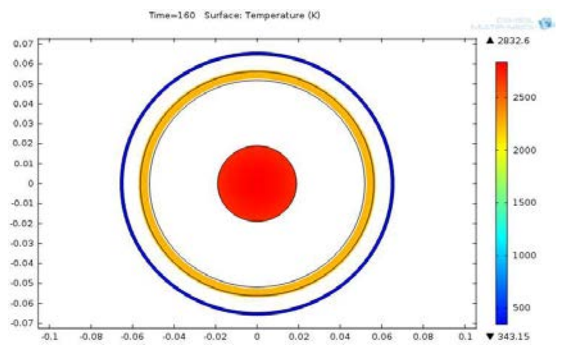

(b)

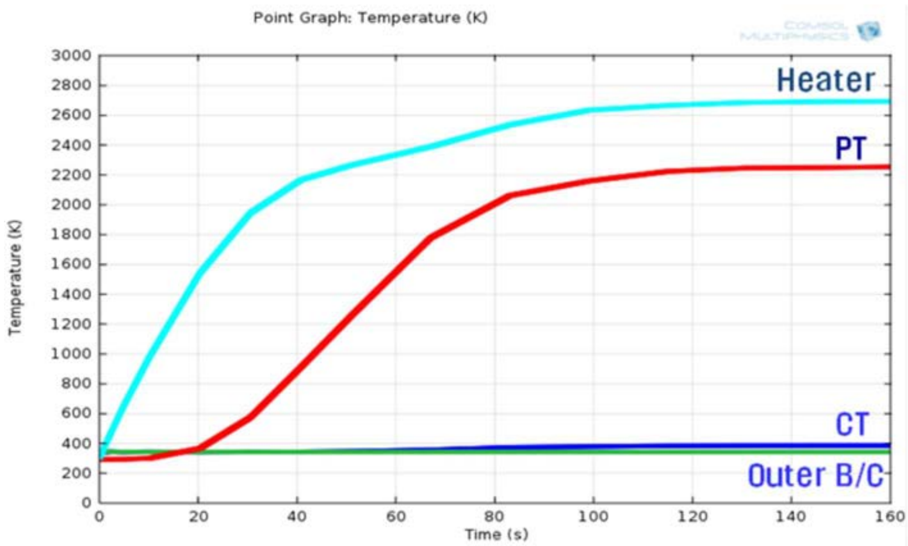

(c)

FIG. 28. Simulation result of the linear elastic model; (a) Von Mises stress, (b) temperature field, (c) temperature–time history at the surface boundaries [37].

The result of the present simulation seems to be very stable, and there is no evidence for the thermal expansion of PT. However, this is restricted from the linear elastic model in Eq. (12a-c), so a modified model is required for the consideration of plastic deformation.

The creep model [7] for the CATHENA code is also used in the present calculation, with the creep rate equations given by (1) and (2).

Unfortunately, the time integration at the denominator of Eqs (1) and (2) cannot be expressed in the analytic form, which needs some approximation. Using the two-point Gaussian quadrature for these integrations [44]:

$$\int_{t_1}^{t} e^{\frac{-A}{T}} dt = \int_{T_1}^{T} \frac{e^{\frac{-A}{T}}}{\frac{dT}{dt}} dt = \frac{1}{\dot{T}} \int_{T_1}^{T} e^{\frac{-A}{T}} dT$$
$$\approx \frac{T-T_1}{2\dot{T}} \left[\frac{-A}{e^{\frac{1}{2}\left\{\left(1+\frac{1}{\sqrt{3}}\right)T+\left(1-\frac{1}{\sqrt{3}}\right)T_1\right\}}} + \frac{-A}{e^{\frac{1}{2}\left\{\left(1-\frac{1}{\sqrt{3}}\right)T+\left(1+\frac{1}{\sqrt{3}}\right)T_1\right\}}} \right]$$
$$\approx \frac{T-T_1}{2\dot{T}} \left[\frac{-A}{e^{0.7887T+0.2113T_1}} + \frac{-A}{e^{0.2113T+0.7887T_1}} \right] \tag{59}$$

$$\int_{t_2}^{t} \mathrm{e}^{\frac{-B}{T}}(T-C)^n dt \approx \frac{T-T_2}{2\dot{T}}\left[\mathrm{e}^{\frac{-B}{0.7887T+0.2113T_2}}(0.7887T+0.2113T_2-C)^n+\mathrm{e}^{\frac{-B}{0.2113T\quad .7887T_2}}(0.2113+0.7887T_2-C)^n\right] \tag{60}$$

The time rate for the surface temperature of PT in Eqs (59) and (60) is measured in Fig. 28 (c):

$$\dot{T}=\frac{dT}{dt}\approx\frac{\Delta T}{\Delta t}=33.25\ \mathrm{K/s} \tag{61}$$

where this value seems a constant during the time 40 to 60 s. Therefore, if the thermal expansion of PT terminates in that time region, this assumption should be valid for the present simulation.

Substituting Eq. (61) into Eqs (59) and (60), and with the following numerical value:

$$\sigma=(3.4\ \mathrm{MPa})\frac{54\ \mathrm{mm}}{4.4\ \mathrm{mm}}=41.73\ \mathrm{MPa} \tag{62}$$

The strain rate in Eq. (14) is expressed in an explicit form:

$$\dot{\varepsilon}=(4.99\times10^{9})\mathrm{e}^{\frac{-36600}{T}}+\frac{(4.31\times10^{10})\mathrm{e}^{\frac{-29200}{T}}}{\left[1+(3.01\times10^{8})(T-973)\left(\mathrm{e}^{\frac{-2920}{0.7887T+206}}+\mathrm{e}^{\frac{29200}{0.2113T+76}}\right)\right]^{0.42}} \tag{63}$$

for $973\ \mathrm{K}\le T\le 1223\ \mathrm{K}$

$$\dot{\varepsilon}=(3.36\times10^{6})\mathrm{e}^{\frac{-19600}{T}}+\frac{(6.50\times10^{6})\mathrm{e}^{\frac{-1960}{T}}}{1+(4.12)(T-112\ )\left[\mathrm{e}^{\frac{-1960}{0.7887T+237}}(0.7887T-868)^{3.72}+\mathrm{e}^{\frac{-19600}{0.2113T+886}}(0.2113T-219)^{3.72}\right]} \tag{64}$$

for $1123\ \mathrm{K}\le T\le 1473\ \mathrm{K}$

From the definition of thermal expansion:

$$\varepsilon=\alpha\Delta T\ \therefore\ \alpha=\frac{d\varepsilon}{dt}\Big/\frac{dT}{dt}=\frac{\dot{\varepsilon}}{\dot{T}} \tag{65}$$

Equations (63) and (64) are expressed in the form of thermal expansion coefficient, simply divided by $\dot{T}$ in Eq. (65):

$$\alpha=(1.50\times10^{8})\mathrm{e}^{\frac{-36600}{T}}+\frac{(1.42\times10^{9})\mathrm{e}^{\frac{-29200}{T}}}{\left[1+(3.01\times10^{8})(T-973)\left(\mathrm{e}^{\frac{-29200}{0.7887T+206}}+\mathrm{e}^{\frac{29200}{0.2113T+76}}\right)\right]^{0.42}} \tag{66}$$

for $973\ \mathrm{K}\le T\le 1223\ \mathrm{K}$

$$\alpha=(1.01\times10^{5})\mathrm{e}^{\frac{-19600}{T}}+ \tag{67}$$

$$\frac{(1.95\times10^{5})e^{\frac{-19600}{T}}}{1+(4.12)(T-112\ )\left[e^{\frac{-1960}{0.7887T+237}}(0.7887T-86\ )^{3.72}+e^{\frac{-1960}{0.2113T+88}}(0.2113T-219)^{3.72}\right]}$$

$$\text{for } 1123\ \mathrm{K} \le T \le 1473\ \mathrm{K}$$

Equations (66) and (67) are finally applied to the simulation of plastic deformation of PT. The thermal expansion coefficient becomes a function of temperature (Fig. 29). When the PT is heated, over the temperature 973 K (699.85ºC), the expansion coefficient is abruptly increased to reach about 1.7×10^4 times that in the linear elastic region in the numerical value at 1400 K (1126.85ºC).

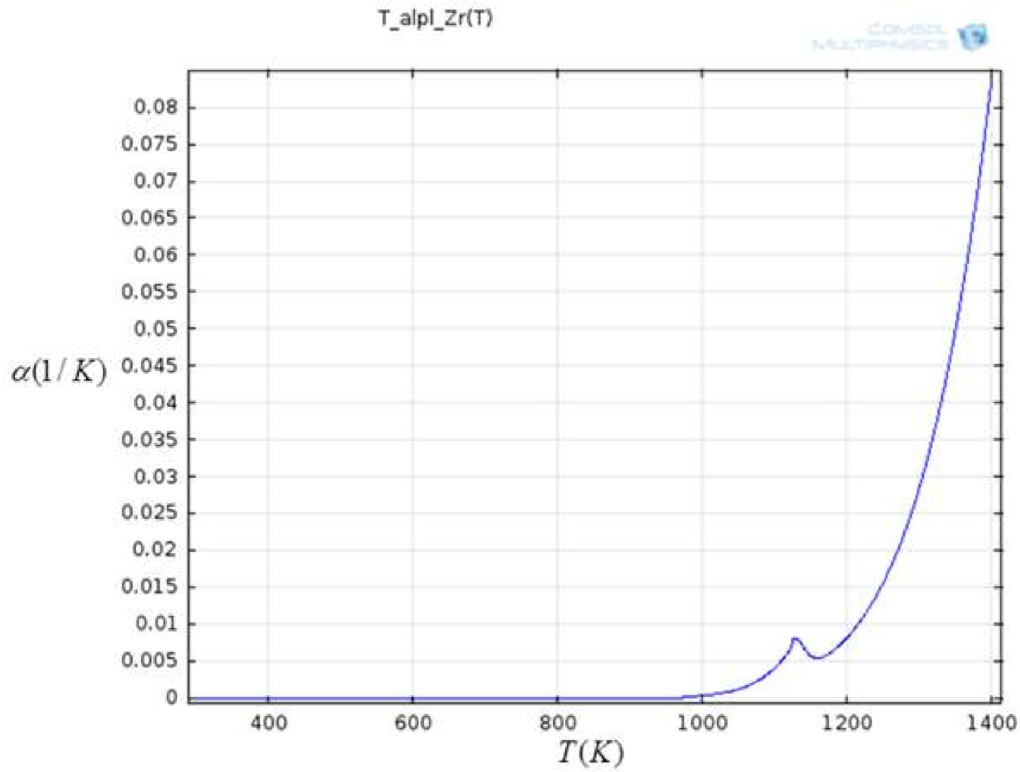

FIG. 29. Thermal expansion coefficient as a function of temperature for the plastic deformation model [37].

Therefore, in the nonlinear range, the term of thermal expansion in Eq. (40) should be corrected from the linear form:

$$\tilde{\alpha}(T - T_0) \rightarrow \int_{T_0}^{T} \tilde{\alpha} dT \tag{68}$$

and two-point Gaussian quadrature method is used for the numerical computation of the integration in Eq. (68).

4.4.8. KANUPP Model

To model the test apparatus, it has been idealized as a one-dimensional problem in conduction, convention and radiation heat transfer as shown in Fig. 30.

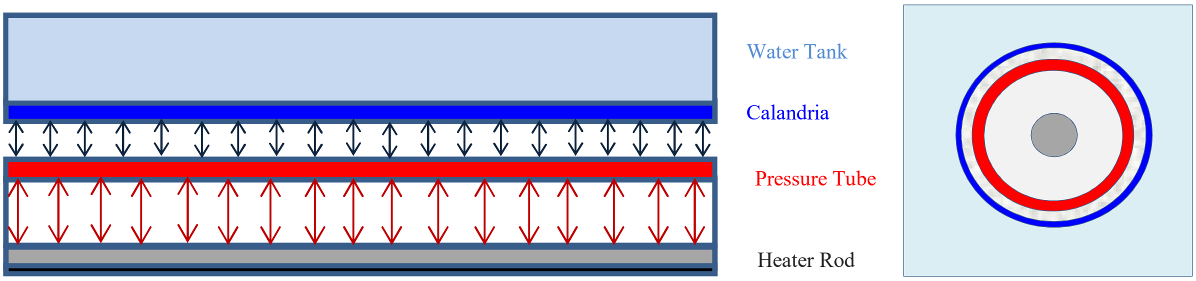

FIG. 30. Idealization of the test apparatus

The conduction heat transfer inside the three metals (GH, PT and CT) is separately represented by transient Fourier equation:

$$\rho c_p \frac{\partial T}{\partial t} = k\left(\frac{\partial^2 T}{\partial r^2} + \frac{1}{r}\frac{\partial T}{\partial r}\right) + q(r,t) \tag{69}$$

The last term (volumetric heat source) is a user defined function for GH, and is equal to zero when applied to PT or CT.

The temperature-dependent thermal conductivity and specific heat are used in the discretized equations with uniform heat source across the GH radius.

The above equation is discretized using implicit finite difference scheme as in the finite difference form:

$$\rho c_p \frac{T_i^{n+1} - T_i^n}{\Delta t} = k\left(\frac{T_{i-1} - 2T_i + T_{i+1}}{(\Delta r)^2} + \frac{1}{r_i}\frac{(T_{i+1} - T_{i-1})}{2\Delta r}\right) + q_i^n \tag{70}$$

Here, the time derivative $\partial u/\partial t$ is approximated by forward difference in time and the spatial derivatives are approximated by central difference formulae using weighted average (in time) value of u. That is:

$$T_i = (1-\phi)T_i^n + \phi T_i^{n+1} \tag{71}$$

Thus,

$$\begin{aligned} T_i^{n+1} - T_i^n &= \frac{k\Delta t}{\rho C_p (\Delta r)^2}(T_{i-1} - 2T_i + T_{i+1}) \\ &\quad + \frac{k\Delta t}{2\rho C_p r_i \Delta r}(T_{i+1} - T_{i-1}) + \frac{q_i^n \Delta t}{\rho C_p} \end{aligned} \tag{72}$$

using $T_i^{n+1} = (T_i - (1-\phi)T_i^n)/\phi$ $T_i^{n+1} = (T_i - (1-\phi)T_i^n)/\phi$ and simplifying:

$$\begin{aligned} -\left(1 - \frac{\Delta r}{2r_i}\right)T_{i-1} + \left(\frac{\rho C_p (\Delta r)^2}{k\Delta t \phi} + 2\right)T_i - \left(1 + \frac{\Delta r}{2r_i}\right)T_{i+1} \\ = \frac{\rho C_p (\Delta r)^2}{k\Delta t \phi} T_i^n + \frac{q_i^n (\Delta r)^2}{k} \end{aligned} \tag{73}$$

This equation is written at each mesh point and the appropriate boundary conditions (BC) are applied as follows:

Graphite heater (Left BC - Eq (74); Right BC -Eq (75)):

$$\left.\frac{\partial T}{\partial t}\right|_{r=0} = 0 \tag{74}$$

$$-k\left.\frac{\partial T}{\partial t}\right|_{r=r_{\mathrm{GHo}}} = Q_{\mathrm{rad,g-p}} + Q_{\mathrm{Ar}} \tag{75}$$

where:

$$Q_{\mathrm{rad,g-p}} = H_{\mathrm{rad,g-p}}(T_{\mathrm{GHo}} - T_{\mathrm{PTi}}) \tag{76}$$

$$H_{\mathrm{rad,g-p}} = \frac{\sigma(T_{\mathrm{GHo}}^2+T_{\mathrm{PTi}}^2)(T_{\mathrm{GHo}}+T_{\mathrm{PTi}})}{\frac{1}{\epsilon_{\mathrm{GH}}}+\frac{D_{\mathrm{GH}}}{D_{\mathrm{PTi}}}\left(\frac{1}{\epsilon_{\mathrm{PT}}}-1\right)} \tag{77}$$

$$Q_{\mathrm{Ar}} = \frac{k_{\mathrm{Ar}}}{D_{\mathrm{GH}}\cdot\ln\left(\frac{D_{\mathrm{PTi}}}{D_{\mathrm{GH}}}\right)} \tag{78}$$

Pressure tube (Left BC -Eq (79); Right BC -Eq (80) prior to contact and Eq (81) after contact):

$$-k\left.\frac{\partial T}{\partial t}\right|_{r=r_{\mathrm{PTi}}} = -Q_{\mathrm{rad,g-p}} + Q_{\mathrm{Ar}} \tag{79}$$

$$-k\left.\frac{\partial T}{\partial t}\right|_{r=r_{\mathrm{PTo}}} = Q_{\mathrm{rad,p-c}} + Q_{\mathrm{CO2}} \tag{80}$$

$$-k\left.\frac{\partial T}{\partial t}\right|_{r=r_{\mathrm{PTo}}} = Q_{\mathrm{C}} = h_{\mathrm{c}}(T_{\mathrm{PTo}} - T_{\mathrm{CTi}}) \tag{81}$$

where:

$$Q_{\mathrm{rad,p-c}} = H_{\mathrm{rad,p-c}}(T_{\mathrm{PTo}} - T_{\mathrm{CTi}}) \tag{82}$$

$$H_{\mathrm{rad,p-c}} = \frac{\sigma(T_{\mathrm{PTo}}^2+T_{\mathrm{CTi}}^2)(T_{\mathrm{PTo}}+T_{\mathrm{CTi}})}{\frac{1}{\epsilon_{\mathrm{PT}}}+\frac{D_{\mathrm{PTo}}}{D_{\mathrm{CTi}}}\left(\frac{1}{\epsilon_{\mathrm{CT}}}-1\right)} \tag{83}$$

Calandria tube (Left BC -Eq (84); Right BC -Eq (85)):

$$-k\left.\frac{\partial T}{\partial t}\right|_{r=r_{\mathrm{CTi}}} = -Q_{\mathrm{rad,p-c}}\ or\ Q_{\mathrm{C}} \tag{84}$$

$$-k\frac{\partial T}{\partial t}\bigg|_{r=r_{\text{CTo}}} = h_{\text{mod}}(T_{\text{CTo}} - T_{\text{mod}}) \tag{85}$$

The first and last equations for each of the three domains are modified according to the above boundary conditions. We, therefore, obtain three sets of simultaneous equations that can be solved by Gaussian Tridiagonal algorithm.

Moderator heat transfer:

Natural convective heat transfer is given by Churchil and Chu [18] correlation:

$$Nu_{\text{D}} = \left\{0.6 + \frac{0.387Ra_{\text{D}}^{1/6}}{\left[1+(0.559/Pr)^{9/16}\right]^{8/27}}\right\}^2 \tag{86}$$

where Ra and Pr and Raleigh and Prandtl numbers, respectively. The nucleate boiling heat transfer is calculated by Rohsenow [24] correlation, simplified at moderator conditions:

$$q = C(T_{\text{w}} - T_{\text{s}})^3 \tag{87}$$

The Critical Heat Flux (CHF) at temperature T for subcooled pool boiling is calculated using Thibault correlation [35]:

$$\frac{q_{\text{chfsub}}}{q_{\text{chfsat}}} = 1.006 + 0.0436(T_{\text{sat}} - T) \tag{88}$$

The saturated pool boiling CHF is calculated using Modified Zuber correlation [34]:

$$q_{\text{chfsat}} = 0.118h_{\text{fg}}\left(\sigma \text{g}\rho_{\text{g}}^2(\rho_{\text{f}} - \rho_{\text{g}})\right)^{0.25} \tag{89}$$

The Minimum Film Boiling Temperature as function of fluid subcooling is given by Lauer and Hufschmidt [36] correlation:

$$\Delta T_{\text{mfb}} = 5.893\Delta T_{\text{sub}} + 228.6 \tag{90}$$

The rounding of the boiling curve at the top was approximated by a constant heat flux equal to the critical heat flux for an interval of 10°C beginning at the temperature of the critical heat flux.

The heat flux in the transition boiling regime was assumed to decrease from critical heat flux to the minimum film boiling heat flux along two straight lines which intersected at a heat flux of:

$$q = \frac{q_{\text{CHF}} - q_{\text{MIN}}}{3} \tag{91}$$

and temperature of:

$$T = \frac{2}{3}(T_{\text{CHF}} - T_{\text{MIN}}) \tag{92}$$

The minimum heat flux is calculated by Luaer-Hufschmidt equations given above. The film boiling heat transfer is given by Gillespie and Moyer correlation [26]:

$$q_{\mathrm{fb}} = 0.2(1 + 0.031(T_{\mathrm{sat}} - T_{\mathrm{b}})) \tag{93}$$

Pressure tube deformation:

The plastic deformation of the pressure tube is calculated using the Shewfelt equations, Eq (1) and (2).

Heater power:

Heater loss considered in the calculations is 5% and incorporated by employing a power factor of 0.95 in the input cards. The heater power is assumed to be uniformly distributed over the five axial node points.

Contact conductance:

Due to unavailability of explicit data on contact conductance in the experiment, open literature and engineering judgment is used to prepare values of contact conductance. The data in Table 8 was used for PT/CT contact conductance.

TABLE 8. PT/CT CONTACT CONDUCTANCE

TIME AFTER CONTACT (s)	CONTACT CONDUCTANCE (kW/m^2°C)
0.0	11.0
10.0	11.0
15.0	5.0
Onward	5.0

4.4.9. SNN Model

Assumptions for blind calculations were as follows:

— The model included heat transfer only in radial direction. View factors are used to model radiation heat transfer. No heat losses were considered at the sides. Axial power distribution is uniform.
— The heater was modelled considering an offset of 9.5 mm to the bottom.
— The non-uniform free convection of argon gas was included in the model.
— Natural convective flow in the water tank was neglected.

The following dimensions and assumptions have been used in the simulation:

— The initial inner and outer radii of the pressure tube were 51.9 and 56.2 mm;
— The initial inner and outer radii of the calandria tube were 64.7 and 66.1 mm;
— The PT and CT were each modelled with a length of 0.90 m.

Only half of the geometry is considered assuming lateral symmetry to the vertical diametric line of the PT;

The PT and CT are assumed to have the same number of circumferential sectors/subsectors and axial segments. The test was represented by 20 axial nodes, 10 radial nodes and 16 circumferential sector groups.

The material of PT and CT was Zircaloy. The CATHENA built-in temperature-dependent thermal properties were used.

The schematic model piping network is presented in Fig. 31. The heater, annulus gas and moderator are represented in the axial direction. Heater rod was modelled through 20 axial nodes. The nodes length is imposed in order to cover the location of each thermocouple. The circular geometry was considered during the model development. The circumferential nodalization was represented by 16 sectors while 10 radial nodes have been used in the radial direction.

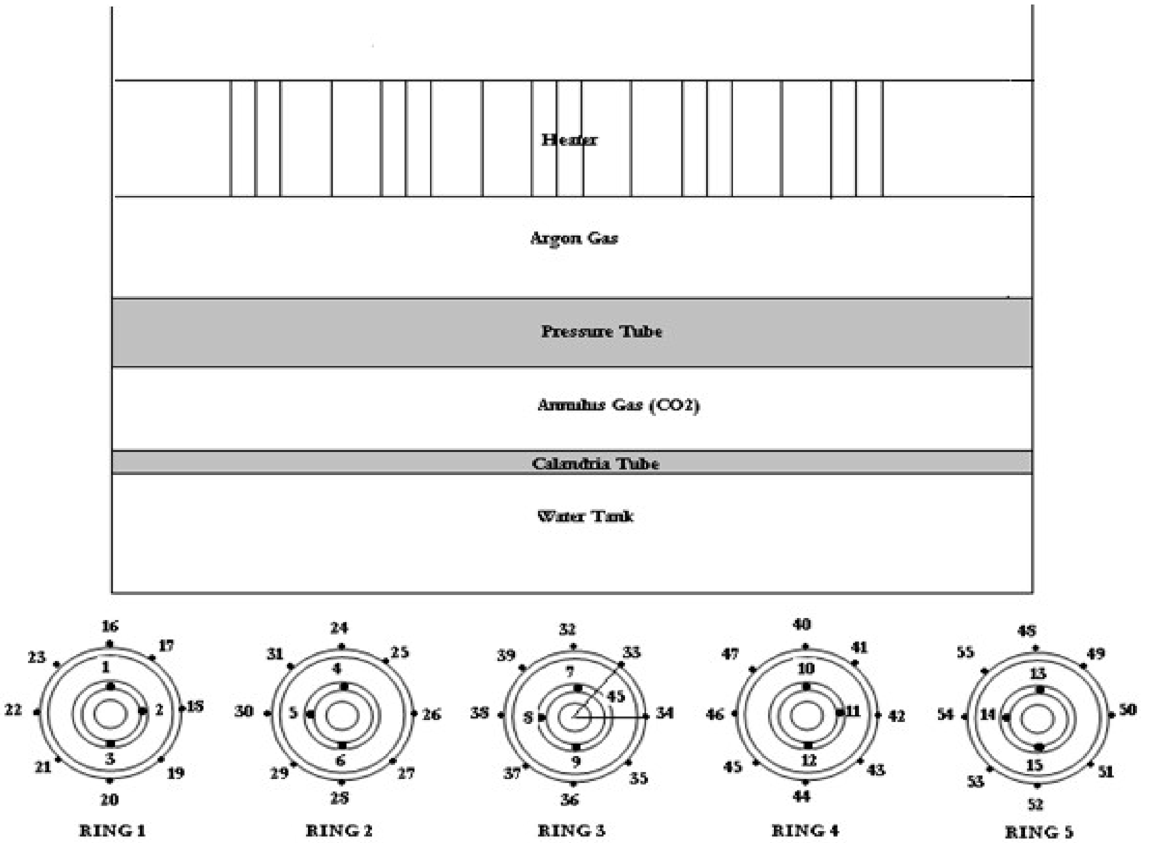

FIG. 31. Sketch showing model nodalization for the actual test simulation (blind simulation).

Figure 32(a) shows a set of heater element/PT and how temperature stations should be identified. For the model prepared, the temperature stations indices are numbered counter-clockwise, starting from the vertical (twelve o'clock) position from 1 to 32. Fig. 32(b) shows an assembly of PT/CT and how temperature stations may be identified, and temperature stations indices are numbered in counter clockwise from 1 to 32.

The GENHTP boundary conditions for the heater are represented by the outside conditions represented by the heater surface. For the PT, two boundary conditions were included. The inside boundary condition is represented by the heater while the outside boundary conditions are represented by the annulus gas. Similarly, for the CT the internal boundary conditions are represented by the PT, while the outside is represented by the moderator.

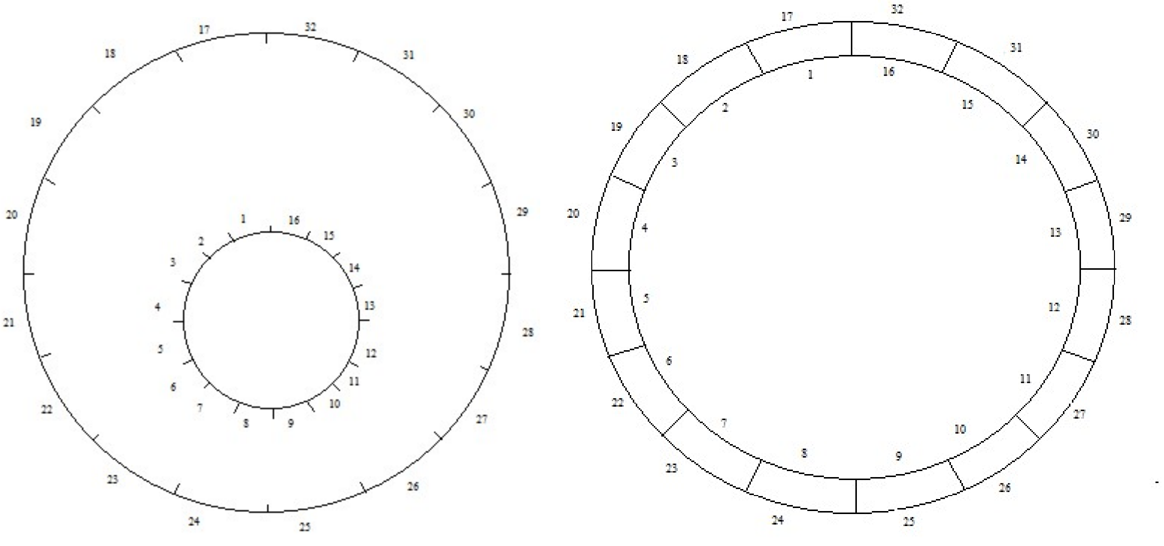

(a) *(b)*

FIG. 32. (a) Heater and pressure tube and (b) pressure tube and calandria tube view factor matrix numbering system (blind simulation).

4.4.9.1.Initial conditions

Initial conditions for PT and CT temperatures were imposed at each radial location as presented in the test description information received in the pre-test report presentation.

The presence of argon gas around the heater was modelled as a non-condensable gas in the channel around the graphite rod (mixed H_2O and Argon was considered as the circulation fluid). The pressure control was imposed at 3.5 MPa while the gas temperature was also kept constant at 300°C. These values have been included in the model as boundary and initial conditions.

Annulus gas (CO_2) is modelled as a pipe around the PT, having the length equal to that of the PT. The annulus pipe is connected by two reservoirs, one at each of its sides. The reservoirs are modelled as pressure boundary conditions. The annulus gas pressure is maintained constant during the test at atmospheric pressure. The temperature of the gas was assumed/considered at 70°C in the model. The corrected stagnant CO_2 flow of 0.0 kg/s was imposed in the model as flow boundary condition.

The water in the tank was assumed to be in contact with the atmosphere. The atmospheric temperature was imposed at 21.5°C while pressure was imposed to 746 mm Hg (as per pre-test reported conditions).

4.4.9.2.Special models used and user options

(a) Free convection model

Free convection occurs when there are density gradients accompanied by thermal stratification in a gas. In fuel channel integrity test a thermal gradient develops between the top and bottom of the PT. This thermal gradient promotes density gradients in the gas and thus a free convection flow is induced. The free convection currents provide an extra path to transfer heat from the electrically heater to PT.

As per pre-test data, the temperature at the top of the PT was higher than at the bottom. This difference in temperature can be attributed to free convection. The free convection provides an extra path to transfer heat from the electrically heater to the PT. The free convection effect increases with increasing temperature difference between heater and the PT and with increasing with internal pressure. The free convection effect was estimated by applying the correlation developed by Raithby and Hollands [44]. Therefore, free convection was incorporated in the model used for the blind calculations.

(b) Fuel channel deformation model

The fuel channel deformation model is used to calculate the deformation through ballooning of a PT caused by the high PT temperature and relatively high internal pressure. The model calculates the strain deformation of each PT model sector around PT circumference and, individually at each axial segment along its length. Straining of the PT is calculated until PT/CT contact occurs. Subsequently, the model calculates the solid–solid heat transfer rates between PT and the CT based on contact conductance.

The contact conductance transient following PT/CT ballooning contact was setup as follows: zero until the contact; a step increase to a high initial contact conductance following the contact; holding the constant initial contact conductance for a short time interval; a linear decrease to a constant post-contact conductance (the limiting values and the time interval were considered as per new moderator subcooling methodology).

For a deformed PT, the outer flow areas are much larger than the inner flow areas. If the heater is assumed to have offset within the PT, a significant portion of the outer flow area comes from the top region of the channel. The flow area and hydraulic diameter calculation is required for each thermalhydraulic node along the channel if the PT has strained differently at each axial location.

The model includes information regarding the number of surfaces that will come in contact and data about the number of sub sector subdivisions which are used in deformation calculation. PT/CT contact heat transfer is modelled as occurring over the entire circumference of the PT in a given axial location when strain to contact has been predicted. CT strain was calculated after PT/CT contact.

(c) Auxiliary model for heat transfer through radiation

Thermal radiation was modelled between the heater and PT and between PT and CT. Each of the solid elements in a given GENHTP model of CATHENA is subdivided into axial, radial, cylindrical and circumferential subcomponents. Since the thermal radiation heat transfer occurs only between surfaces only the innermost or outermost radial node is considered for this treatment.

A constant emissivity of 0.9 is applied for the heater. For both inside and outside surfaces of the PT a constant emissivity of 0.8 is used, while an emissivity of 0.325 for the inside surface of the CT. The file used to calculate the view factors between the heater and PT was prepared based on numbering scheme shown in Fig. 32 using the GEOFAC code. Similarly, the scheme used for PT and CT is presented in Fig. 32 (a) and (b) for PT and CT, respectively. Each of the PT and CT is split into 16 sectors. 'GEOFAC' stores the general view factors in a file and then does the compression of these factors to a given geometry (16 sectors) that is finally used to model the pressure and calandria tubes.

The number of surfaces involved in radiative heat transfer is 32 while the number of sectors is 16, both for the PT and for the CT. Radiation between the PT outside surface and the CT inside surface was included in the model.

(d) Annulus gas model

Annulus gas system provides separation between the PT and CT. In the model, the annulus gas is represented by a hydraulic branch as shown in Fig. 31 (CO_2). This approach allows modelling the heat transfer from the CO_2 gas to the PT/CT annulus. Annulus gas is modelled as a pipe around the channel. Into the annuli, there is a dry carbon dioxide gas atmosphere that prevents tubes corrosion. The annulus gas system provides a thermal barrier between the PT and CT during normal plant operation. The annulus gas length model is the same as the PT length (0.900 m). The annulus pipe is connected by two reservoirs, one at each of its sides. The reservoirs are modelled as pressure boundary conditions and atmospheric pressure was imposed.

(e) Water tank (moderator) model

The water tank (moderator) is represented in the actual model as a large pipe with light water around the CT. The real volume of light water from the tank was included in the model. There is no hydraulic connection with any other node. The moderator temperature is assumed to be 70.6 ºC. The moderator initial pressure is assumed to be atmospheric pressure.

In order to evaluate the heat transferred from the PT/CT contact to the moderator; the moderator model is coupled through heat transfer with the CT.

(f) Pool boiling heat transfer model

Outside surfaces of the CT model are attached to the fluid conditions described by the ‘LIQUID BATH’ option. The surface is horizontal, and the fluid pressure and enthalpy considered were 99.458 kPa and 293 kJ/kg (as per pre-test reported conditions).

4.4.9.3. User options in the heat transfer

CATHENA default correlations have been used to calculate heat transfer coefficient at the wall surface for the heater, pressure tube (inside and outside surfaces) and for calandria tube inside surface. The only exception was related to condensation region where no condensation option was imposed.

CATHENA default correlations have been used to calculate the heat transfer coefficient for the calandria tube outside surface.

For the outside of the calandria tube, the index of the critical heat flux correlation for subcooled and saturated conditions was set to Zubber-Grifitth correlation [18].

Changes from blind to open calculations

The heater is modelled concentric with the PT and CT, i.e. no offset has been considered and non-uniform free convection of argon gas was not included in the model. The heater/PT and CT are each divided in 36 axial nodes, 10 radial nodes and 36 circumferential sectors. The argon gas inside the PT was modelled by a hydraulic pipe with two atmospheric pressure boundary conditions. The temperature of the gas was assumed at 70.6°C. CO_2 was modelled as a hydraulic pipe with reservoirs at each end. Atmospheric pressure was imposed as boundary conditions. The temperature initial conditions have been imposed as 70.6°C, (according to information provided during the blind calculation results presentation). CO_2 flow was imposed as zero. New graphite rod properties (provided during the meeting) have been included in the model. Similarly, the new Zr-2.5% Nb properties for PT/CT specific heat capacity have been used. CATHENA default code properties for Argon and CO_2 have been used. Light water has been considered as the moderator fluid both for the blind and open calculations

The moderator was modelled by a hydraulic pipe with atmospheric pressure boundary conditions at each end. The temperature of the water was assumed initially 70.6°C. The real volume of water has been included for moderator inventory and no other hydraulic connections were included in the model.

The optimum quench temperature correlation, based on the new moderator subcooling methodology, has been introduced directly in the model, based on a subcooling margin of less than 30°C.

The 'FUEL CHANNEL DEFORMATION' auxiliary model was used to model the PT deformation for each sector of the PT. The post contact PT/CT deformation option is selected to model the post-contact straining. The PT deformation is assumed circular. This approach is similar to that used during the blind calculation phase.

The PT/CT contact heat transfer was modelled as occurring over the entire circumference of the PT when PT/CT contact is predicted. The new moderator subcooling methodology contact conductance evolution was assumed both for the blind and open calculations. The PT geometry change is fed back in the model for the PT conduction heat transfer calculation. This approach is applied to both blind and open calculation.

'LIQUID BATH' option/model used in the blind calculation has been completely removed.

Two different models were developed in order to evaluate the independence of results to the modelling parameters. For each case, the heater, PT and CT were placed concentric and no free convection was considered between the heater and the pressure tube. For the first simulation the components (heater, PT and CT) were simulated using 36 axial nodes. For the second simulation, only one node was considered / simulated in the axial direction. For both cases, the number of radial nodes and circumferential sectors were kept constant (10 and respectively 36). The power evolution was distributed uniformly.

For the open calculations, the water tank (moderator) was represented by a pipe with light water around the CT. The moderator boundary conditions were introduced at the ends of the pipe. The pressure boundary was assumed at atmospheric conditions while the moderator initial temperature considered was slightly increased to the median of the RTDs values (70.6°C as recorded during the pre-test conditions). In order to evaluate the heat transferred from the PT/CT contact to the moderator; this model was coupled through heat transfer with the CT.

The results were found to be only slightly affected by the number of axial nodes included in different models. The PT/CT contact time; PT and CT temperatures were almost similar between the cases considered. The time the CT is in dryout conditions is also similar between the two cases. The moderator temperature was predicted to increase during the simulation, but the values are below the recorded test data. The non-transient parameter results are presented in Table 9.

The same two models (1 or 36 axial nodes) have been simulated considering a large volume of water for moderator. Again, the models predicted similar results in terms of PT/CT contact time or PT and CT temperatures. However, due to significantly increased moderator volume included in the model, the moderator temperature observed during the test could not be reproduced. Some differences have been also observed in the evolution of the PT temperatures after the contact between the similar cases but with different moderator volumes. Just after the contact, the pressure tube top sectors temperatures decreased more in case that a larger volume of water is considered in the moderator. However, after about 10 seconds, the values became similar.

The effect of the minimum/maximum running time step was also evaluated. The effect was found to be insignificant (second digit) on each parameter reported for comparison.

TABLE 9. COMPARISON OF THE NON-TRANSIENT PARAMETERS

PARAMETER/CASE	1 AXIAL NODE		36 AXIAL NODES	
	Moderator volume		Moderator volume	
	Real	Large	Real*	Large
Time of first PT CT contact (s)	72.80	72.79	72.81	72.80
Location of first PT/CT contact (m)	0.025	0.025	0.025	0.025
PT temperature at time of contact, axial centre, 0° (°C)	808.9	808.9	809.0	809.0
axial centre, 270° (°C)	808.9	808.9	809.0	809.0
axial centre, 180° (°C)	808.9	808.9	809.0	809.0
Percent of CT Dryout area (%)	36	36	36	36
Max PT temperature (°C)	830	830	830	830

*This set of results has been included as the final open calculation results.

5. SIMULATION COMPARISON WITH EXPERIMENT

5.1. GLOBAL BEHAVIOUR

Establishing a heat balance in a transient experiment is difficult, but the distribution of energy in various components can be determined and an instantaneous pseudo heat balance can be performed using a computer code. The distribution of energy during the test is shown in Fig. 33 using CATHENA code with the measured power (average electrical energy ~147 kW) from the experiments. The energy calculated as shown in Fig. 33 is the cumulative energy based on code estimations when measured electrical power, components temperatures and water temperatures were supplied as boundary conditions. The energy stored in the in the heater is coincident with electrical power until about 40 s in to the transient. From there on less and less heat is stored in the heater as heat begins to radiate to the pressure tube. The stored heat in the heater reaches a plateau around 80 s from where most of the electrical power is radiated out of the heater. The pressure tube began to store heat from about 30 s reaching a maximum around 72 s and then abruptly transferring about 15 kJ to the calandria tube upon contact. The stored heat in the calandria tube increases, upon pressure tube calandria tube contact, by about the same amount of heat transferred from the pressure tube. Following pressure tube calandria tube contact, the stored heat in the water tank increases linearly to reach the stored heat value in the heater at approximately 140 s. The sum of stored heat in the heater, pressure tube, calandria tube and the water is always equal to the heat input from the measured power supply.

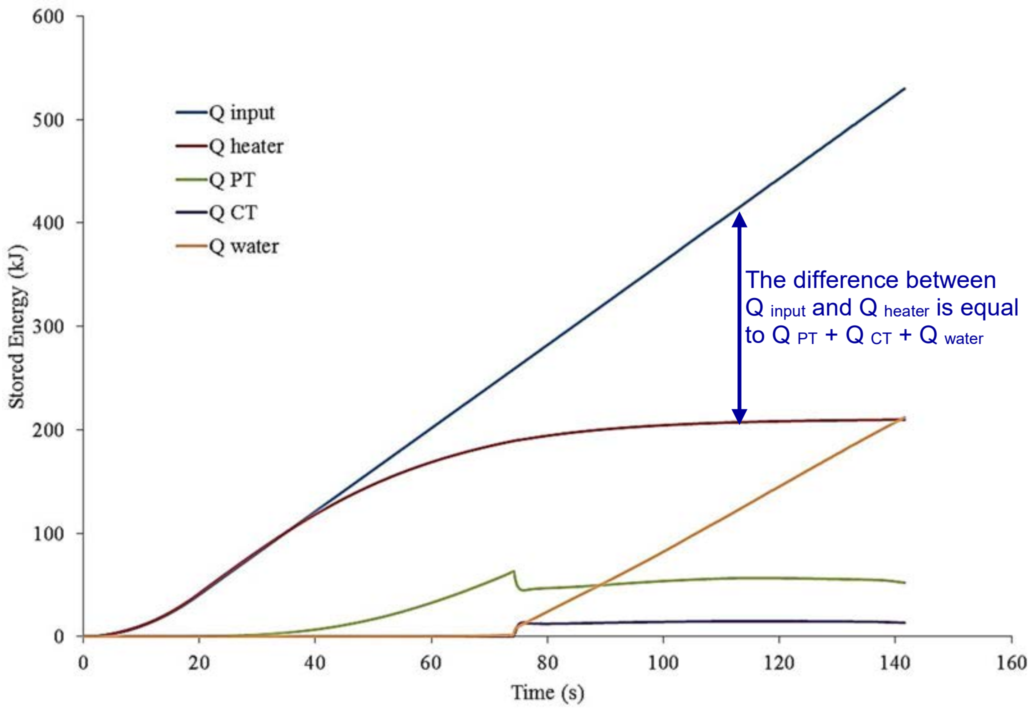

FIG. 33. Calculated energy distribution in the ICSP test showing electrical heat input and stored heat in the heater, pressure tube, calandria tube and water.

The test section internal pressure averaged 3.5 MPa and ranged between 3.4 and 3.7 MPa during the test, as shown in Fig. 34. The pressure was controlled automatically by a control system able to feed and bleed gas as required to maintain the set point pressure. Additional manual venting of the pressure tube section helped maintain the pressure as the test section heated rapidly during the test. The test section was depressurized 64 seconds after initial pressure tube/calandria tube contact and prior to the power being turned off.

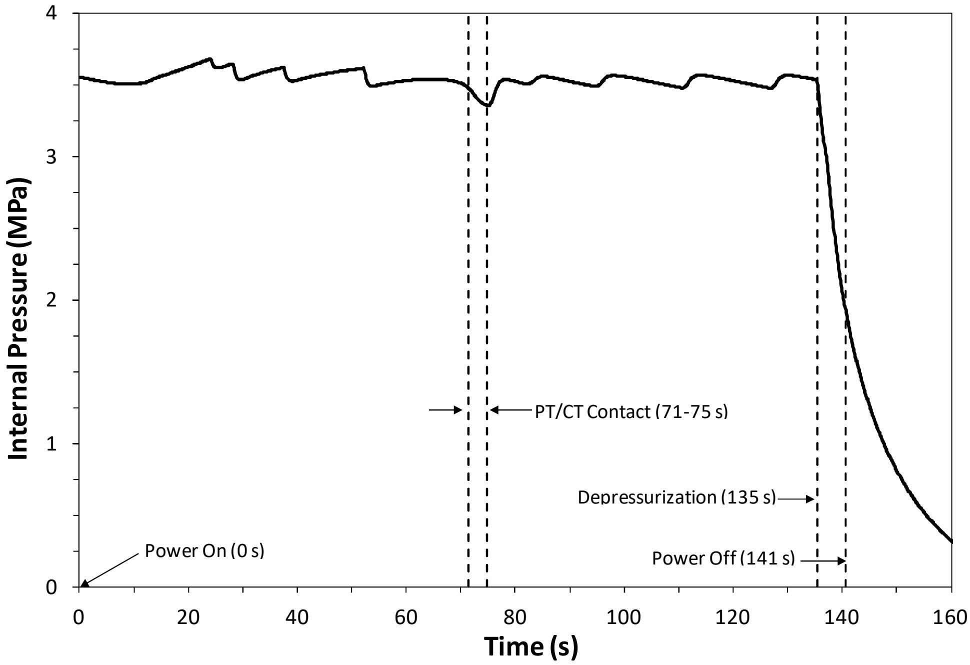

FIG. 34. Test section pressure in IAEA ICSP contact boiling test.

The linear heater power, determined by dividing the measured heater power by the distance between the voltage taps on the heater, is the normalized power to the heater. The linear heater power averaged 164 kW/m and ranged from 159 to 165 kW/m as shown in Fig. 35. To achieve this linear heater power, the power supply set point was ramped to 176 kW (88 kW per rectifier) over 20 s. The power provided by the power supply averaged 179 kW which resulted in an average buss bar power of 166 kW and an average heater power of 147 kW. The linear heater power provides a more representative measurement of the heat supplied to the test section since the voltage taps contact the heater directly, thereby avoiding buss bar losses.

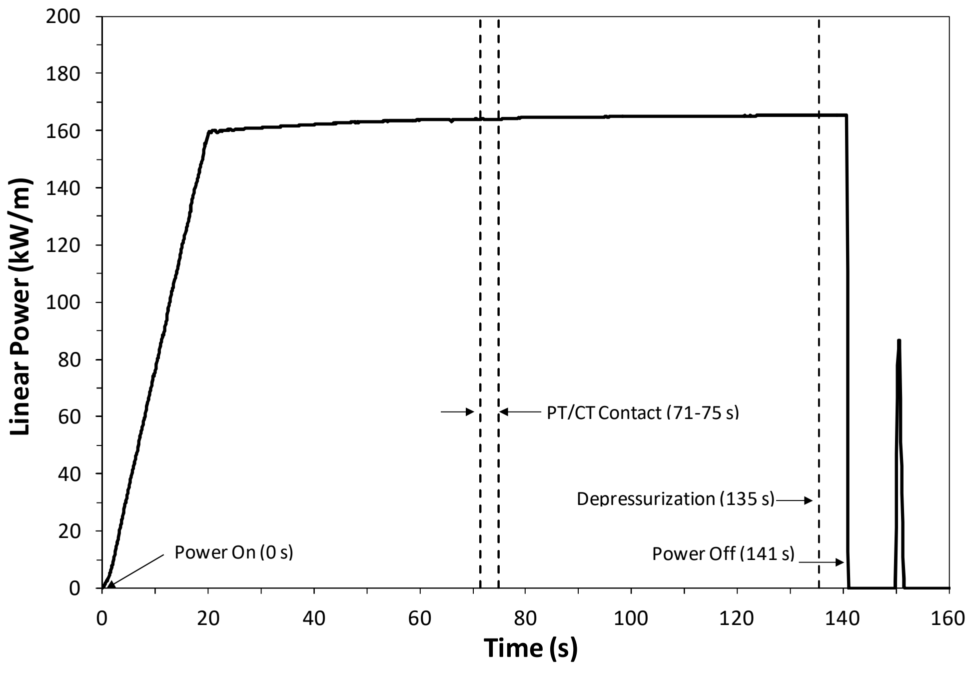

FIG. 35. Linear heater power in IAEA ICSP contact boiling test.

The water temperatures measured above, below and next to the calandria tube surface are shown in Fig. 36. The average water temperature at initial contact was 70.5°C and ranged from 70.1 to 71.1°C with the higher temperature measured below the calandria tube. Taking into account the barometric pressure and the head of water above each resistance temperature detector, the average subcooling was 29.6°C at the time of initial pressure tube/calandria tube contact. Following contact, the temperature surrounding the calandria tube increased as heat was transferred from the test section to the surrounding water, reaching up to approximately 72 to 80°C by the time the test section power was turned off.

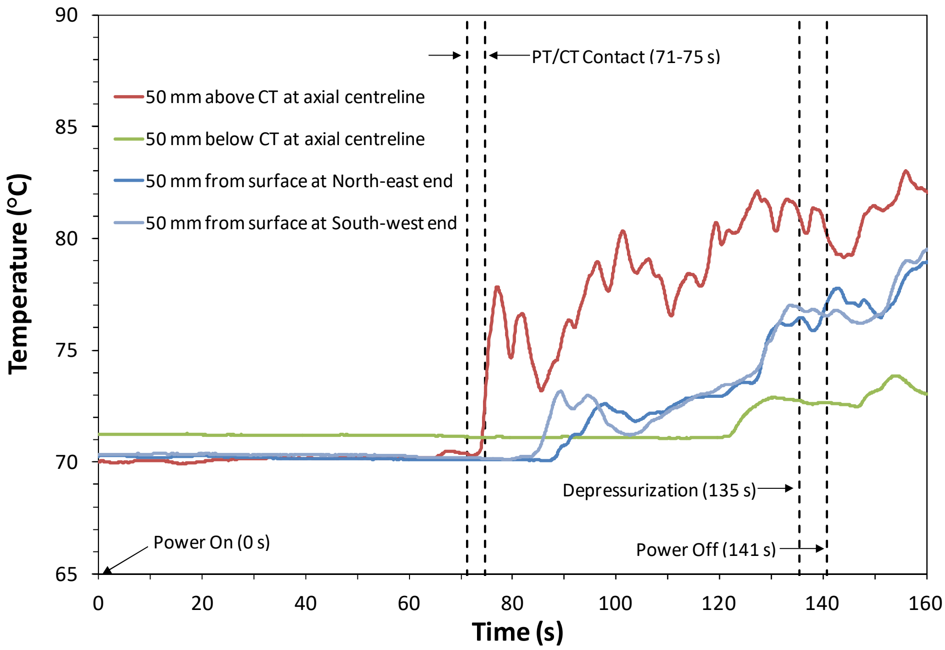

FIG. 36. Measured water temperature in IAEA ICSP contact boiling test.

5.2. PRESSURE TUBE AND CALANDRIA TUBE TEMPERATURES

The pressure tube mid-wall and calandria tube surface temperatures were measured at each of the five axial rings during the test. The temperatures measured at the centreline of the test section (Ring 3) are chosen for comparison to simulation values, shown in Fig. 37. The participants in the ICSP were asked to model pressure tube and calandria tube temperatures with initial and boundary conditions representing the ICSP test. The pressure tube temperatures increased at an average rate[1] of 21.8°C/s in the experiment and reached contact temperatures in the range of 823 to 919°C[2], as shown in Fig. 10. For the ICSP activity, the measured and calculated top, centreline, and bottom temperature transients were used as the comparison. The calculated values shown in Fig. 33 for all participants approximately captured the heat-up rate reasonably well, however, the calculated contact temperatures were lower. In contrast, the calculated contact times were within the same range as the measured values, except for one calculation, as shown in Fig. 38. The predictions by SNN was significantly different due to misconceiving the units for heater power (nevertheless, these results are included according to rules adopted for the blind simulation submissions). In a subsequent analysis, labelled SNN New, the misconceived input parameter was corrected, and the calculation agreed with the rest

---

[1] The heating rate is determined between the temperatures of 350 and 650°C.
[2] The peak temperature of 1018°C, measured by TC0, is considered to have been affected by direct radiation from the heater. The data is not used in the analysis.

of the participants. The calculated post contact pressure tube temperature was not in good agreement with the measured temperatures. None of the participants were able to obtain the quasi steady ~700°C post contact temperature observed in the test. Similar observation can be made to the pressure tube temperatures calculated from the side (Fig. 39) and at the bottom (Fig. 40). The calculated and measured pressure tube contact temperatures are shown in Fig. 41. Consistently, the calculated pressure tube contact temperatures were lower at the top and the bottom of the pressure tube, whereas on the sides, the agreement was somewhat better compared to the top and the bottom.

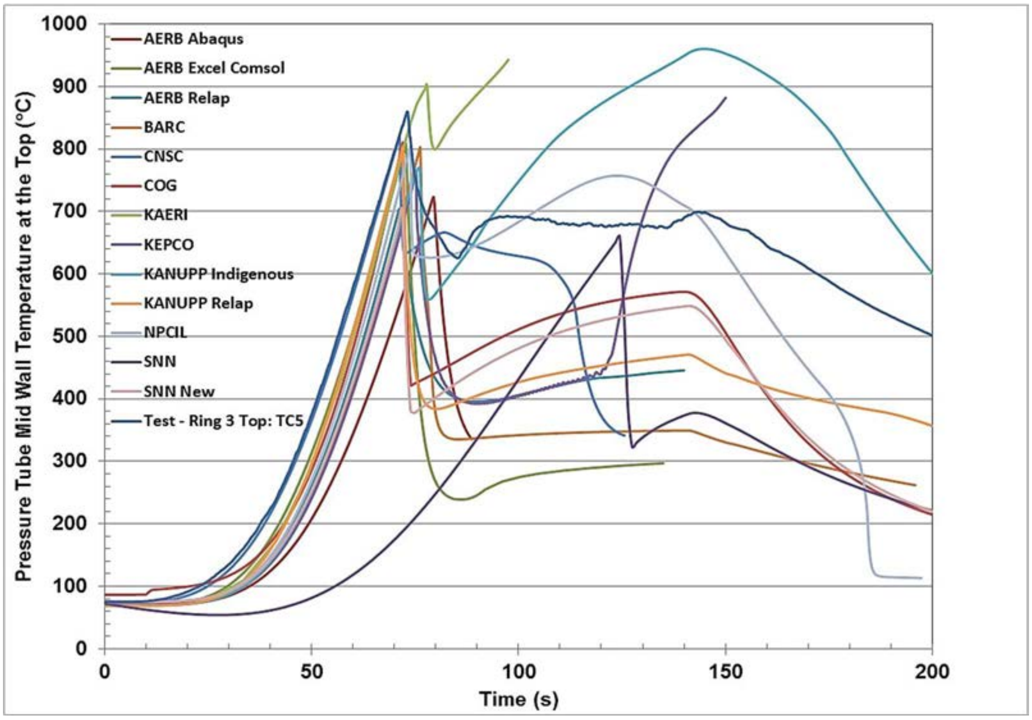

FIG. 37. Comparison of calculated and measured pressure tube temperature at the top of Ring 3.

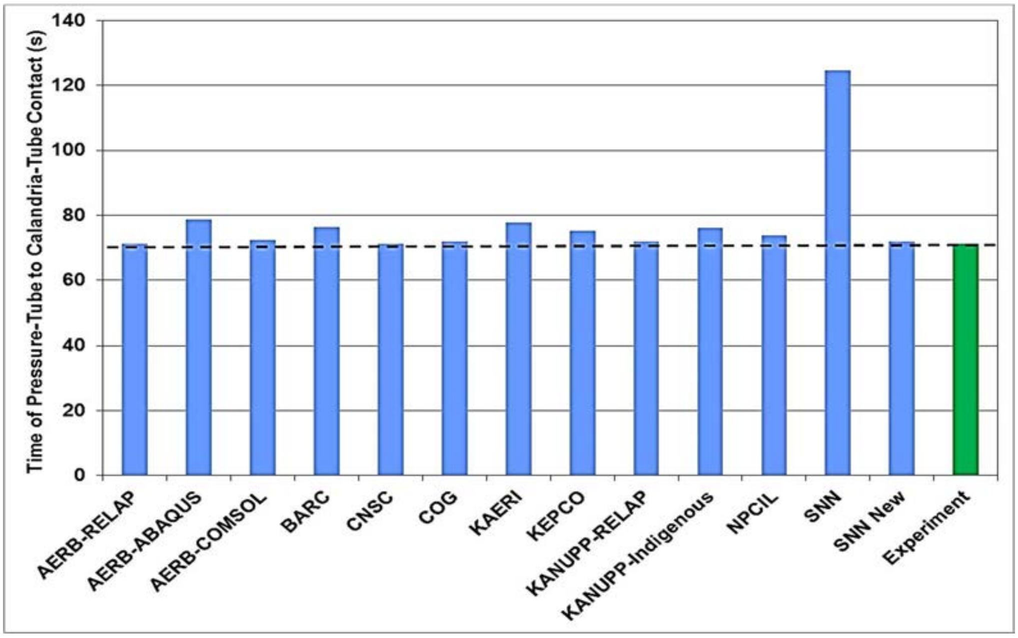

FIG. 38. Comparison of calculated and measured pressure tube to calandria tube contact time.

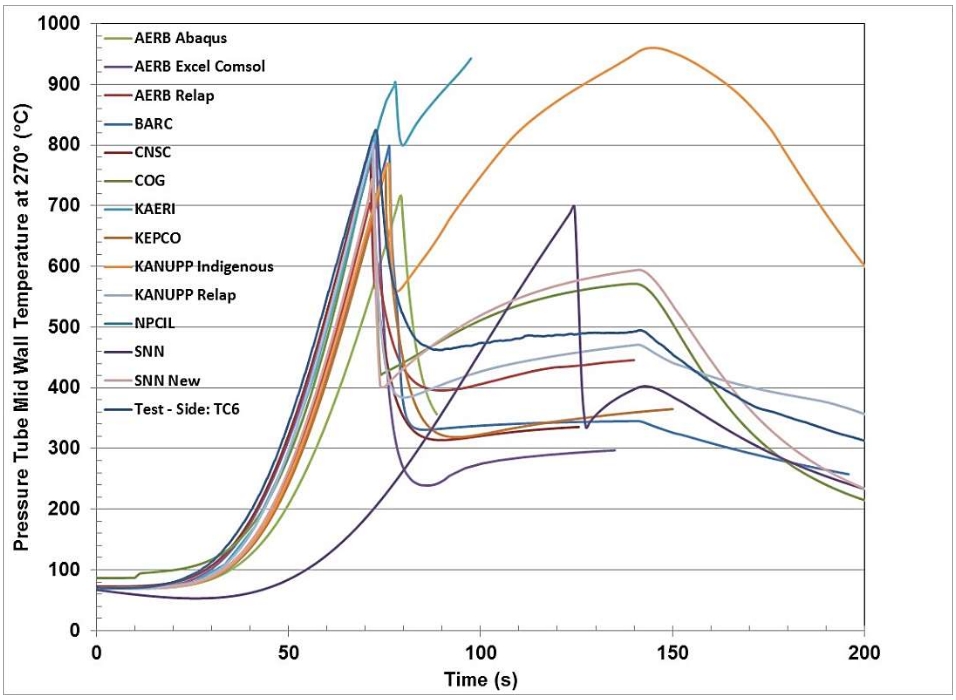

FIG. 39. Comparison of calculated and measured pressure tube temperature at the side in Ring 3 during the ICSP test.

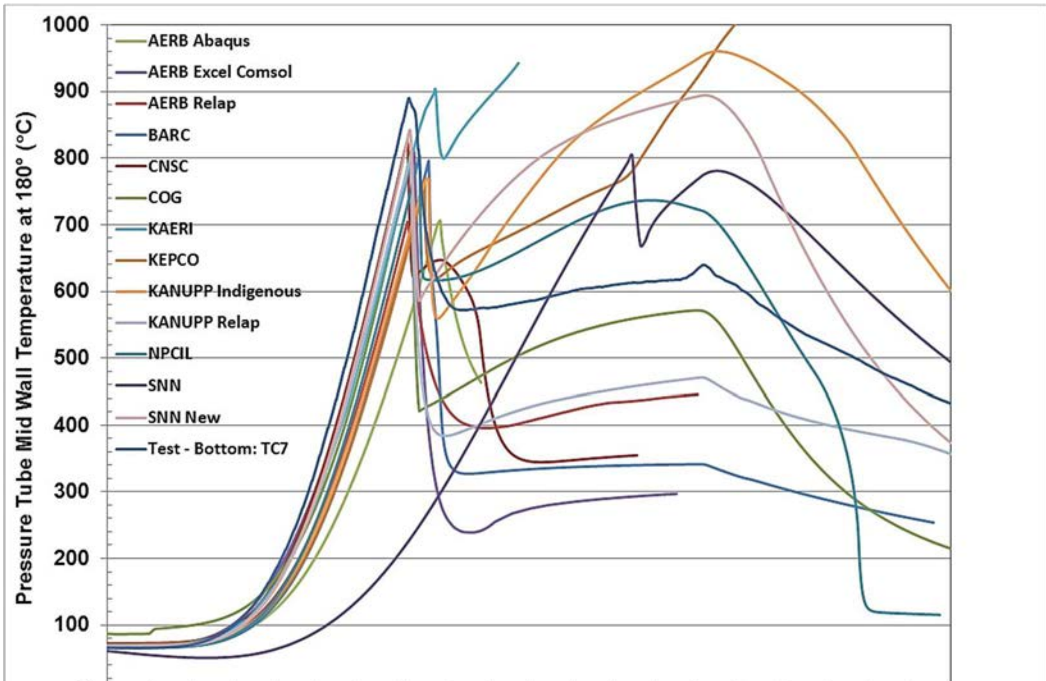

FIG. 40. Comparison of calculated and measured pressure tube temperature at the bottom in Ring 3 during the ICSP test.

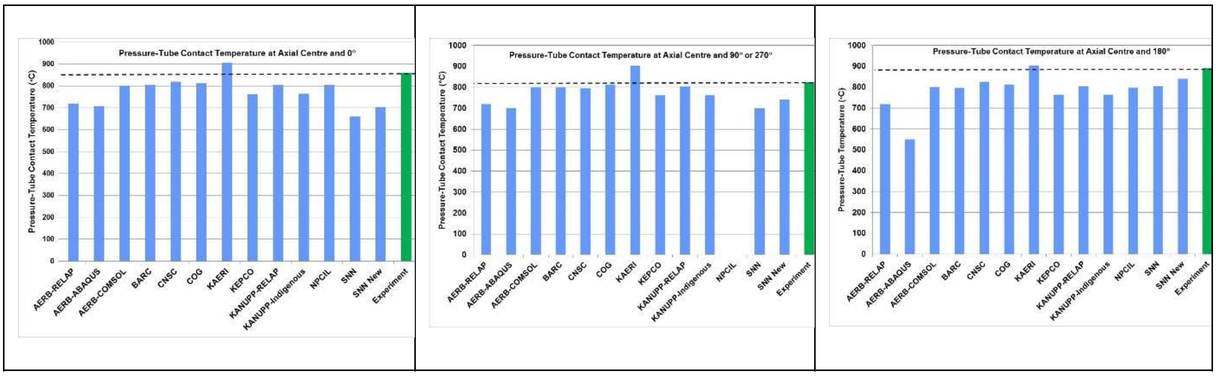

FIG. 41. Comparison of calculated pressure tube contact temperature at the top, sides and the bottom in Ring 3 during the ICSP test.

Following contact in the ICSP test, about half of the calandria tube thermocouples indicated film/transition boiling (six thermocouples) or immediate quench (15 thermocouples) while the other half of the thermocouples indicated nucleate boiling (19 thermocouples). The peak calandria tube temperature of 649°C occurred at the top of Ring 4. Four of the six thermocouples that indicated dryout conditions were located at the top of the calandria tube. The two thermocouples at the top of Ring 3 (centre) and Ring 1 (west) reached 540 and 562°C, respectively, and both remained in film boiling above 220°C for approximately 10 seconds. The thermocouples at the top (Fig. 4) of the tube and east of the centreline at Rings 4 and 5 reached peak temperatures of 649 and 583°C, respectively, and quenched in 20.8 and 14.3 seconds. The calandria tube thermocouple at the top of Ring 2 only reached 126°C, although some thermocouples at the side of Ring 2 reached up to 385°C. The peak temperatures were higher and the length of time in dryout was longer for the calandria tube thermocouples at the top of the tube (Fig. 42) compared to the thermocouples located on the sides and the bottom.

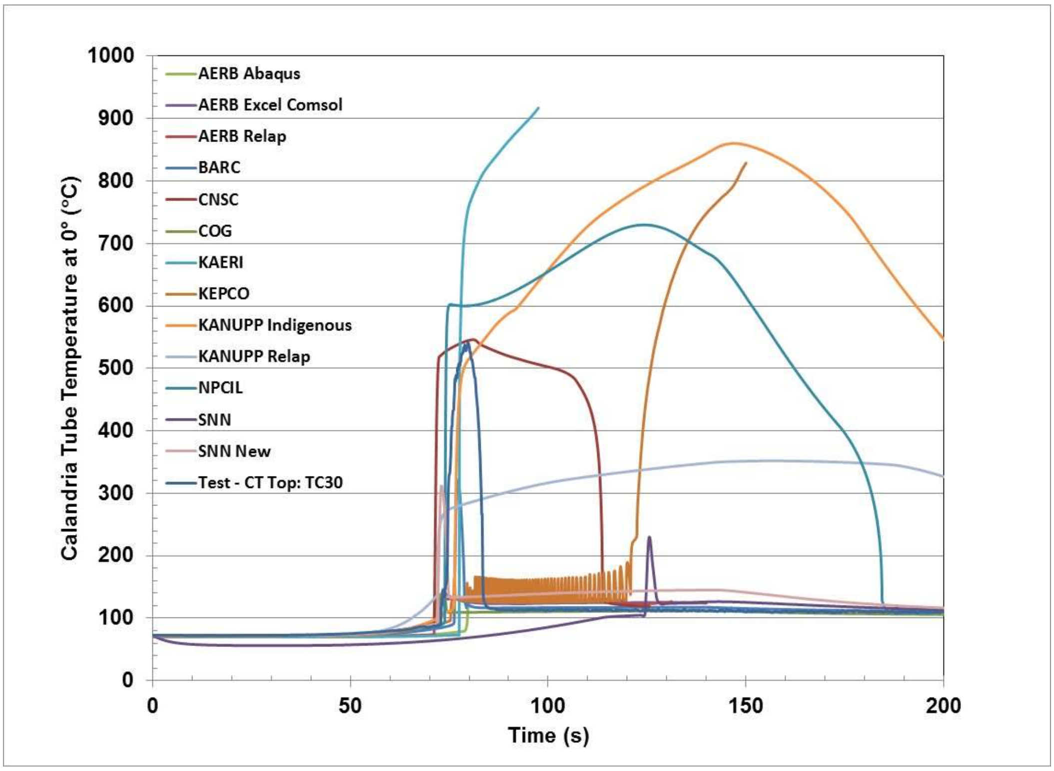

FIG. 42. Comparison of calculated and measured calandria tube temperature at the top in Ring 3 during the ICSP test.

A comparison of calculated and measured calandria tube temperature at the top of Ring 3 is shown in Fig. 42. Except for one calculation (SNN New), all calculations indicated a higher calandria tube temperature than the measured peak calandria tube temperature of ~550°C. The calculation performed by the CNSC was remarkably close to the peak calandria tube temperature, however, the extent of dryout period calculated was about four times longer than the measured period. Some of the participants were not able to calculate calandria tube temperatures because their finite element codes did not have the capabilities to model heat transfer from a solid to water.

The calculated calandria tube temperatures at the bottom of the calandria tube are shown in Fig. 43. Close examination of the time just after contact indicates that six of the calculations were able to reproduce the immediate quench observed in the test. The five other calculations predicted sustained film boiling. The majority of the calculations predicted some boiling and the rise in calandria tube temperature following pressure tube contact.

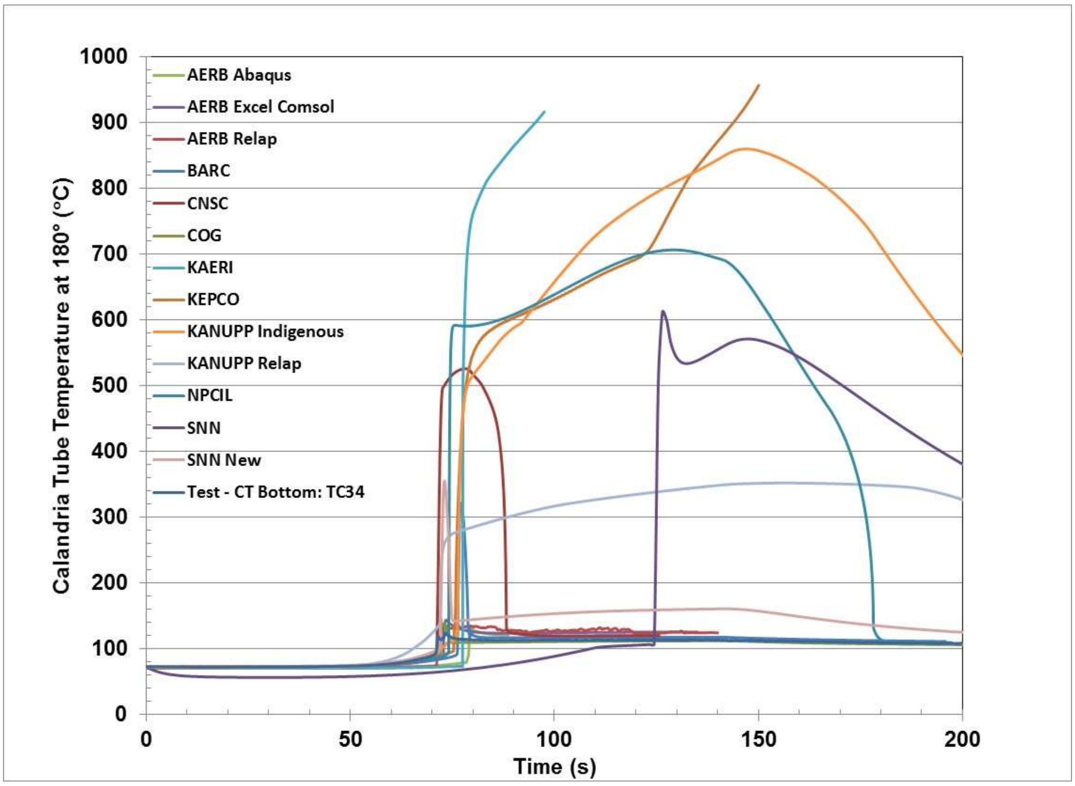

FIG. 43. Comparison of calculated and measured calandria tube temperature at the bottom in Ring 3 during the ICSP test.

5.3. CONTACT BEHAVIOUR (CONDUCTANCE AND CONTACT SPREADING)

The participant from BARC calculated the heat transfer between the pressure tube and the calandria tube using a gap closure model. The model is defined as:

$$q'_{\mathrm{pt-ct}} = (1-f)q'_{\mathrm{gap}} + f q'_{\mathrm{cnt}} \quad (94)$$

where f is the contact status between the pressure tube and the calandria tube. The term f is equal to 1 if pressure tube has contacted the calandria tube otherwise it is assumed equal to 0. The term q'_{gap} is defined as:

$$q'_{gap} = q'_{radn} + q'_{g,cond} \quad (95)$$

The gas conduction, $q'_{g,cond}$, is evaluated as a function of radial distance between the pressure tube and the calandria tube. The term $q'_{g,cond}$ can be significantly high when pressure tube approaches the calandria tube due to ballooning creep. The term q'_{radn} is the radiation heat transfer term evaluated using two concentric cylinders.

The pressure tube to calandria tube contact heat transfer, q'_{cnt}, is calculated based on contact conductance, h_{cnt}, as described by:

$$q'_{cnt} = h_{cnt} A_{cnt} (T_{opt} - T_{ict}) \quad (96)$$

where, A_{cnt} is pressure tube to calandria tube contact area equivalent to the inner surface area of calandria tube under fully ballooned condition, T_{opt} and T_{ict} are outer and inner surface temperature of pressure tube and calandria tube, respectively.

The participant from the Canadian Nuclear Safety Commission proposed a randomized pressure tube to calandria tube contact conductance, as illustrated in Fig. 44. They postulated that this contact conductance, and its distribution, is one of the key parameters of the simulation that impacts the boiling regime on the outside of calandria tube. The method calculated an average value of initial contact conductance using a few runs with different average values and comparing them to dryout maps with other contact boiling experiments. From these comparisons, a contact conductance of 12.5 kW/(m^2·K) was selected. The calandria tube surface was divided into a manageable number of discrete squares (like pixels) and each square was assumed to have a finite surface pair of pressure tube and calandria tube. These squares were randomly allocated an initial contact conductance within ±50% from average. The initial contact conductance for each finite surface pair is assumed constant for a duration that is empirically derived in relation to its selected magnitude. The initial conductance was then assumed to decrease to a steady value of 2.5 kW/(m^2·K) over a period of 0.5 s.

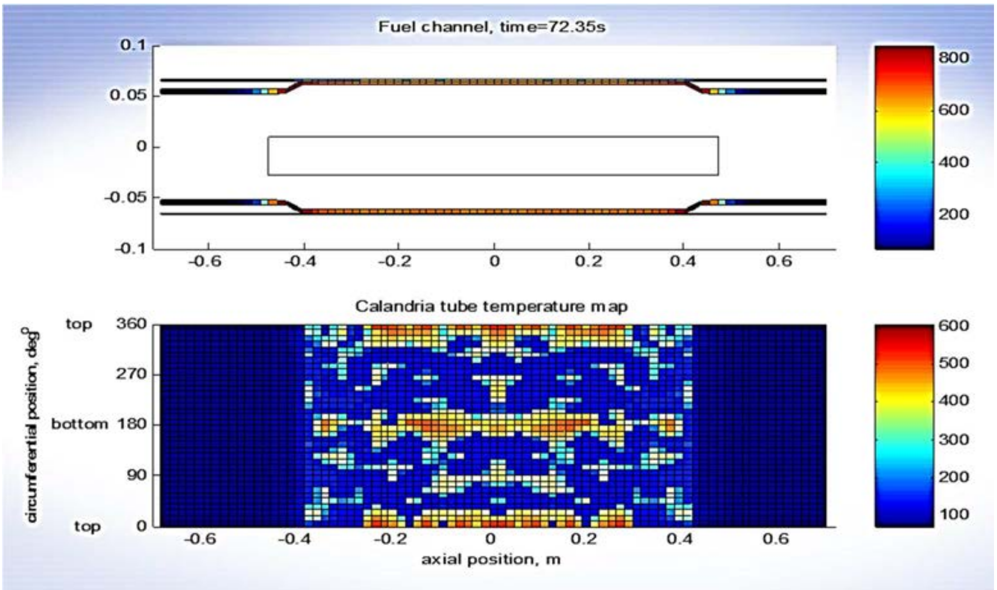

FIG. 44. CNSC's random contact conductance model predicting randomly distributed dryout patches.

5.4. DRYOUT BEHAVIOUR

The calandria tube temperature calculated by lumped parameter codes is an average for the entire length of the tube (the only exception to this statement is the simulation technique adopted by the CNSC participant). This averaged prediction is at odds with the boiling phenomena taking place on the calandria tube during the test. For example, the post-test dryout surface shown in Fig. 45 has random dryout locations dispersed throughout the surface. In all of the dark surfaces the surface temperature exceeded the minimum film boiling temperature of 220°C and is assumed to demarcate film boiling from transition boiling. The darker regions in Fig. 45 appear only when the surface is in film boiling for sufficiently long period of time to oxidize. A post-test photograph of the oxidized surface is shown in Fig. 46. The area not covered by film boiling is either in transition boiling or nucleate boiling. These regions have a lower surface temperatures and high heat transfer coefficient compared to the regions in film boiling. The net effect of this large area (about 78%) is to remove heat from the calandria tube and the pressure tube into water. The lumped parameter codes do not have the ability to capture this heat transfer mechanism and thus would overestimate the time required to cooldown the overheated pressure tube. The net result of this anomaly between the code and the reality is that the codes tend to overpredict the time in dryout (assuming all other parameters being equal).

The percent dryout in most of the codes are calculated indirectly. In a code that can have circumferential sectors and axial nodes, the boiling regime on the surface is assessed via the boiling index calculated at each time step. Once the boiling index indicates film boiling, the code assumes the entire surface defined by the sector to be in film boiling. The area of sectors indicated to be in dryout versus the total surface area is assumed to be the percentage in dryout.

The oxide discoloration on the outside surface of the calandria tube resulting from elevated surface temperatures during film boiling provides a post-test measure of the extent of film boiling that occurred upon pressure tube/calandria tube contact. After the test, the areas of dark brown, black or blue discoloration were transferred to transparency, scanned to electronic format, and then analysed using image analysis software to determine the percent of the heated area that experienced dryout (22% in this test). The reference heated area is taken as the shoulder–shoulder length of the heater, which was ±475 mm from the axial centreline of the test section. The dryout map determined using this method is shown in Fig. 45.

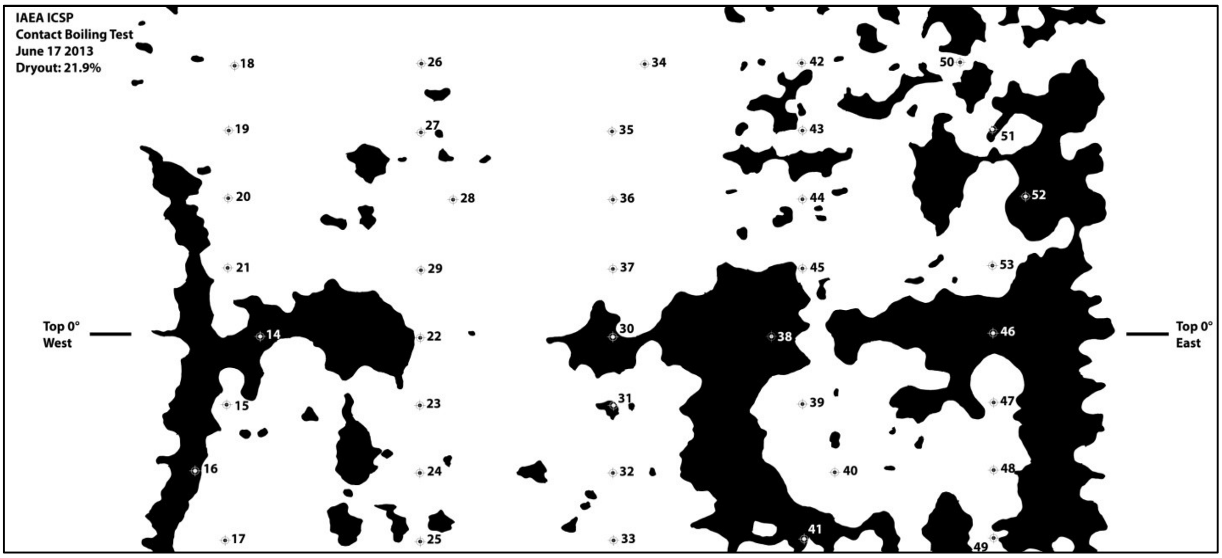

FIG. 45. Map of dryout pattern with oxidized areas due to film boiling shown in black.

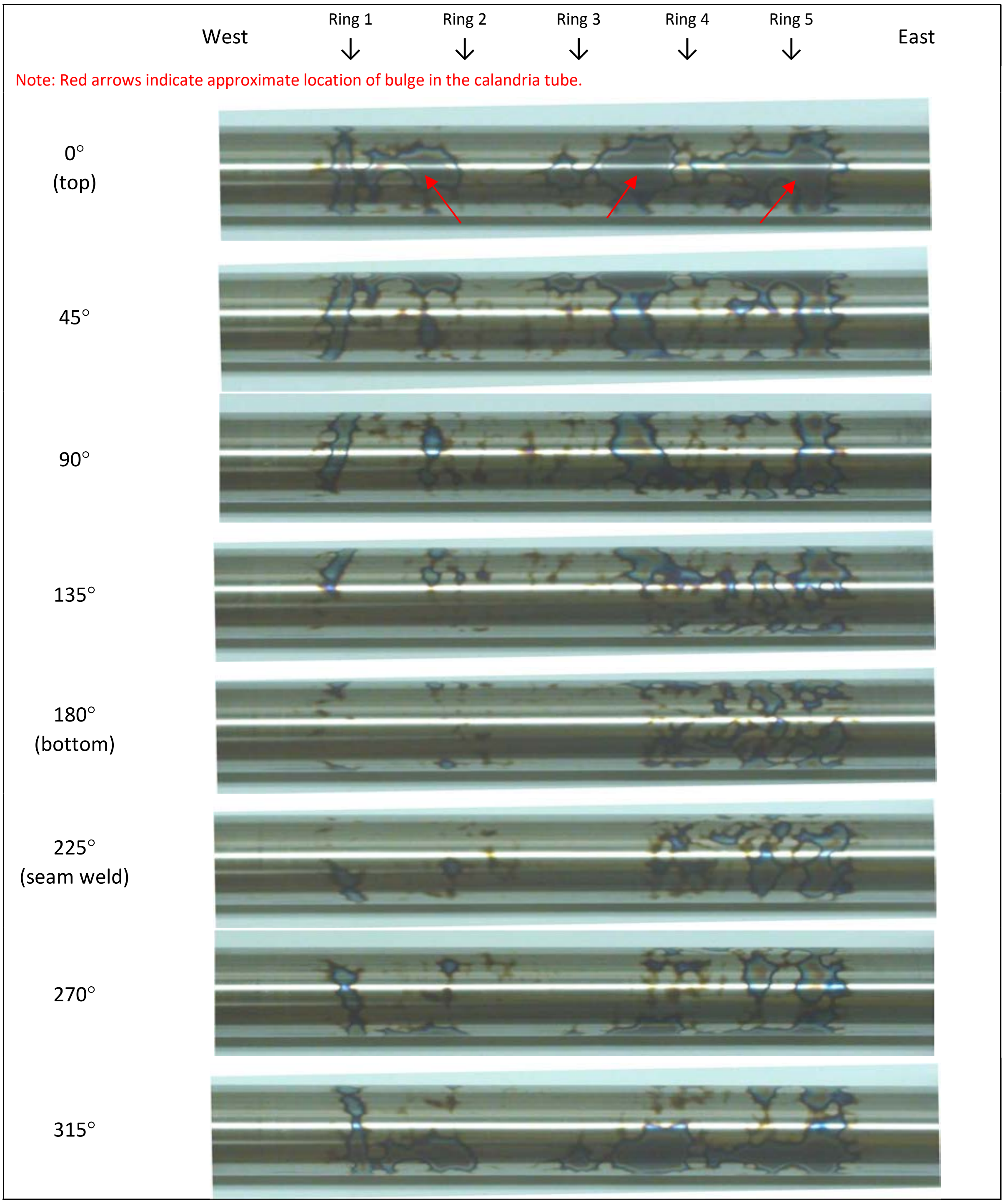

FIG. 46. Photographs of oxide discoloration on the calandria tube in the IAEA ICSP contact boiling test.

The dark oxide patches on the surface covered 22% of the heated area. The peak temperature measurements in the large dryout patches correspond to the highest temperature measurements of 649°C and 583°C at thermocouples 38 and 46. Since the calandria tube thermocouples did not rewet within 20 seconds and the dryout area was between 16 and 50%, the test was deemed patchy film boiling.

As observed from the video of the test, the pressure tube first contacted the calandria tube close to the bottom of the test section near the axial centre (Ring 3) and near the west end (Ring 1) of the test section shown in Fig. 47. The pressure tube contact spread axially along the bottom between these two locations and circumferentially around the tube.

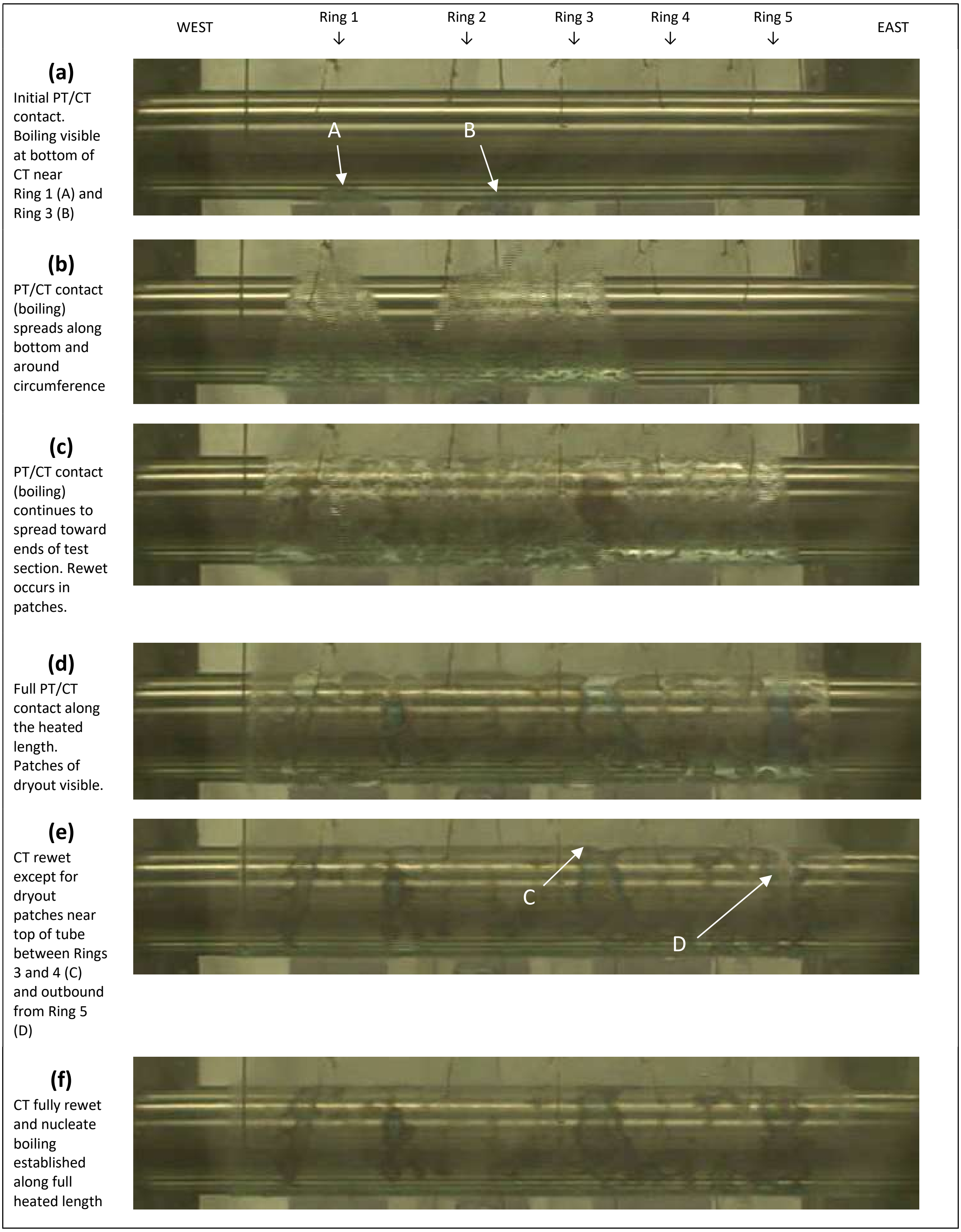

FIG. 47. Still frames from video of the south side of the test section in the IAEA ICSP contact boiling test.

Contact then spread toward the east end of the heated test section, and full contact over the heated length was achieved within approximately 4 s. As the pressure tube/calandria tube contact quickly spread, it caused vigorous boiling on the surface of the calandria tube. The surface rewet quickly near the centreline, before contact occurred at the eastern most edge of the heated length. The top of the tube near the east end took approximately 20 s to rewet[3]. Oxidation, hence dryout, was also concentrated around the side of the tube near the west end of the heated zone outboard from Ring 1, toward the east end of the tube between Ring 3 and 4, and near the east end of the heated zone outboard from Ring 5.

The percent dryout calculated by the participants are shown in Fig. 48. Not all participants were able to calculate dryout and therefore only five calculations among the 13 entries are shown in the figure. The percent dryout calculated by SNN was very close to the experimentally measured dryout, however, the revised SNN New was 30% too high. The percent dryout calculated by COG and the CNSC were 10 and 20% too high, respectively. The calculation completed by NPCIL can only distinguish between dryout (total) and no dryout condition. Since the test showed partial dryout, NPCIL calculation identified this as complete dryout.

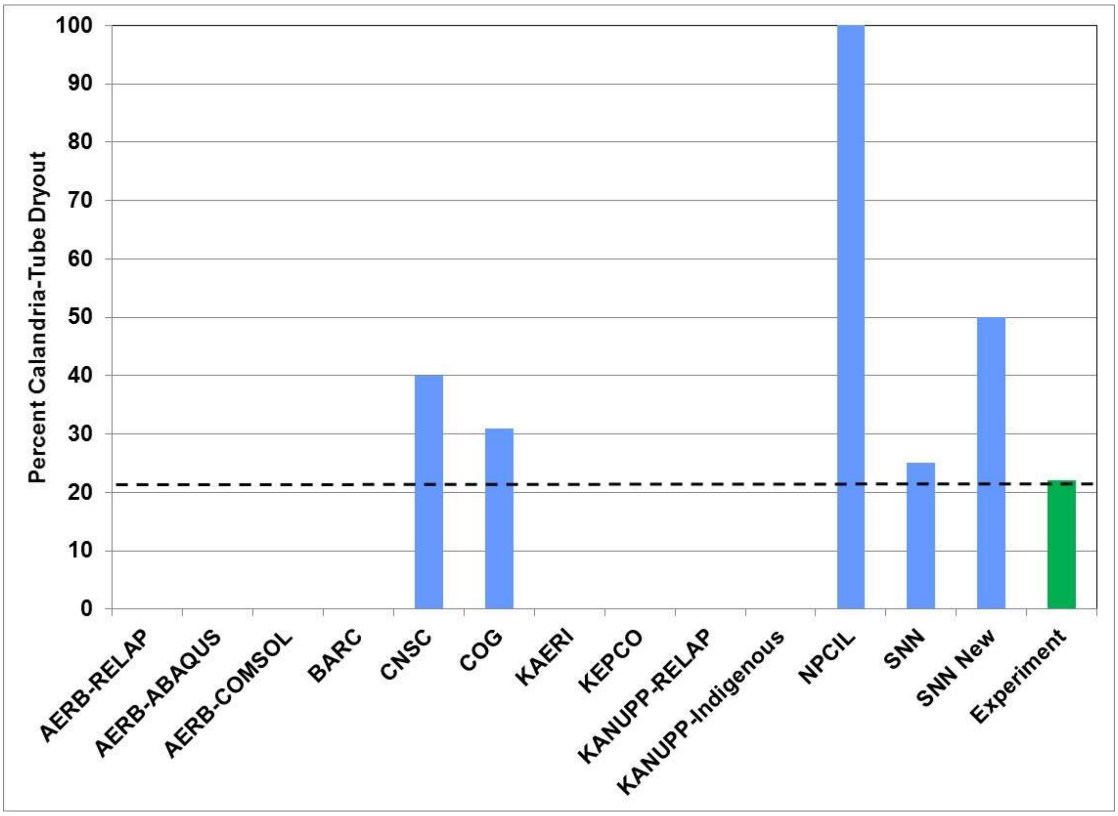

FIG. 48. Percent dryout calculated by ICSP participants.

Figure 49 shows the wall thickness and strain every 15° around the circumference of the pressure tube at each of the five axial rings. The strain averaged 15% and ranged from 8 to 29%. The maximum strain occurred at the bottom of the pressure tube at each of the axial locations, which is typical of the strain from contact boiling experiments. The maximum post-test pressure tube wall thickness, and minimum strain, was at ±45° from the top of the tube.

---

[3] The timing of calandria tube rewet outside the instrumented areas on the test section determined from the video is approximate.

The calandria tube pre- and post-test wall thickness measurements at the instrumented axial ring locations did not indicate any calandria tube strain at the instrumented locations of the calandria tube. However, a small amount of deformation could be discerned along the top of the calandria tube within the largest three dryout patch locations, as shown in Fig. 50. The calandria tube was sectioned and additional wall thickness measurements were taken using a point micrometer around the circumference of the tube within the bulge locations. The axial locations chosen were the points where a minimum wall thickness was measured at the top of the tube within each bulge region. The maximum calandria tube hoop strain was then estimated from these wall thickness measurements. The maximum local true radial strain measured was 2% in the dryout area west of Ring 2, 2% within the dryout area west of Ring 4 and 3% within the dryout area east of Ring 5. The calandria tube hoop strain was estimated to be 0.2% in the dryout area west of Ring 2, 0.4% within the dryout area west of Ring 4 and 0.2% in the dryout area east of Ring 5.

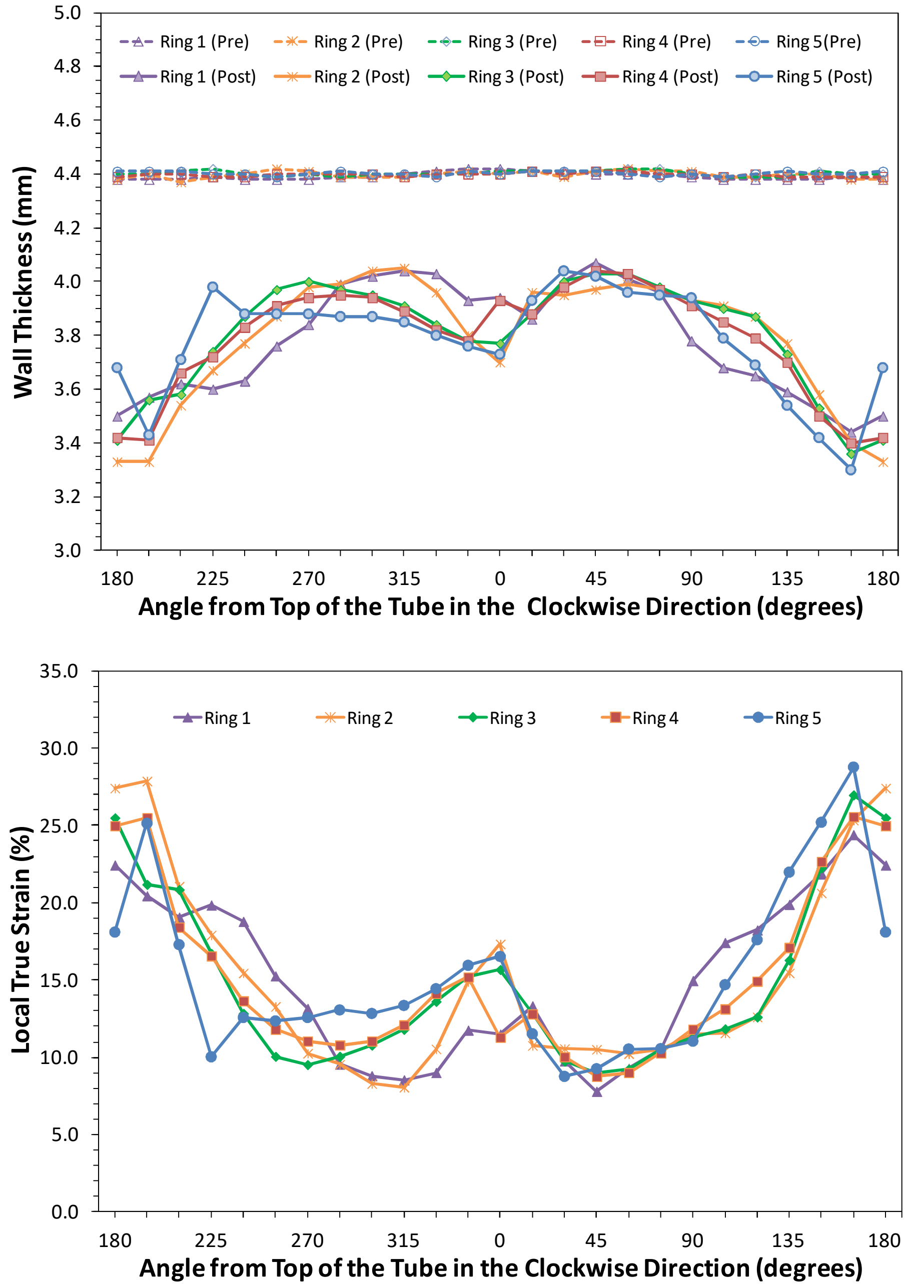

FIG. 49. Pressure tube wall thickness and strain measured in IAEA ICSP contact boiling test.

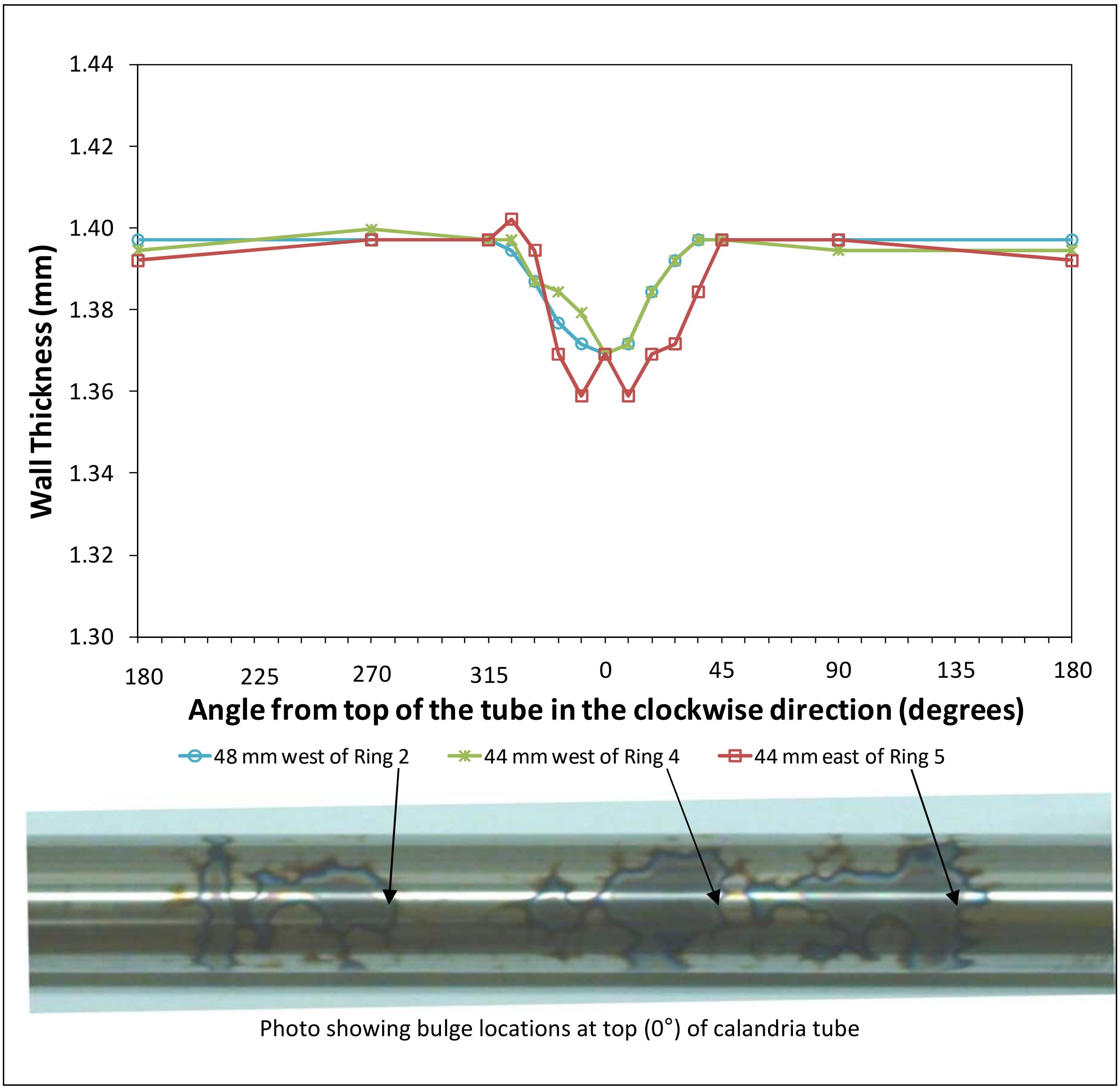

FIG. 50. Calandria tube wall thickness and strain measured in IAEA ICSP contact boiling test.

The pressure tube wall strain calculations completed by the ICSP participants are shown in Fig. 51 and Fig. 52 for top and bottom locations, respectively. Three participants calculated pressure tube strain at the top of the pressure tube well within the expected range. During a contact boiling experiment, the pressure tube reaches an average final wall strain of 16% when it balloons until calandria tube contact. Any additional deformation can take place only when extensive dryout occurs on the calandria tube or when the tube deforms nonuniformly. Fig. 52 compares the measured and the calculated pressure tube wall strain at the bottom of the pressure tube where higher deformation occurred, due to the proximity of the offset heater. The measured wall strain at the bottom was approximately 26%.

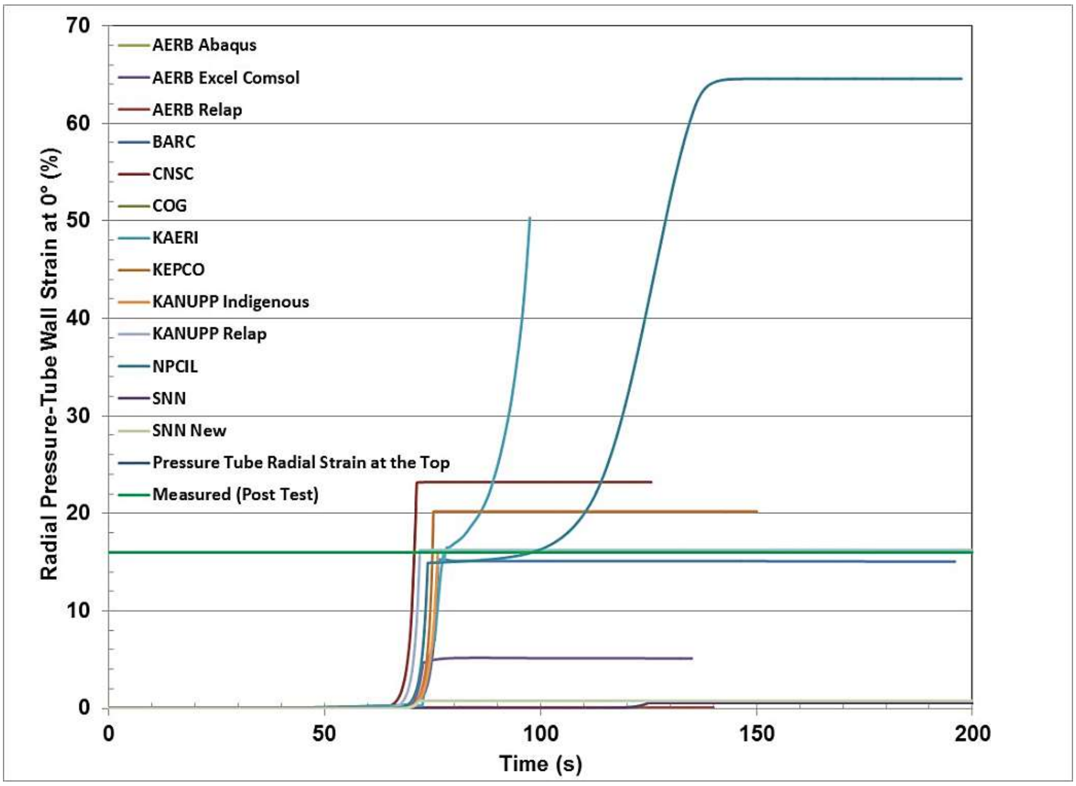

FIG. 51. Comparison of calculated and measured pressure tube wall strain at the top in the ICSP.

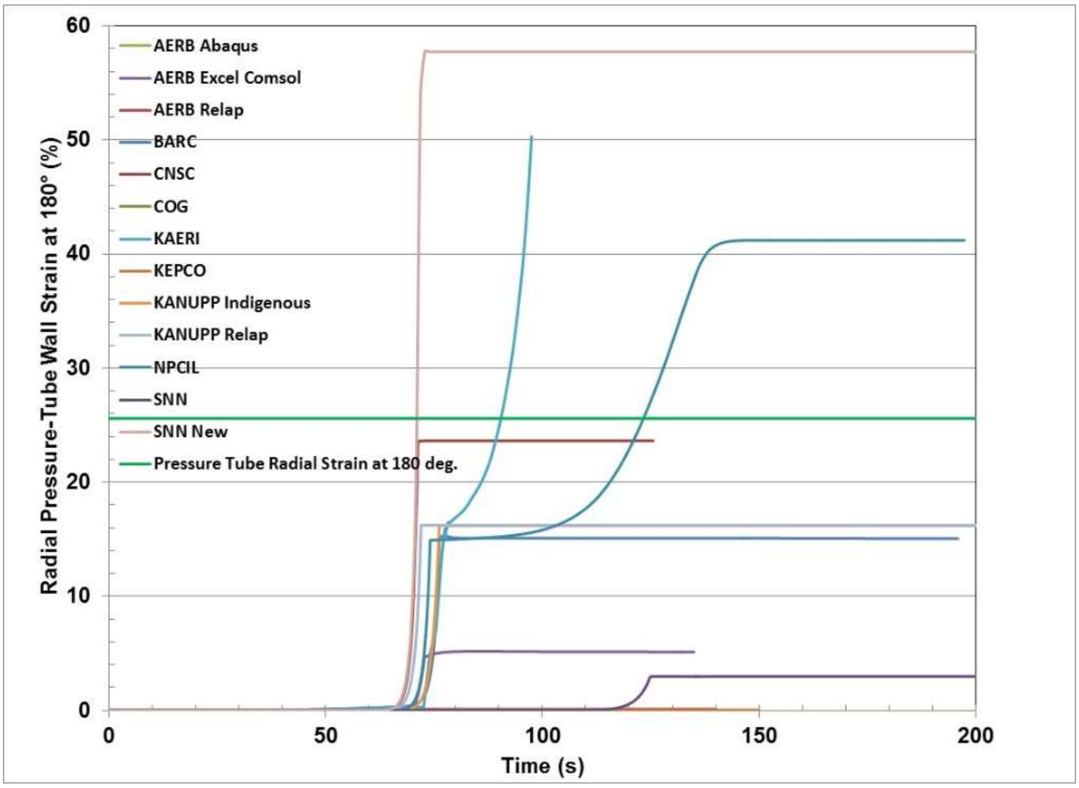

FIG. 52. Comparison of calculated and measured pressure tube wall strain at the bottom in the ICSP.

6. LESSONS LEARNED

6.1. EXPERIMENTAL

The IAEA ICSP contact boiling tests results are consistent with the results of previous contact boiling experiments performed with as-received calandria tubes and internal pressure of 3.5 to 4 MPa. The experiments show that contact boiling behaviour becomes more severe as subcooling decreases at a given heating rate — increasing from immediate quench (○) through small patches (◔) and patchy (◒) to extensive (◕) and entire surface (●) in film boiling. For a given subcooling and internal pressure, higher pressure tube heating rates, which indicate a higher power supplied to the test section, increase the extent of film boiling and therefore the larger the area in dryout.

The IAEA ICSP on HWR moderator subcooling requirements is valuable for the development and validation of computer codes for the analysis of fuel channel integrity. The ICSP test investigated relevant phenomena and the Standard Problem exercise simulated the experiment to assess computer code capabilities used in predicting subcooling requirements for an overheated pressure tube that is plastically deforming into contact with a calandria tube under accident conditions. This objective was met in the completed ICSP exercise.

6.2. CODE/MODEL CAPABILITIES AND DEFICIENCIES

The ICSP simulations required a coupled thermal and structural analysis for the simulation of the contact boiling test completed for this activity. The thermal analysis required radiation, conduction and convection heat transfer capabilities in the code. Heat transfer models were required for free convection within the pressure tube; radiation from heater to pressure tube and from pressure tube to calandria tube; contact heat transfer between pressure tube and the calandria tube after ballooning contact; liquid convection and boiling heat transfer from outer surface of the calandria tube to water. The structural analysis requirements included elasto-plastic deformation of Zr-2.5 Nb pressure tube and Zr-4 calandria tube. Although majority of the codes possessed all of the analysis tools required, there were variations in how they are implemented, especially with contact heat transfer and pool boiling heat transfer. These two models combined with user effect probably covered the entire range of scatter observed in the simulations.

6.2.1. Heater models

All of the codes used in the ICSP study calculated the heater temperature consistently (Fig. 53) using the measured input power and graphite heater thermal properties supplied to the participants. This is one of the benchmarks that is indicative of very consistent radiation heat transfer models available in the codes. Some minor differences occurred due to the differences in pressure tube ballooning deformation models. The temperature decay curve calculated by four participants, after the power was turned off at 141 s, is also reasonably consistent.

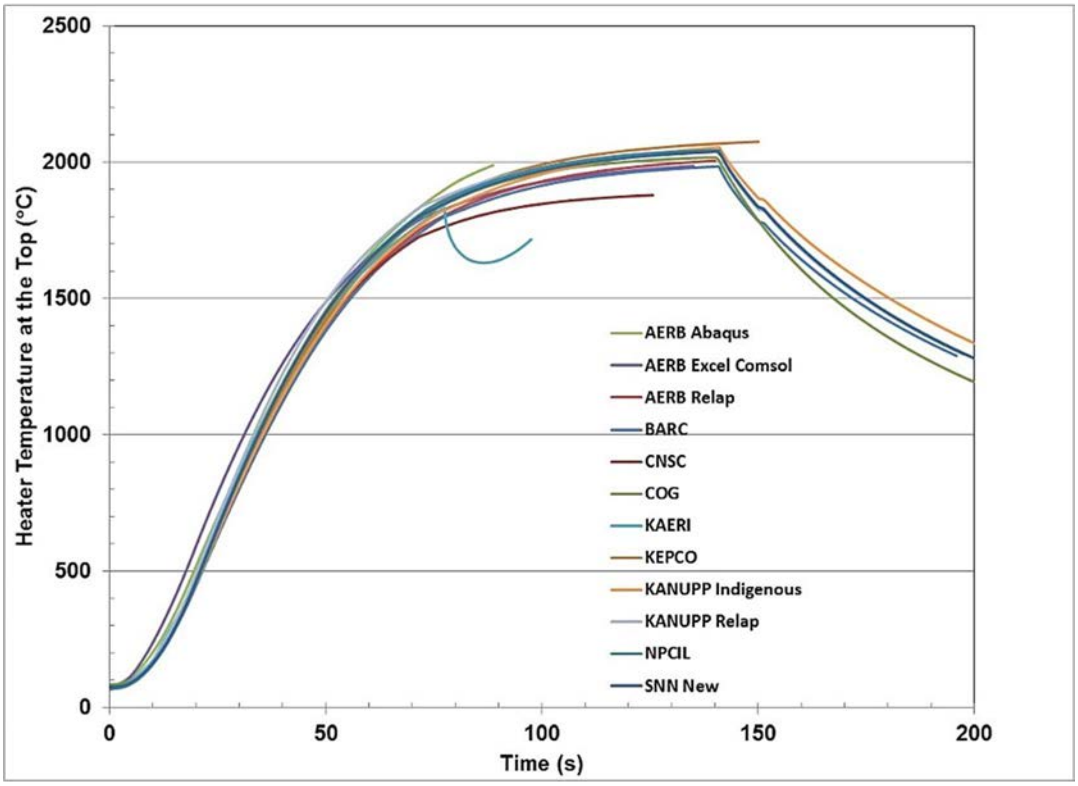

FIG. 53. Comparison of calculated heater temperature at the top in the ICSP.

6.2.2. Deformation models

The calculated pressure tube temperatures during initial heating period before contact are generally lower than the measured temperatures (Fig. 37, Fig. 39, Fig. 40). Several factors can contribute to this difference. The first factor is the uncertainty in the measured temperatures. Several separate effects tests completed at CNL indicate that this uncertainty cannot be the sole contributor to the difference. New information on temperature-dependent specific heat for Zr-2.5 Nb shows that the material properties (assumed as Zircaloy) could be a significant contributor to the differences in calculated pressure tube temperature. An improved understanding of this behaviour is required. The third factor is the effect of free convection within the pressure tube and graphite heater annulus space. Almost all codes had no free convection models to handle the heat transfer due to density driven argon flow within the pressure tube, however, these effects are present in a horizontal test section. Although the experiment incorporated an offset heater to minimize preferential ballooning at the top, it is reasonable to expect some contribution from these phenomena on measured pressure tube temperature. Further investigation of this uncertainty is recommended.

The calculated pressure tube contact temperatures were lower than the measured contact temperature. The difference between measured and calculated contact temperatures were lower at the sides (90° and 270°) than at the top or at the bottom (Fig. 41). In contrast, the time of pressure tube contact with the calandria tube is reasonably close to measured contact time (Fig. 38).

6.2.3. Contact models

The pressure tube to calandria tube contact models have two main factors. The first factor is the Shewfelt correlation [7], required for structural mechanical calculations to estimate plastic deformation of the pressure tube based on the radiation heat load from the heater. The second factor is the transient pressure tube to calandria tube contact heat transfer. Both factors affect the total heat transferred to water from the heater via the calandria tube. Most participants used similar models for heat transfer to the water tank and all participants used Shewfelt's correlation to simulate thermo-mechanical deformation of the PT. The contact heat transfer assumed by the participants had significant variation as shown in Fig. 54. The assumed values varied, and this variation is likely to impose a significant variability in the calculation.

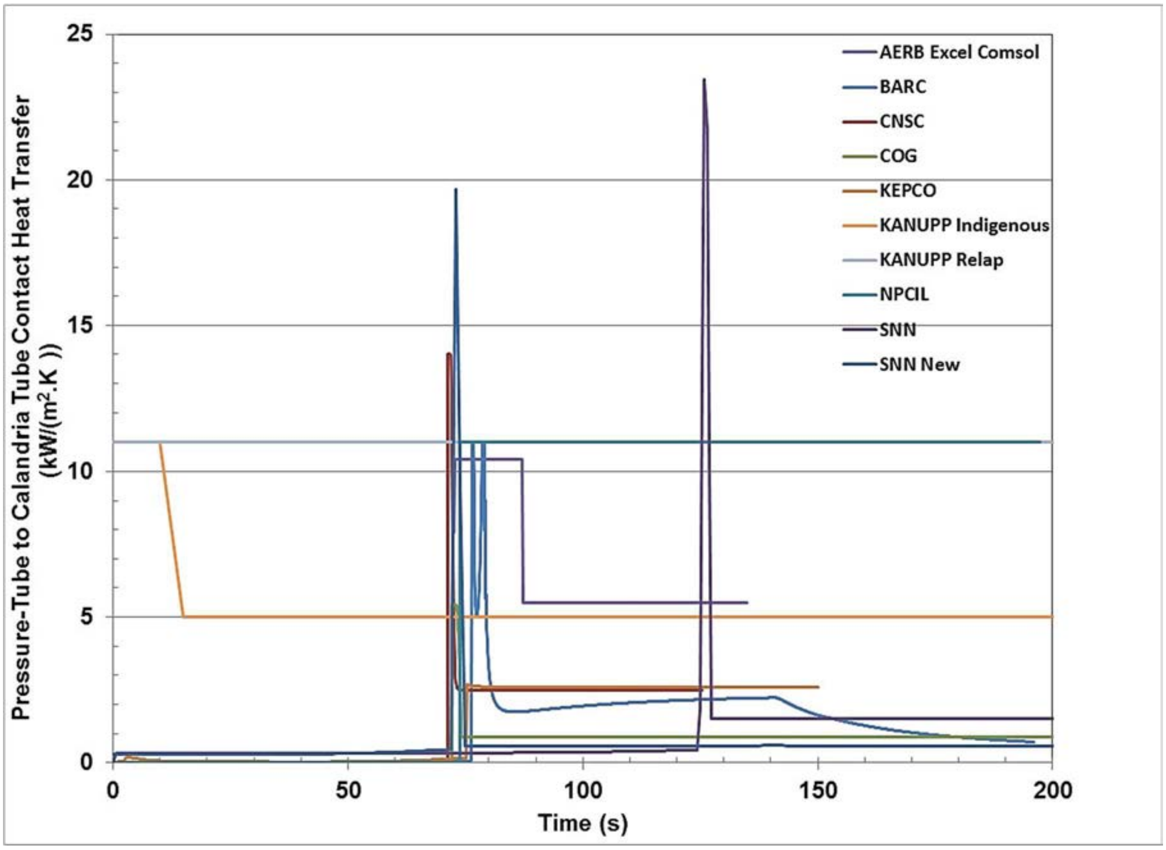

FIG. 54. Comparison of pressure tube to calandria tube heat transfer assumed in the ICSP calculations.

The pressure tube to calandria tube contact heat transfer coefficient is an inferred parameter obtained from a large pool of experiments and engineering judgement. It is one of the key parameters for numerical simulations, since it directly controls post-contact heat transfer rate between the pressure tube and calandria tube, and ultimately impacts the boiling regime at the outside of calandria tube. For adequate comparison to experimental measurements the available models require the contact conductance to be a transient value. The current practice is to use a maximum value at the time of contact (between 10 kW/(m^2·K) and 20 kW/(m^2·K) depending on the pressure) and subsequently decrease it to a steady value (around 1 kW/(m^2·K)).

During the ICSP activity, CNL provided an alternate method to infer the contact heat transfer using an instantaneous energy balance from the energy balance shown in Fig. 33. The energy transferred to the calandria tube is the heat source for the contact heat transfer coefficient, as all heat received by the calandria tube must pass through the contact surfaces following pressure tube calandria tube contact. If the amount of heat going into the calandria tube is divided by the contact surface temperatures and the area, a contact conductance can be derived. The calculated contact conductance using this method using measured inputs from the ICSP test is shown in Fig. 55. The very high initial contact conductance, usually seen in inverse conduction methods immediately after first contact, is absent. Such a heat balance based method avoids the numerical artefacts imposed by inverse conduction methods. The inverse conduction methods tend to give high initial conductance values because initial values are guessed and corrected iteratively to converge the calculated surface temperature to a measured temperature.

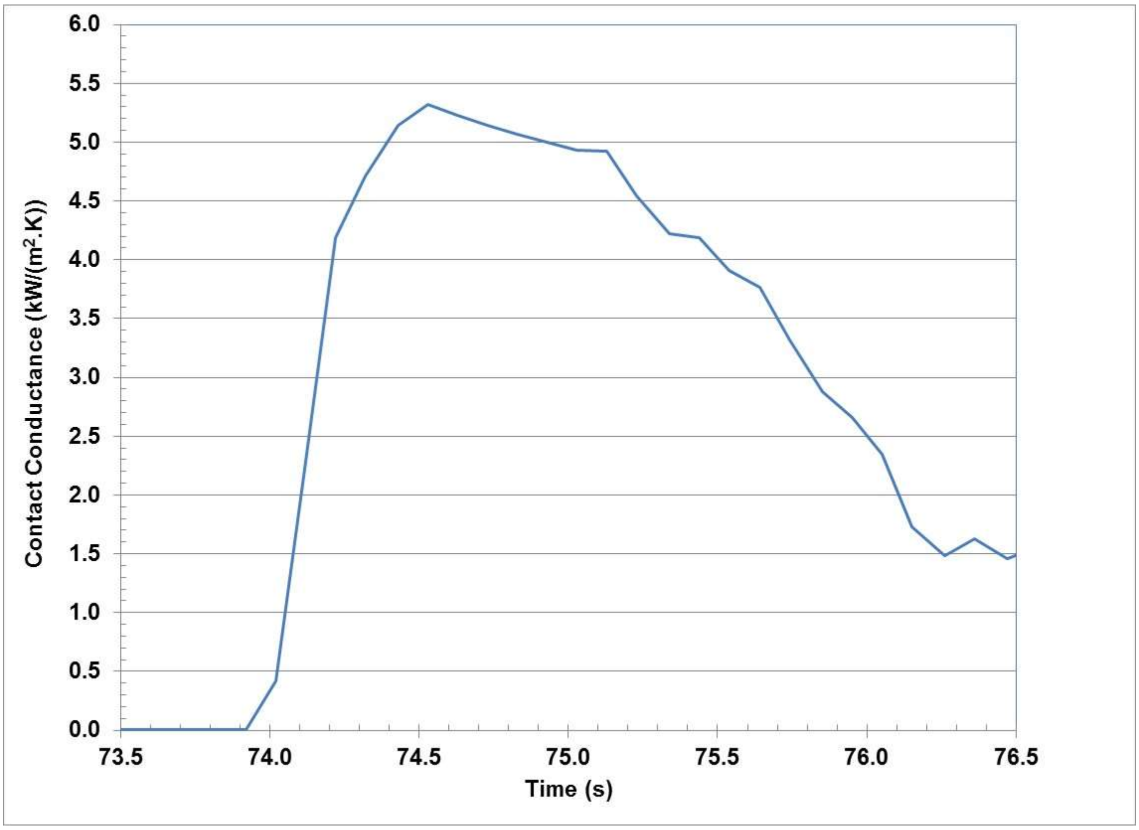

FIG. 55. PT/CT contact conductance derived from instantaneous heat balance.

6.2.4. Boiling models

Calculating calandria tube temperature was the most challenging aspect of the problem to the ICSP participants. The calandria tube temperature is dependent on the boiling correlations used. The dryout period calculated was not in good agreement with measured dryout time. An improved understanding and models are required to simulate calandria tube-to-water pool heat transfer and rewet behaviour.

Few simulations have demonstrated good agreement with water pool temperature while others show a constant temperature (one simulation shows water pool gradually cooling down). Those simulations with large differences may have used an inappropriate volume of the water tank.

6.3. USER EFFECTS

The ICSP activity could not explicitly identify user effects except for the role of nodalization. The choice of an appropriate level of nodalization scheme was left with the code users, to ensure they are sufficiently tested for establishing grid independence. Further investigation in this area is warranted.

7. CONCLUSIONS AND RECOMMENDATIONS

The moderator provides a backup heat sink in HWRs to ensure adequate cooling of fuel in the unlikely event of a large break loss of coolant accident with unavailable emergency cooling injection. Numerous studies have confirmed the capability of the moderator as a backup heat sink to remove residual heat during emergencies. Moderator temperatures (subcooling) are specified to ensure that the transfer of stored heat from the pressure tube to the moderator occurs without film boiling on the calandria tube, which could compromise channel integrity. The subcooling required to minimize the extent of film boiling was determined from contact boiling experiments where pressure tubes were ballooned into contact with calandria tubes at internal pressures ranging from 0.5 to 10 MPa.

Safety analysis codes are validated against full-scale contact boiling experiments conducted using specific channel power, pressure, and moderator subcooling. The pressure tube and calandria tube temperatures, the extent of dryout and failures of the pressure tube or the calandria tube (if any) are the outcome of these experiments. The IAEA International Collaborative Standard Problem (ICSP) on HWR moderator subcooling requirements was performed to demonstrate the analysis capabilities of Member States to calculate the backup heat sink potential of the moderator during accidents.

Eight organizations from five Member States with HWR technology participated in the blind simulation and used 10 different computer codes. For the ICSP activity, a contact boiling experiment reproducing relevant phenomena was completed in order for the participants to perform double-blind, blind and open simulations of the experiment with their computer codes. Canadian Nuclear Laboratories (formerly Atomic energy of Canada Ltd.) conducted the ICSP contact boiling experiment in the High Temperature Fuel Channel Laboratory. During the test, the pressure tube was heated at an average rate of 21.8°C/s and contacted the calandria tube at temperatures ranging from 823 to 919°C. The moderator subcooling at the time of contact averaged 29.6°C. Following contact, the calandria tube experienced patches of film boiling which rewet within 20.8 s and reached a peak measured surface temperature of 649°C. The resulting oxidized patches (indicating dryout) covered 22% of the heated area with large dryout patches along the top of the tube. Based on the extent of oxidation, the IAEA ICSP contact boiling test was classified as patchy film boiling. The dryout resulted in a small amount of deformation in small regions of the CT outside surface. PT and CT integrity was maintained.

Figure 56 shows the relationship between water subcooling and pressure tube heating rate measured during the contact boiling experiments for similar pressure as the ICSP test. In this figure, the resultant contact boiling behaviour becomes more severe as subcooling decreases at a given heating rate. For a given subcooling, higher pressure tube heating rates, which indicate a higher power supplied to the test section, increase the extent of film boiling and therefore the larger the area in dryout.

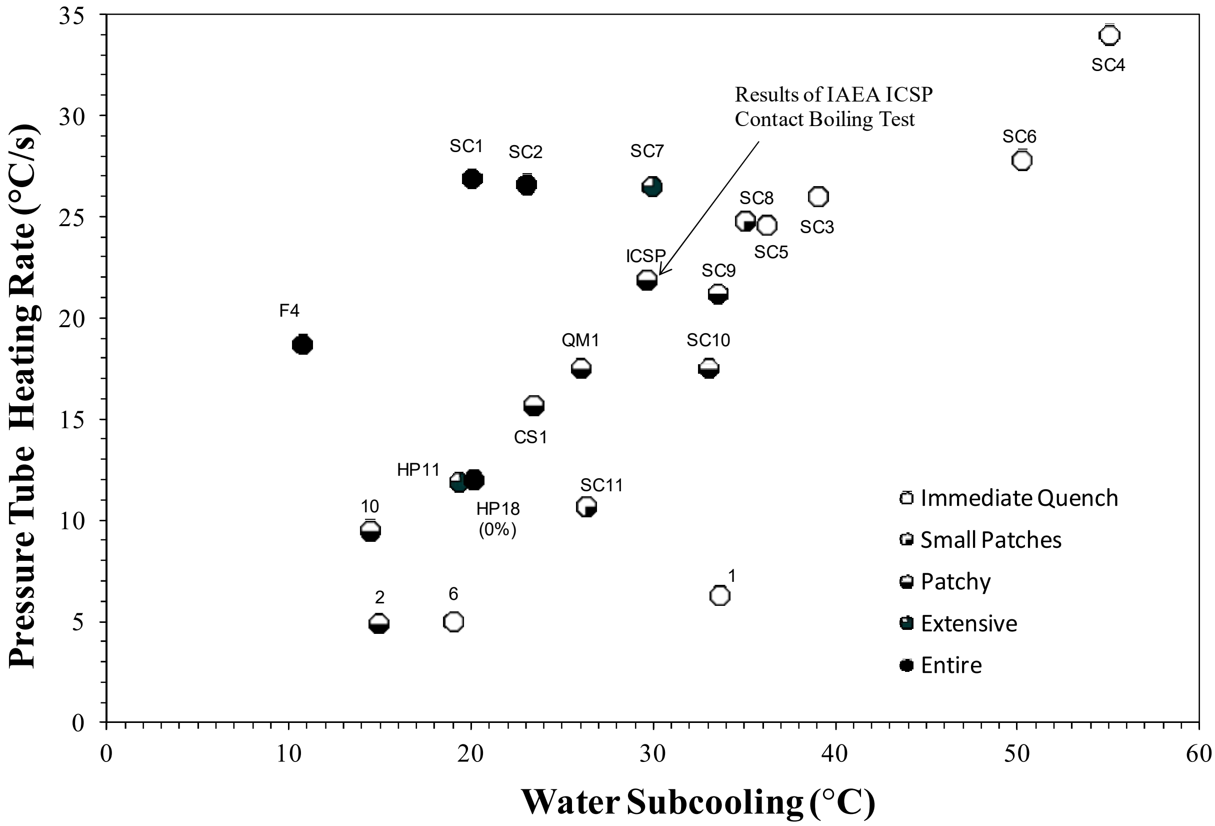

FIG. 56. Comparison of contact boiling behaviour observed in other contact boiling experiments completed between 3.5 and 4 MPa pressure and ICSP test.

The IAEA ICSP blind simulations achieved the objectives and provided significant insights into safety analysis codes. The exercise identified development and validation needs in the codes for the analysis of fuel channel integrity. The blind simulation indicated that:

— The calculated pressure tube contact temperatures were lower than the measured contact temperature and these differences were lower at the sides (90° and 270°) than at the top or at the bottom;
— The pressure tube contact time with the calandria tube was reasonably close to measured contact time for all participants;
— The contact heat transfer assumed by the participants had significant variation. This variation is likely to impose large uncertainties in the calculations;
— Calculating calandria tube temperature was more challenging to the ICSP participants and as a result the dryout period calculated was not in good agreement with measured dryout time;
— Few simulations demonstrated good agreement with measured water pool temperature transient while others assumed a constant temperature;
— The calandria tube dryout and rewet behaviour were not consistent and need improvement;
— Calandria tube strain characteristics appear to be not well captured, potentially due to the uncertainties in the heat transfer;
— An improved understanding and new models are needed to simulate calandria tube to water pool heat transfer and rewet behaviour.

APPENDIX:
OPEN CALCULATION CHECK LIST

- ☐ The transient Contact Conductance from the New Moderator Subcooling Methodology (NMSM) is applied in the open calculation
- ☐ The measured transient power (at V-taps, over the 900 mm between taps) as a function of time applied in the open calculation (ignore spike after shutdown)
- ☐ No reduction of heater power for heat end heat losses (average linear power was 164 kW/m)
- ☐ The water tank has been simulated either by using a very large pipe (if there are code restrictions) with Reservoir boundary conditions equal to atmospheric pressure on both ends of the pipe
- ☐ Measured (average, pre-contact) temperature of the water tank has been applied as initial condition
- ☐ Shewfelt Zr-2.5 Nb creep correlation without any modifications has been applied, taking the PT temperature as the midpoint (between inner and outer radius) temperature
- ☐ Used old graphite properties, same as the graphite properties used in the blind calculations.
- ☐ The new Zr-2.5% Nb property for PT c_p (specific heat as a function of temperature, as supplied by CNL) has been used.
- ☐ If a new correlation for thermal conductivity for Zr-2.5%Nb is distributed by CNL, the new thermal conductivity has been used in the open calculations.
- ☐ The heater has been modelled with an offset (9.5 mm to the bottom) with non-uniform free convection, …OR…

  ☐ The heater has been modelled concentric with no free convection.
- ☐ Used light water properties for water tank.
- ☐ Modelled the PT deformation in a concentric, circular, but non-uniform manner. This will cause all “segments” in a “ring” to contact at the same time.
- ☐ The emissivities of 0.9 (heater), 0.8 (PT), and 0.325 (CT) have been correctly applied.
- ☐ Verified correct CO_2 conductivity, in particular if the correlation is used.
- ☐ Verify and document grid convergence, i.e. independence of results to the nodalization.
- ☐ Verified and consistent correlations for all relevant CT-moderator heat transfer regimes and rewet temperature from NMSM as per list below:
  pre-CHF nucleate boiling: Thom or modified Chen et.al. correlation;
  CHF: Zuber-Griffith;
  post-CHF film boiling: Gillespie-Moyer pool film boiling heat transfer coefficient correlation
  Min. film boiling optimum quench temperature: as supplied by COG;
  Transition: interpolate between "optimum quench temperature” and CHF in the form of $Q=aT^2$

REFERENCES

[1] HART, R.S., SNELL, V.G., SIMPSON, L.A., SANDERSON, D.B., "Passive heat removal in CANDU", Proc. of the IAEA Advanced Group Meeting on Technical Feasibility and Reliability of Passive Safety Systems, Julich (1994).

[2] NITHEANANDAN, T., TIEDE, R.W., SANDERSON, D.B., FONG, R.W.L. COLEMAN, C.E., "Enhancing the moderator effectiveness as a heat sink during Loss-Of-Coolant Accidents in CANDU-PHW reactor using glass-peened surfaces", Experimental Tests and Qualification of Analytical Methods to Address Thermohydraulic Phenomena in Advanced Water Cooled Reactors, IAEA-TECDOC-1149, IAEA, Vienna (2000) 121–137.

[3] EL-HAWARY, M., SZYMANSKI, J., TANASE, A., DELJA, A., OUSSOREN, A., NEAL. P., "New contact boiling experiments to evaluate calandria tube strain acceptance criteria," 35th Annu. Conf. of the Canadian Nucl. Soc., St. John, Canada (2015).

[4] GILLESPIE, G.E., "An experimental investigation of heat transfer from a reactor fuel channel to surrounding water", Proc. of the 2nd Annual CNS Conference, Ottawa, Canada (1981).

[5] BEUTHE, T.G., HANNA, B.N. (Eds), "CATHENA MOD-3.5c/Rev 0 Theoretical Manual," CANDU Owners Group Report, COG-99-007, (1999).

[6] HAGRMAN, D.L., REYMANN, G.A., MATPRO-Ver. 11 (Rev. 1): a handbook of material properties for use in the analysis of light water reactor fuel rod behaviour, NUREG/CR-0497, TREE-1280, Idaho Falls, ID (1979).

[7] SHEWFELT, R.S.W., LYALL, L.W., GODIN, D.P., A high-temperature creep model for Zr-2.5 wt% Nb pressure tubes, J. Nucl. Mater. **125** (1984) 228–235.

[8] ABAQUS User Manual, (1996).

[9] BEUTHE, T.G., HANNA, B. N., "CATHENA MOD-3.5d/Rev 2 Input Reference and GENHTP Input Reference", AECL (2005).

[10] COMSOL MULTIPHYSICS, "Theory for the solid mechanics interface", Structural Mechanics User's Guide, Version 4.3, Stockholm (2012) 160–210.

[11] CHEUNG, S.F., "TUF Software Theory Manual", AMEC NSS Document #CG059/MA/007 R01, (2007).

[12] OH, D.J., LEI, Q.M., "Validation of new moderator subcooling methodology", COG-09-2059, (2010).

[13] MAJUMDAR, P., MUKHOPADHYAY, D., GUPTA, S.K., KUSHWAHA, H.S., VENKAT RAJ, V., "Heat transfer characteristics at calandria tube surface during high temperature transient," 16th National Heat and Mass Transfer Conf. and 5th ISHMT/ASME Heat and Mass Transfer Conf., Kolkata (2002).

[14] MAJUMDAR, P., CHATTERJEE, B., NANDAN, G., MUKHOPADHYAY, D., LELE, H.G., Assessment of the code PTCREEP for IPHWR pressure tube ballooning study, J. Press. Vessel Technol. **133** (2011).

[15] YOVANOVICH, M.M., Thermal contact correlation, spacecraft radiative transfer and temperature control, Astronaut. Aeronaut. **80** (1982) 83–95.

[16] SINGH, B.K., SINGH, R.J., KUMAR, R., NITHEANANDAN, T., KRAUSE, M., GAIKWAD, A.J., 3D-thermo-structural simulation of pressure tube – calandria tube behaviour under accident conditions in PHWR using ABAQUS, Nucl. Eng. Des. **328** (2018) 188–196.

[17] DUREJA, A.K., SINHA, S.K., SRIVASTAVA, A., SINHA, R., Flow behaviour of autoclaved, 20% cold worked, Zr2.5Nb alloy pressure tube material in the temperature range of room temperature to 800°C, J. Nucl. Mater. **412** (2011) 22–29.

[18] CHURCHILL, S.W., CHU, H.H.S., Correlating equations for laminar and turbulent free convection from a horizontal cylinder, Int. J. Heat Mass Transf. **18** (1975) 1049.

[19] INCROPERA, F., DEWITT., D.P., BERGMAN, T.L., LAVINE, A.S., Fundamentals of Heat and Mass Transfer, 6th edn, John Wiley & Sons Inc., Hoboken, NJ (2006).
[20] BJORNARD, T.A., GRIFFITH, P., "PWR blowdown heat transfer", Thermal and Hydraulic Aspects of Nuclear Reactor Safety, Vol. 1 (JONES, O.C. Jr., BANKOFF, S.G. Eds.), American Society of Mechanical Engineers, New York (1977) 17–41.
[21] SHOUKRI, M., CHAN, A.M.C., On the thermal analysis of pressure tube/calandria tube contact in CANDU reactors, Nucl. Eng. Des. **104** 2 (1987) 197–206.
[22] YOVANOVICH, M.M., HEGAZY, A., "An accurate universal contact conductance correlation for conforming rough surfaces with different micro-hardness profiles," AIAA 18th Thermophys. Conf., Montreal (1983).
[23] BAHRAMI, M., CULHAM, J.R., YOVANOVICH, M.M., "Thermal resistance of gaseous gap for conforming rough contacts," 42nd AIAA Meet. and Exhibit, Reno (2004).
[24] ROHSENOW, W.M., A method of correlating heat transfer data for surface boiling of liquids, Trans. ASME **74** (1952) 969–975.
[25] YAGOV, V.V., LEKSIN, M.A., Subcooled-liquid boiling crisis on horizontal cylindrical heaters, Therm. Eng. **53** 4 (2006) 262–269.
[26] GILLESPIE, G.E., MOYER, R.G., THOMPSON, P.D., "Moderator Boiling on the External Surface of a Calandria Tube in a CANDU Reactor during a Loss of Coolant Accident", Proc. Int. Meet. Therm. Nucl. React. Saf., Chicago (1982).
[27] MORI, M., TODA, S., OCHIAI, M., SAITO, S., Transient cooling process of fuel rod in reactivity initiated accident, J. Nucl. Sci. Technol. **17** 6 (1980) 413–424.
[28] SAKURAI, A., SHIOTSU, M., HATA, K., A general correlation for pool film boiling heat transfer from a horizontal cylinder to subcooled liquid: Part 1 - A theoretical pool film boiling heat transfer model including radiation contributions and its analytical solution, J. Heat Transf. **112** (1990) 430–440.
[29] SAKURAI, A., SHIOTSU, M., HATA, K., A general correlation for pool film boiling heat transfer from a horizontal cylinder to subcooled liquid: Part 2 - Experimental data for various liquids and its correlation, J. Heat Transf. **112** (1990) 441–450.
[30] TANASE, A., SZYMANSKI, J., EL-HAWARY, M., DELJA, A., "Numerical Predictions of Heat Transfer and Pressure Tube/Calandria Tube Deformation During Calandria-Tube Strain Contact Boiling (CSCB) Tests," 7th Int. Conf. on Model. and Simul. in Nucl. Sci. and Eng., Ottawa, (2015).
[31] CZIRACKY, A., Pressure Tube-Calandria Tube Thermal Contact Conductance, MS Thesis, McMaster Univ. (2006).
[32] LIS, C., "Experimental investigation of natural convection heat transfer in simple and obstructed horizontal annuli", Proc. 3rd Int. Heat Transf. Conf., Vol. 2, Chicago (1966) 196–204.
[33] FORSTER, H.K., ZUBER, N., Dynamics of vapor bubbles and boiling heat transfer, AIChE J. **1** 4 (1955) 531–535.
[34] LIENHARD, J.H., DHIR, V.K., Hydrodynamic prediction of peak pool-boiling heat fluxes from finite bodies, J. Heat Transf. **95** 2 (1973) 152–158.
[35] THIBAULT, J., Boiling heat transfer around a horizontal cylinder and in tube bundles, PhD. Thesis, McMaster Univ. (1978).
[36] LAUER, H., HUFSCHMIDT, W., Heat transfer and surface rewet during quenching, Ad. Study Inst. on Two-Ph. Flows and Heat Transf., Istanbul (1976).
[37] KIM, H.T., CHANG, S.-M., PARK, J.H., "Unsteady two-dimensional multiphysical simulation of a pressure tube model expanded to contact with the outer concentric tube," J. Nucl. Sci. and Tech. **53** (2015) 580–591.
[38] KIM, H.T., CHANG, S.-M., SON, Y.W., MIN, T., Multiphysical simulations for the IAEA/ICSP benchmark model on the contact of pressure tube and calandria tube in the

moderator system of a CANDU-6 PHWR, Sci. and Tech. of Nucl. Installations **2018** (2018) 1–8.

[39] MEGSON, T.H.G., in Aircraft Structures for Engineering Students, Edward Arnolds, Bristol (1985) 22–25.

[40] CHANG, S.M., KIM, H.T., "Unsteady two-dimensional multiphysical simulation on the radiating calandria tube under the subcooling boundary condition," Transaction of Korean Nuclear Society 2012 Autumn Meeting, Kyoungju, South Korea, October (2012).

[41] CENGEL, Y., Introduction to Thermodynamics and Heat Transfer: Vol. II Heat Transfer, International Editions, McGraw-Hill, New York (2001).

[42] GEELHOOD, K.J., BEYER, C.E., LUSCHER, W.G., PNNL Stress/Strain Correlation for Zircaloy, Rep. PNNL-17700, Pacific Northwest National Laboratory, WA (2008).

[43] LUSCHER, W.G., GEELHOOD, K.J., Material Property Correlations: Comparisons between FRAPCON-3.4, FRAPTRAN 1.4, and MATPRO, Rep. NUREG/CR-7024 PNNL-19417, U.S. Nuclear Regulatory Commission, (2011).

[44] RAITHBY, G.D., HOLLANDS, K.G.T., "Natural convection", The Handbook of Heat Transfer, 3rd edn (ROHSENOW, W.M., HARTNETT, J.P., CHO, Y.I., Eds), McGraw-Hill, New York (1998) Ch. 4.

ABBREVIATIONS

CANDU	CANadian Deuterium Uranium
CHF	Critical heat flux
CT	Calandria tube
GH	Graphite heater
HWR	Heavy water reactor
HTC	Heat transfer coefficient
IAEA	International Atomic Energy Agency
ICSP	International collaborative standard problem
PT	Pressure tube
NMSM	New moderator subcooling methodology
RTD	Resistance temperature detector
TC	Thermocouple
TWG-HWR	Technical working group on advanced technologies for HWRs
WCR	Water cooled reactor

CONTRIBUTORS TO DRAFTING AND REVIEW

Chatterjee, B.	Bhabha Atomic Research Centre (BARC), India
El Hawary, M.	Canadian Nuclear Safety Commission (CNSC), Canada
Gaikwad, A.J.	Atomic Energy Regulatory Board (AERB), India
Hasanein, H.	CANDU Owners Group (COG), Canada
Istrate, E.R.	Cernavoda Nuclear Energy (CNE), Romania
Kim, H.T.	Korean Atomic Energy Research Centre (KAERI), Republic of Korea
Krause, M.	International Atomic Energy Agency (IAEA), Vienna, Austria
Nitheanandan, T.	Canadian Nuclear Laboratories (CNL), Canada
Noora, A.	Karachi Nuclear Power Plant (KANUPP). Pakistan

Technical Meetings

Ottawa, Canada: 19–21 November 2012
Vienna, Austria: 9–11 July 2014, 27–29 January 2015

Consultants Meetings

Vienna, Austria: 14–17 February 2012

ORDERING LOCALLY

IAEA priced publications may be purchased from the sources listed below or from major local booksellers.

Orders for unpriced publications should be made directly to the IAEA. The contact details are given at the end of this list.

NORTH AMERICA

Bernan / Rowman & Littlefield
15250 NBN Way, Blue Ridge Summit, PA 17214, USA
Telephone: +1 800 462 6420 • Fax: +1 800 338 4550
Email: orders@rowman.com • Web site: www.rowman.com/bernan

Renouf Publishing Co. Ltd
22-1010 Polytek Street, Ottawa, ON K1J 9J1, CANADA
Telephone: +1 613 745 2665 • Fax: +1 613 745 7660
Email: orders@renoufbooks.com • Web site: www.renoufbooks.com

REST OF WORLD

Please contact your preferred local supplier, or our lead distributor:

Eurospan Group
Gray's Inn House
127 Clerkenwell Road
London EC1R 5DB
United Kingdom

Trade orders and enquiries:
Telephone: +44 (0)176 760 4972 • Fax: +44 (0)176 760 1640
Email: eurospan@turpin-distribution.com

Individual orders:
www.eurospanbookstore.com/iaea

For further information:
Telephone: +44 (0)207 240 0856 • Fax: +44 (0)207 379 0609
Email: info@eurospangroup.com • Web site: www.eurospangroup.com

Orders for both priced and unpriced publications may be addressed directly to:

Marketing and Sales Unit
International Atomic Energy Agency
Vienna International Centre, PO Box 100, 1400 Vienna, Austria
Telephone: +43 1 2600 22529 or 22530 • Fax: +43 1 26007 22529
Email: sales.publications@iaea.org • Web site: www.iaea.org/publications

19-00871

International Atomic Energy Agency
Vienna
ISBN 978–92–0–162919–7
ISSN 1011–4289